December 2022

Unraveling Deformation Mechanisms and Kinematics in Metasedimentary Rocks Along the Southern Iberian Shear Zone

Kayla P. Kopinski
University of Wisconsin-Milwaukee

UNRAVELING DEFORMATION MECHANISMS AND KINEMATICS IN METASEDIMENTARY ROCKS ALONG THE SOUTHERN IBERIAN SHEAR ZONE

by

Kayla Kopinski

A Thesis Submitted in

Partial Fulfillment of the

Requirements for the Degree of

Master of Science

in Geosciences

at

The University of Wisconsin-Milwaukee

December 2022

ABSTRACT

UNRAVELING DEFORMATION MECHANISMS AND KINEMATICS IN METASEDIMENTARY ROCKS ALONG THE SOUTHERN IBERIAN SHEAR ZONE

by

Kayla Kopinski

The University of Wisconsin-Milwaukee, 2022
Under the Supervision of Professor Dr. Dyanna Czeck

The primary goal of this project is to document deformation mechanisms in quartz-rich rocks across a 100 m wide ductile shear zone to evaluate whether strain localization at the brittle-ductile transition is accompanied by variations in active or dominant deformation mechanisms. A secondary goal of this project is to evaluate whether the kinematic framework varies across a shear zone with a major rheological boundary. The Southern Iberian Shear Zone (SISZ), a major terrane bounding shear zone within the Iberian Massif, is an ideal location to study these questions because it is a regional scale shear zone currently exposed at the level of the brittle-ductile transition that has well-documented strain and kinematics. Previous studies focused largely on deformation in the Beja-Acebuches metabasite (BAM) rocks on the northern side of the shear zone; whereas this study focuses on the Pulo do Lobo (PdL) metasedimentary rocks on the south side of the shear zone. Using microstructural analysis and EBSD data on 24 oriented samples, new information was learned about the PdL unit that is in contact with the SISZ.

Microstructural analyses revealed that brittle, diffusional, and dislocation deformation mechanisms were active in quartz deformation. Electron Backscatter Diffraction (EBSD) analysis of quartz provided a dataset that had helped uncover information about the kinematics of the shear zone, the slip systems that were active, and whether diffusional processes or dislocation processes dominated during ductile deformation. The EBSD data was used to generate crystallographic preferred orientation (CPO) plots in quartz. Weak CPO patterns indicated that, although dislocation processes contributed to the deformation, diffusional processes dominated. CPO patterns and misorientation axis plots were also used to infer that prism <a> is the dominant slip systems within quartz. Previous studies demonstrated that prism <a> slip dominates at approximately 500°C, which gives a constraint on temperature during deformation. This temperature estimate is broadly consistent with the upper greenschist facies metamorphic assemblage in the PdL near the SISZ, but likely inconsistent with lower grade slates >150 m away from the SISZ which have the same dominant slip systems. Further studies are needed to unravel that apparent discrepancy.A crystallographic vorticity axis (CVA) analysis, which uses the internal distortion of grains, was used to further understand the kinematics of the SISZ. The CPO and CVA analyses were used to interpret the kinematics of the SISZ within the PdL. Results were consistent with a combination of flattening and simple shear. The orientation of the vorticity vector that is associated with the noncoaxial part of the strain regime varies at the meter, or potentially even submeter scale. The simple shear varies between left-lateral, oblique, and thrust orientations. This is in contrast to the consistent left-lateral simple shear component in the BAM.

TABLE OF CONTENTS

LIST OF FIGURES

LIST OF TABLES

ACKNOWLEDGEMENTS

I would like to thank my advisor Dr. Dyanna Czeck for everything she has done for me and presenting me with this amazing opportunity. She is very influential to me, and I hope to follow her footsteps and help graduate student as she has helped me tremendously. She has supported me throughout this whole project and has helped me when I was not feeling so confident in this project. She may be one of the hardest working educators I have ever seen and her love for geology makes you love it even more. I would not have been able to complete this project if it wasn't for her and her hard work. I would like to acknowledge the NSF grant IRES-1854155 to Dr. Dyanna Czeck and the AOP Fellowship for funding on this project. The funding has made a huge difference in completing my masters and I am very grateful for it. Second, I would like to thank Dr. Gary Solar, my ungraduate mentor. Without his help, I would not have made it to where I am today. He has always supported me and my ambitions and pushed me to be a better structural geologist. He was always there to help with anything during my masters and I am very thankful for that. Dyanna and Gary are both tied for the hardest working educators I have ever seen. There are not any better structural geologists to learn from in my opinion (even if they are the only two structural geologists, I have had the pleasure to work with). A huge thank you goes out to Dr. Zachary Michels. I don't think I would have been able to complete this project without him. I am amazed at how smart he is and his ability to use MATLAB (it is truly amazing). He has helped me with all the new techniques described in this paper and learning all the cool knew information we weren't expecting. He is a MATLAB guru, and he needs a certificate or something for that! Lastly, I would like to thank Manu Diaz Azpiroz, Carlos Fernandez, Bil Schneider, and Nancy Carman for help and support on this project. They may not

have realized how much they have helped with this project, but their thoughts, data, and papers have help me with this project so much. The team working on the SISZ is the best team to be a part of.

CHAPTER 1: Introduction

1.1 Objective

The primary goal of this project is to document deformation mechanisms in quartz-rich rocks across a 100 m wide ductile shear zone to evaluate whether strain localization at the brittle-ductile transition is accompanied by variations in active or dominant deformation mechanisms. The focus of this project is on the southern boundary of the Southern Iberian Shear Zone (SISZ), which contains metasedimentary rocks that are part of the Pulo do Lobo (PdL) formation whose structural geometry and internal strain localization is more complex and lesser known than the extensively-studied Beja-Acebuches metabasite (BAM) rocks found on the northern side of the SISZ (Azpiroz and Fernández, 2003; Bard and Moine, 1979; Aspiroz et al., 2007; Azpiroz et al, 2003; Díaz-Azpiroz and Fernández, 2005). A secondary goal of this project is to evaluate whether the kinematic framework within the PdL matches the well-studied kinematics of the BAM on the other side of the shear zone. Within the PdL, strain gradually decreases from the SISZ, but also forms intricate patterns of shear bands, partially controlled by lithology. Preliminary work by Carman (2020) and other researchers in our group (unpublished) documented two features that suggest that kinematics may differ within the PdL compared to the BAM: 1) shear sense indicators on the m to dm scale shear bands indicate largely thrust motion while shear sense indicators in the BAM are largely consistent with left-lateral motion, and 2) lineations in the PdL are primarily oriented down-dip along the foliation, an observation also broadly consistent with more thrust dominated motion and/or pure shear dominated transpression.

Both of these goals contribute to our understanding of aspects of strain localization. "Strain localization" describes an important phenomenon at tectonic boundaries, that deformation intensity is not uniform, but some zones have higher strain than others. Strain localization fundamentally controls the presence of shear zones, and thus evolution of rock strength and deformation at plate boundaries. The location and magnitude of strain localization are dependent on numerous factors such as temperature, composition, grain size, texture, presence and composition of fluids, strain rate, and deformation mechanisms and these may vary throughout the deformation history. In this study, deformation mechanisms and lithologic controls (grain size and composition) will be primarily studied. Tectonic fabrics and grain-scale kinematic analyses will be used to constrain the kinematic framework. The PdL Formation at the SISZ is a perfect choice for this study because it contains two major lithologies, quartzites and metapelites, and kinematics on the other side of the shear zone (within the BAM) have been well documented.

1.2 Kinematic framework of shear zones

In introductory texts, if they are discussed at all, shear zones are typically shown with simple motions- either right-lateral, left-lateral, thrust/reverse, or normal, all of which can be modeled by simple shear in various orientations. Although early studies of ductile shear zones modeled them as having motions related to simple shear only (Ramsay, 1967; Ramsay & Graham, 1970), since transpression studies of the 1990s (e.g. Fossen and Tikoff, 1993), structural geologists have found increasingly more complex motions in shear zones with oblique simple shear and/or additions of pure shear or flattening with variable extrusion directions (Lin et al., 1998; Czeck and Hudleston, 2003; Sullivan and Law, 2007; Fernández et al., 2013). In order to evaluate the

three-dimensional geometries of shear zones, more complex toolkits are needed (e.g. Fernández et al., 2013, Díaz-Azpiroz et al., 2019, Kruckenberg et al., 2019). One parameter that helps characterize the three-dimensional complexities of shear zones is the vorticity vector (Fig. 1). Vorticity is the measure of internal rotation about an axis, the vorticity vector. The vorticity vector's orientation depends only on the simple shear part of the kinematic framework, and it is perpendicular to the shear plane, also known as the vorticity normal section or VNS. In strike-slip systems, the shear plane is horizontal, and the vorticity vector is vertical. In thrust/reverse and normal systems, the shear plane is vertical, and the vorticity vector is horizontal. In oblique shear, the shear plane is neither horizontal nor vertical, and the vorticity vector is consequently oblique. Identifying the VNS or the orientation of the vorticity vector in the field can be difficult. In some cases, the VNS orientation is approximated using the plane that contains the largest abundance of asymmetric features such as σ and δ porphyroclasts, Z- and S- folds, and S-C fabrics (e.g. Czeck and Hudleston, 2003; Díaz Azpiroz and Fernandez, 2005). However, in many cases, especially in fine-grained rocks, such asymmetric features cannot be seen at the outcrop scale, so geologists cut thin sections to look for them. Traditionally, geologists assume that the VNS is a plane that is perpendicular to the foliation and parallel to the lineation, and this simplification is taught in textbooks (e.g. Fossen, 2016). However, recent studies have made it clear that assuming this plane is the VNS is problematic because embedded in that assumption is a simple-shear kinematic framework (alternatively also compatible with some monoclinic geometries) (Díaz-Azpiroz et al., 2019). The orientation the vorticity vector depends on the amount of the simple shear component. The vorticity normal section (VNS) is the shear plane and the vorticity axis is the axis of internal rotation and is the pole to the VNS. Different kinematic models all have a different orientation of the VNS (Fig. 1), in triclinic transpression,

the vorticity vector is subparallel to the Y-axis for lower strain values and approaches the X-axis for increasing strain (Díaz-Azpiroz et al., 2019). To determine the VNS of a sample, the section that contains maximum noncoaxiality is the best section to run kinematic analysis. This means the orientation of the foliation and lineation are crucial in determining the VNS and therefore the vorticity vector. There are many samples such as the PdL where lineations are rare in the field, making it difficult to determine where thin sections should be cut (e.g., perpendicular to foliation and parallel to the lineation). This does not mean kinematic analyses have to be halted.

A relatively new technique called crystallographic vorticity axis (CVA) analysis uses the slight differences in crystallographic orientations within individual grains to determine the orientation of the vorticity axis (Michels et al., 2015; Kruckenberg et al, 2019). CVA analysis can be conducted relatively easily with the detailed crystallographic orientation data acquired through EBSD. In this study, CVA analysis is used in conjunction with field observations to determine the orientation of the vorticity vector. This is one way in which we can test whether the kinematic framework is consistent across the SISZ.

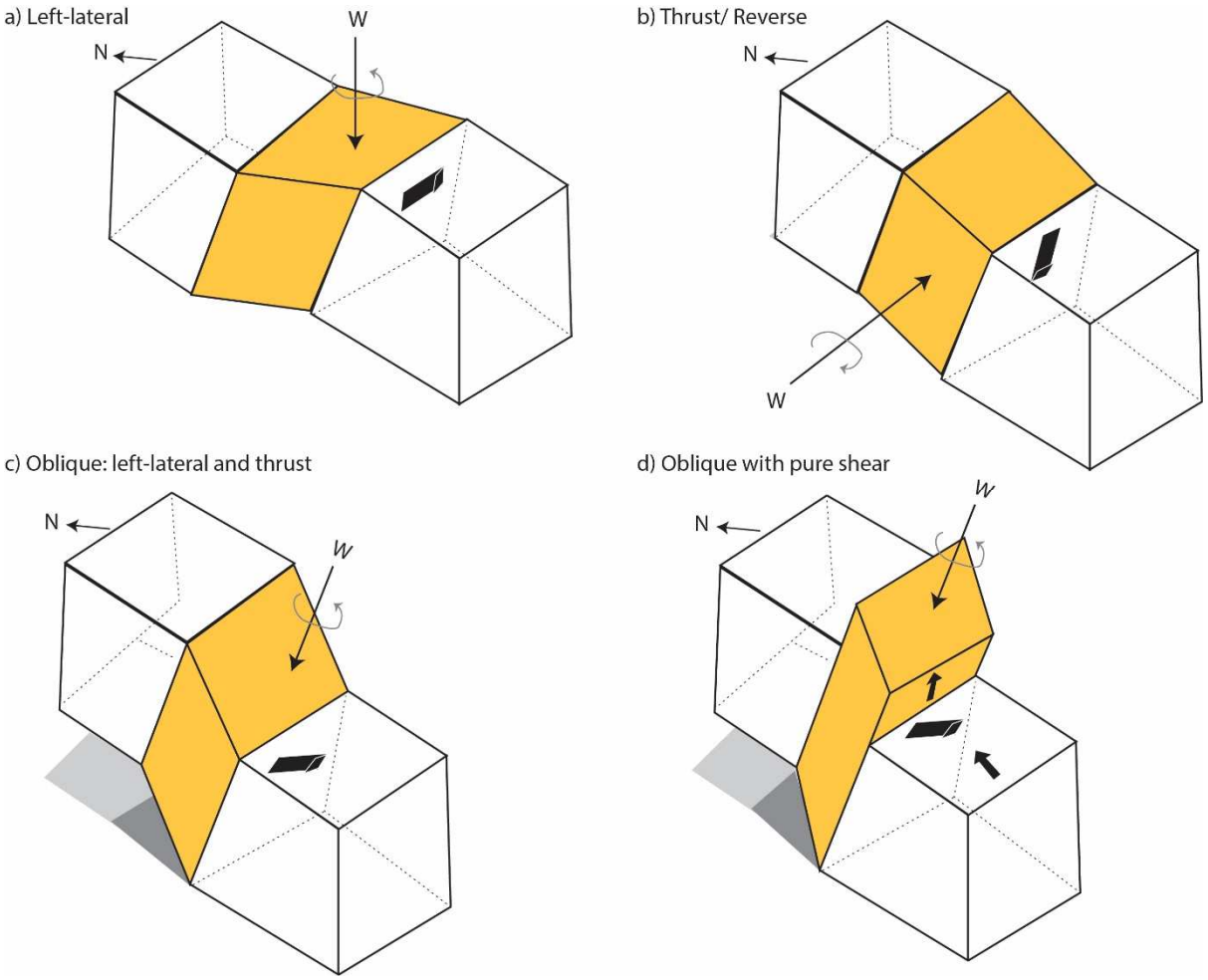

Figure 1: Kinematic models for shear zones dipping approximately 50° to the NNE, like the SISZ. a) Left-lateral shear zone. Vorticity vector is vertical with counter-clockwise rotation. b) Thrust shear zone. Vorticity vector is horizontal with rotation compatible with north side up. c) Oblique shear zone with thrust and left-lateral components. Vorticity vector is oblique to the tectonic framework (perpendicular to the shear plane); orientation depends on the relative proportions of left-lateral and thrusting. d) Oblique shear zone with thrust and left-lateral components with the addition of pure shear to cause shortening across the zone. Vorticity vector orientation only depends on simple shear components, so is the same as shown in c). Here, pure shear is shown with shortening across the zone and dip-parallel extrusion. From Czeck, unpublished, 2022

1.3 Why study variations in deformation mechanisms and kinematics of shear zones

The results of this research will help to refine the kinematic model of the SISZ. Previous detailed kinematic modeling (Díaz-Azpiroz and Fernández, 2005; Fernández et al., 2013) was

based on structures contained within the BAM, but initial work on the PdL suggests that the kinematics may have been different on either side of the SISZ (Carman, 2020). Further refinement of kinematic model within the SISZ may be used to better understand the nature of the tectonic collision that formed it. For example, the results may be used place constraints on plate convergence angle (e.g., Horsman et al., 2008) or amount of displacement (e.g., Fossen, 2016).

Kinematics in natural deformation zones may be complex, three-dimensional, and vary spatially and temporally. Recognizing kinematic partitioning and summing the resultant deformation within differently partitioned zones are keys to proper reconstruction of tectonic history (Horsman and Tikoff, 2005; Horsman et al., 2008). CPOs and microstructures can be used to reflect the strain kinematics and deformation processes during progressive shear zone development (Toy et al., 2008). This project reveals a detailed natural example of kinematic partitioning, and demonstrate the scales at which partitioning can be observed.

The SISZ is an example of a well exposed mid-crustal shear zone, and the results of this study may be used to understand broader questions in ductile shear zones. For example, a community document outlining outstanding "Grand Challenges" in structural geology and tectonics includes understanding the variables involved in rock rheology and the behavior of fault zones from surface to mantle as key avenues of research (Huntington and Klepeis, 2018). Strain localization is a critical component of fault behavior and unravelling the importance of various factors such as mineralogy, grain size, fluid-rock interactions, deformation mechanisms, and temperature is key to understanding strain localization processes.

CHAPTER 2: Geologic Background

2.1 Tectonic Evolution of the SISZ

2.1.1 The Variscan Belt

The Variscan orogeny is the cause of the Variscan belt of Europe and is the result of orogenic evolution (Navarro and Fernandez, 2004). The Variscan belt involved the collision of multiple continental masses which include Gondwana, Laurentia, and Baltica (Fig. 2), that resulted in a large cratonic block known as the Iberian Massif (Navarro and Fernández, 2004; Azor et al., 2008). Within the Iberian Massif, most tectonic features are the result of Devonian and Carboniferous collision between Gondwana, some peri-Gondwanan terranes, and the Avalonian border of Laurentia (Ayarza et al., 2021). The Iberian Massif is divided into two transects, the northern section that consists of an east vergent orogenic wedge, and the southern section that contains three different continental blocks. These three blocks are the Southern Portuguese Zone (SPZ), the Ossa Morena Zone (OMZ), and the Central Iberian Zone (CIZ). The focus of this project is in the southern zone of the Iberian Massif, specifically the contact between the SPZ and OMZ, the Southern Iberian shear zone (SISZ) (Fig. 3). The SISZ marks the suture between these two blocks. The SISZ follows the contact between the Pulo do Lobo (PdL) accretionary prism, which is part of the SPZ, and the Beja-Acebuches metabasites (BAM), which is part of an oceanic complex between the OMZ and SPZ (Crespo-Blanc and Orozco, 1998) (Fig.3).

The Ossa Morena Zone has been interpreted as a poly-orogenic terrane accreted to the Central Iberian Zone (CIZ) during the Cadomain Orogeny. This zone consists of low to medium grade rocks, high grade rocks, and the Acebuches Metabasites (Fig. 5). The structural evolution of the OMZ is governed by transpressional tectonics (Braid, 2010). The Southern Portuguese

Zone is dominated by Upper Devonian to lower Carboniferous sedimentary and bimodal volcanic sequence of the Iberian Pyrite Belt. The SPZ contains rocks of a late Paleozoic sequence including the Pulo do Lobo domain (PdL) in the northern most section and volcano-sedimentary complex (Fig 5). During the Middle Devonian, the Variscan tectonics started with oblique subduction of the Rheic Ocean, which formed into the PdL accretionary prism and the BAM unit. The subduction of the oceanic crust then led to the collision of the OMZ with the SPZ during the Late Devonian (Romeo et al., 2007).

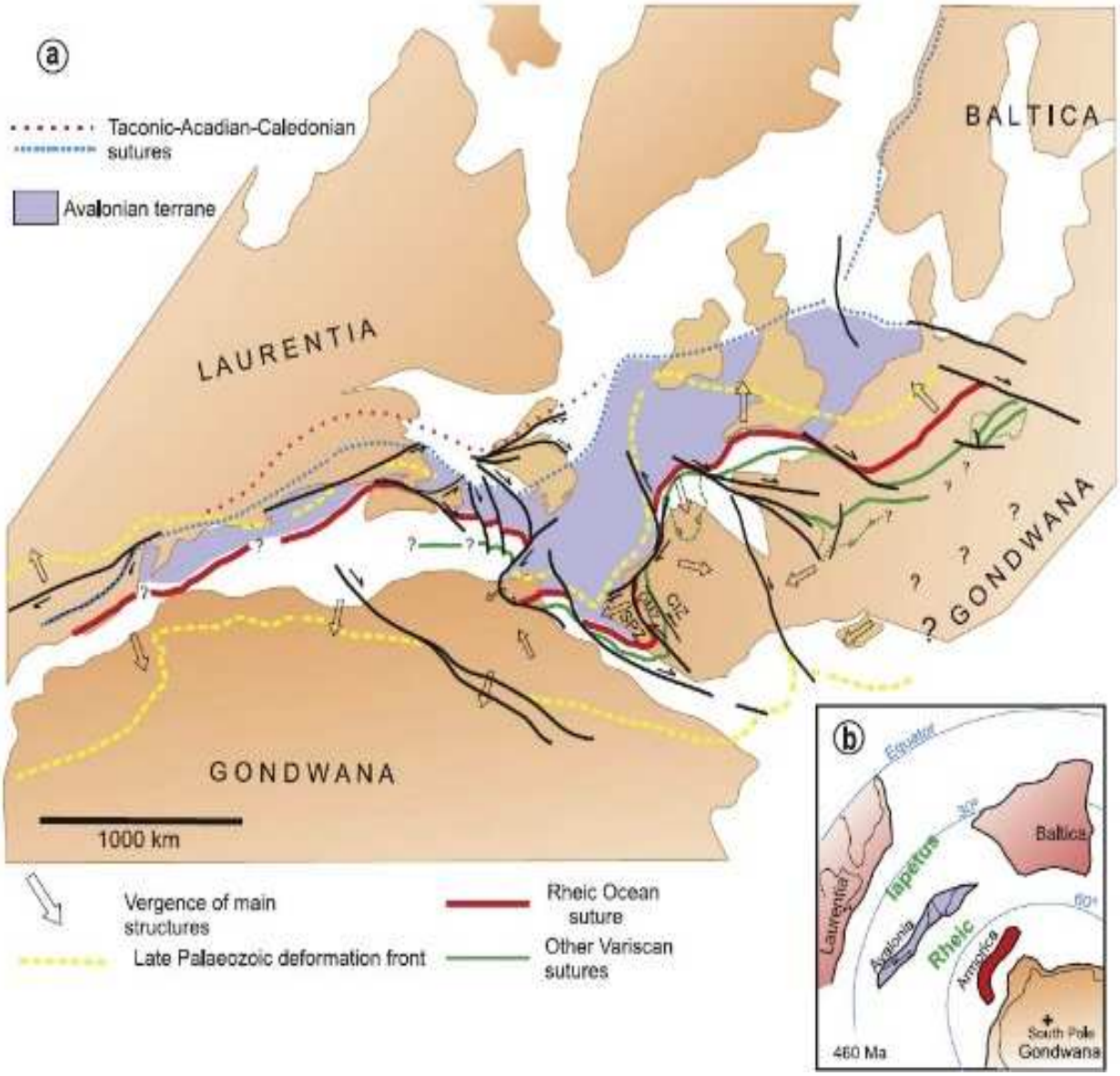

Figure 2: a) Paleotectonic reconstruction of the late Carboniferous Variscan-Alleghanian Orogenic Belt. b) Different zones that have been affected by the continental bodies of Laurentia, Gondwana, Baltica, and intermediate terranes. From Azor et al, 2008.

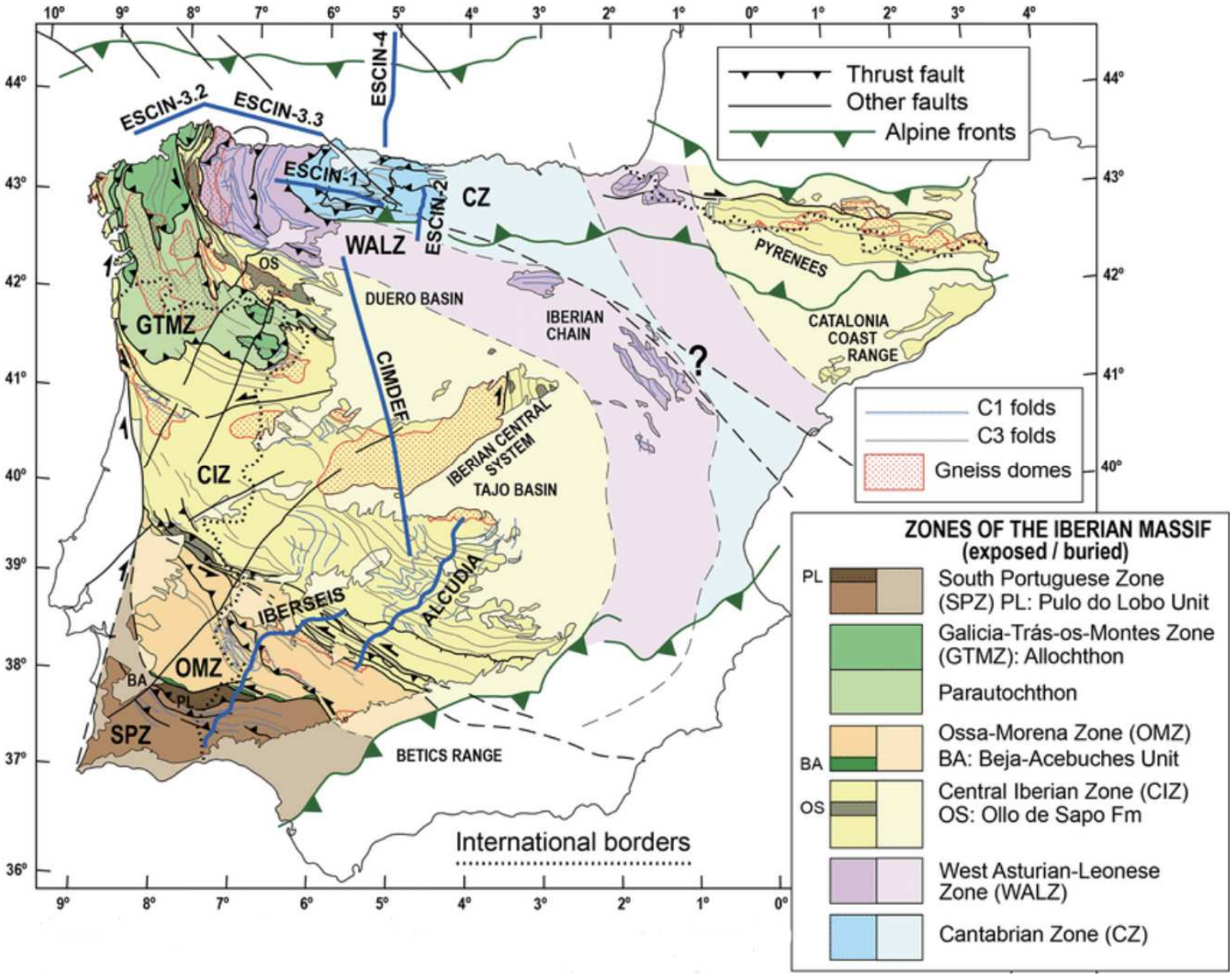

Figure 3: Map indicating the subdivisions of the Iberian Massif. The zones of focus are the OMZ, which is the peach and green, and the SPZ, which are the shades of brown. From Ayarza et al., 2021.

2.1.2 The Southern Iberian Shear Zone (SISZ)

The SISZ is a 300– 500 m thick zone that is oriented WNW-ESE and dips around 50° to the NNE (Díaz-Azpiroz and Fernández, 2005). S-C-C' structures, folds, porphyroclasts, and various other brittle-ductile structures were used to infer an oblique sinistral, top to the WSW sense of movement in the metabasites. The metabasites within the SISZ have a penetrative mylonitic foliation (S_2) and a related stretching lineation (L_2). The S_2 foliation is defined by the arrangement of plagioclase and amphibole in the amphibolites and epidote and chlorite rich layers within the schists. The foliation and lineation are strongest toward the structural base of the metabasites. Most of the rocks in this series have a lineation and a foliation, but there are some rocks that only have a foliation (Díaz-Azpiroz and Fernández, 2005). The orientation of the foliation is WNW-ESE oriented and dips to the NNE. The lineation orientation varies within the metabasite series along segments of the SISZ. Lineations plunge to the SE in the eastern segment, to the NW in the central segment, and back to the SE in the western segment (Fig. 4). The SISZ has an apparent en echelon arrangement due to subsequent cross-cutting Variscan strike slip faults (Díaz-Azpiroz and Fernández, 2005).

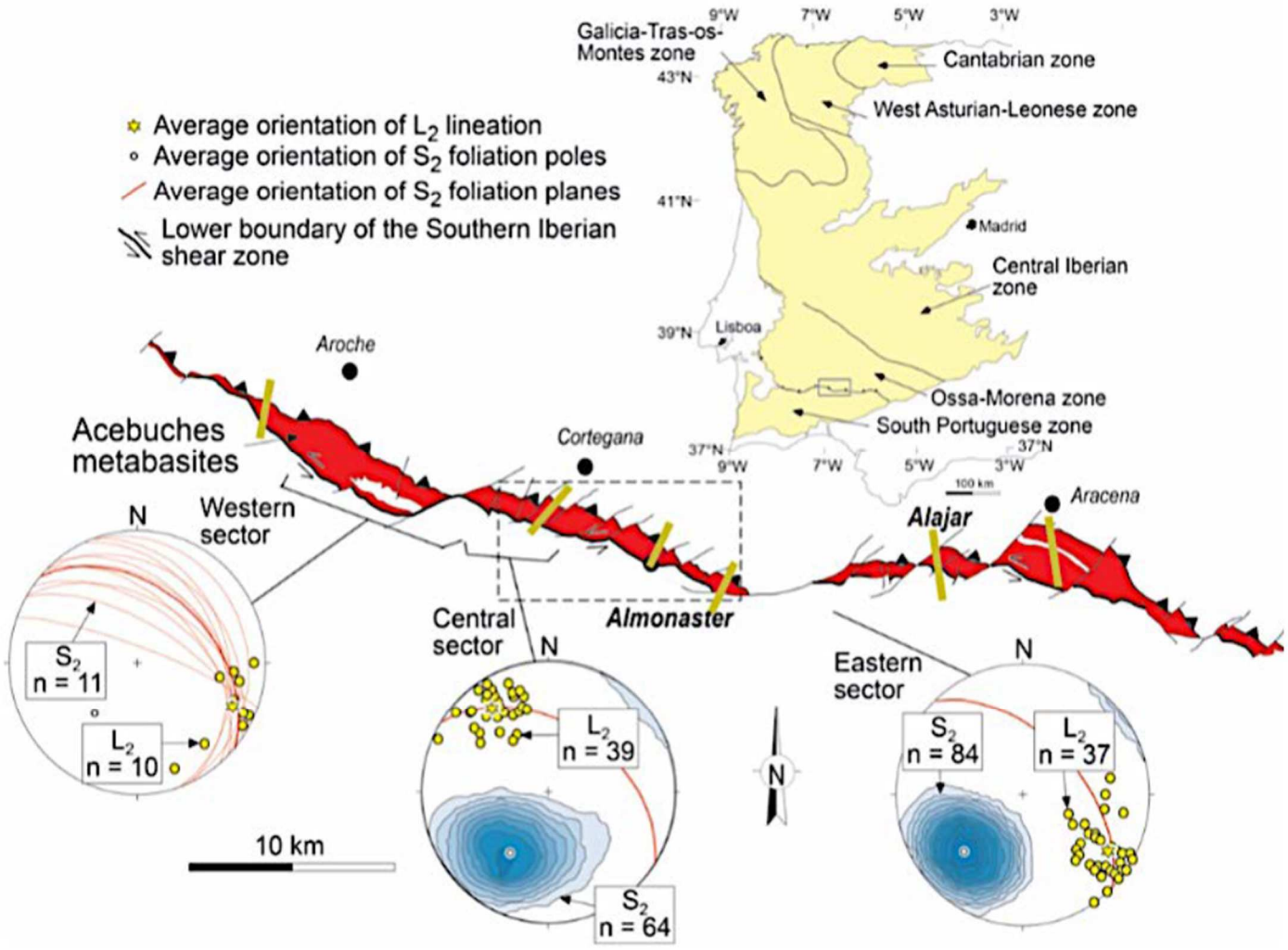

Figure 4: Simplified map of the western, central, and eastern sections of the Acebuches metabasites along the SISZ. The stereonets show the foliation and lineation data that correspond to each section during the second stage of deformation. From Fernandez et al., 2013.

2.2 Aracena Metamorphic Belt (AMB)

The AMB is located at the contact between the Southern Portuguese Zone (SPZ) and the Ossa Morena Zone (OMZ). The AMB is a high-grade metamorphic band that underwent high temperature/ low pressure metamorphism during the Variscan orogeny. The AMB is divided into two domains based on lithological, geochemical, metamorphic, and structural features. The

domains are split into a southern oceanic domain (OD) and a northern continental domain (CD). For this project, the area of focus is the oceanic domain. The oceanic domain is composed of two rock terranes, the Beja Acebuches metabasites (BAM) and the Pulo do Lobo accretionary prism (Fig 5).

2.2.1 Beja-Acebuches Metabasites

The northern side of the SISZ contains the Beja-Acebuches Metabasites (BAM) series, which have chemistry consistent with an oceanic crust with midocean ridge basalt (MORB) affinity (Bard and Moine, 1979; Castro et al., 1996). The BAM underwent two deformation events. The first deformation event consisted of high temperatures and low-pressure metamorphism. The upper structural portion is consistent with upper amphibolite facies with a strong metamorphic gradient, while the lower portion of this series underwent lower temperature metamorphism. This first deformational event is a result of the initial collision of the metabasites onto the continental margin (Castro et al., 1996).

The second deformational event is responsible for the juxtaposition of the BAM onto the PdL to form the suture known as the Southern Iberian Shear zone (SISZ). Based on ductile structures within the BAM, previous workers interpreted the kinematics of the SISZ to be oblique left-lateral transpression with variable oblique extrusion and a subhorizontal component of simple shear (Díaz-Azpiroz and Fernández, 2005; Fernández et al., 2013). The D_2 event affected the lower structural base of the metabasites and was accompanied by retrograde metamorphism that reached greenschist- lower amphibolite facies transition (Díaz-Azpiroz and Fernández, 2005; Stephenson, 2018). This grade of metamorphism is likely related to uplift and exhumation of rocks during the collision.

2.2.2 Pulo do Lobo

During the collision between Gondwana and Laurussia, an accretionary complex was formed along the margin of the Ossa Morena zone (Braid et al., 2012). This complex is known as the Pulo do Lobo domain and is typically interpreted as a suture zone of the final stages of the closing of the Rheic Ocean. However, there is some debate about the origin of the PdL, and some newer metamorphic evidence suggests it is part of the SPZ, perhaps being a remnant piece of Avalonia (Pérez-Cáceres et al., 2020; Díaz-Azpiroz & Fernández, 2021). The PdL domain consists of fault-bounded tectonostratigraphic units that strike east-west and dip steeply to the north. Within this domain, the lowermost units are metapelites, quartzites, and tectonic and sedimentary mélange. The uppermost units are varied siltstones and greywacke flysch sequence (Braid et al., 2010). Near the SISZ, the PdL contains interbedded metapelites and quartzites.

The PdL has a large-scale antiformal structure, however it is internally complexly deformed with various folds and thrusts at low grade metamorphic conditions. Strain within the PdL decreases with increasing distance from the SISZ (Carman, 2020). Strongly foliated schists and interbedded quartzites are closest to the shear zone (0-65 m) (Carman, 2020). These grade into moderately strained phyllites with complex geometries including S-C structures indicating thrust motion, shallowly dipping shear bands that cut the foliation at high angles, folds, and lozenges of quartzites surrounded by strongly deformed phyllites (65- 171 m) (Carman, 2020).

These rocks grade into low grade phyllites and slates with weak fabrics furthest from the SISZ (>172 m).

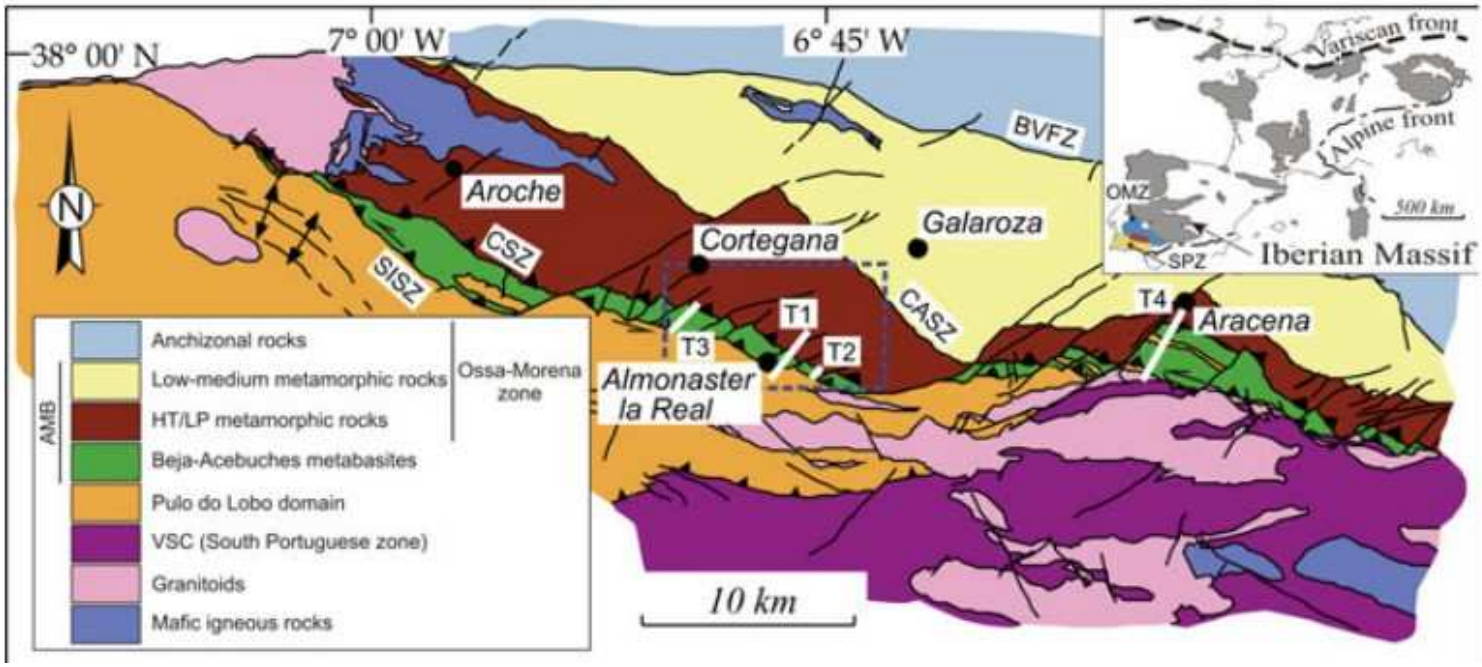

Figure 5: Generalized geologic map showing the SISZ and neighboring geologic units.
From Díaz-Azpiroz and Fernández, 2021.

2.3 Structural foundation of the SISZ

2.3.1 Structural Architecture

The SISZ roughly strikes 115° and dips around 50° to the NNE while displaying an imbricate structure displaying listric geometry. The activity of the SISZ is a result of the second deformation event, which results in the main structures of the SISZ. The D_2 event was a mylonitization event related to the development of the SISZ (Diaz Azpiroz and Fernández, 2005). The SISZ represents a very heterogeneously deformed shear zone that was accompanied by retrometamorphism that reached greenschist and amphibolite facies in the BAM. Toward the

structural base of the metabasites, D_2 increases, while grain size and porphyroclasts decrease with increasing distance to the structural top of the BAM.

Main structures of the SISZ consist of a penetrative foliation (S_2) and a related stretching lineation (L_2). The foliation is defined by the planar plagioclase and amphibole prisms, and, in the mafic schists, there is an addition of epidote-rich and chlorite-rich layers. The lineation is defined by the plagioclase aggregates and the long axes of prismatic amphibole porphyroblasts. Other structures of the SISZ include folds, the styles of which vary based on their distance to the structural base. Folds close to the structural base are much tighter than folds further from the shear zone. Asymmetric structures that are used as shear sense indicators in the SISZ are S-C and S-C' fabrics, asymmetric porphyroclasts, and ductile-brittle structures. All of these structures indicate a top-to-WSW sense of shear. The ductile-brittle structures consist of centimetric-scale reverse brittle faults, striae parallel to L_2, phyllonitic foliation, and C' planes (Diaz and Azpiroz, 2005). The existence of these structures suggests a progressive increase in finite strain from the upper to the lower boundary of the shear zone.

Transpression forms due to oblique collision and has a combination of simple shear (thrust and/or strike-slip) and pure shear (shortening across the zone). Fernández et al., (2013) expanded a procedure developed by Czeck and Hudleston (2003) to test the applicability of various transpression models to individual shear zones including the BAM affected by the SISZ. They found that the kinematics of the SISZ varied along strike, but generally could be explained by transpression with subhorizontal simple shear (shear plane dips less than 20°) and variable inclined extrusion directions with angles that vary between 0-80° from the dip of the shear zone (Fig. 6).

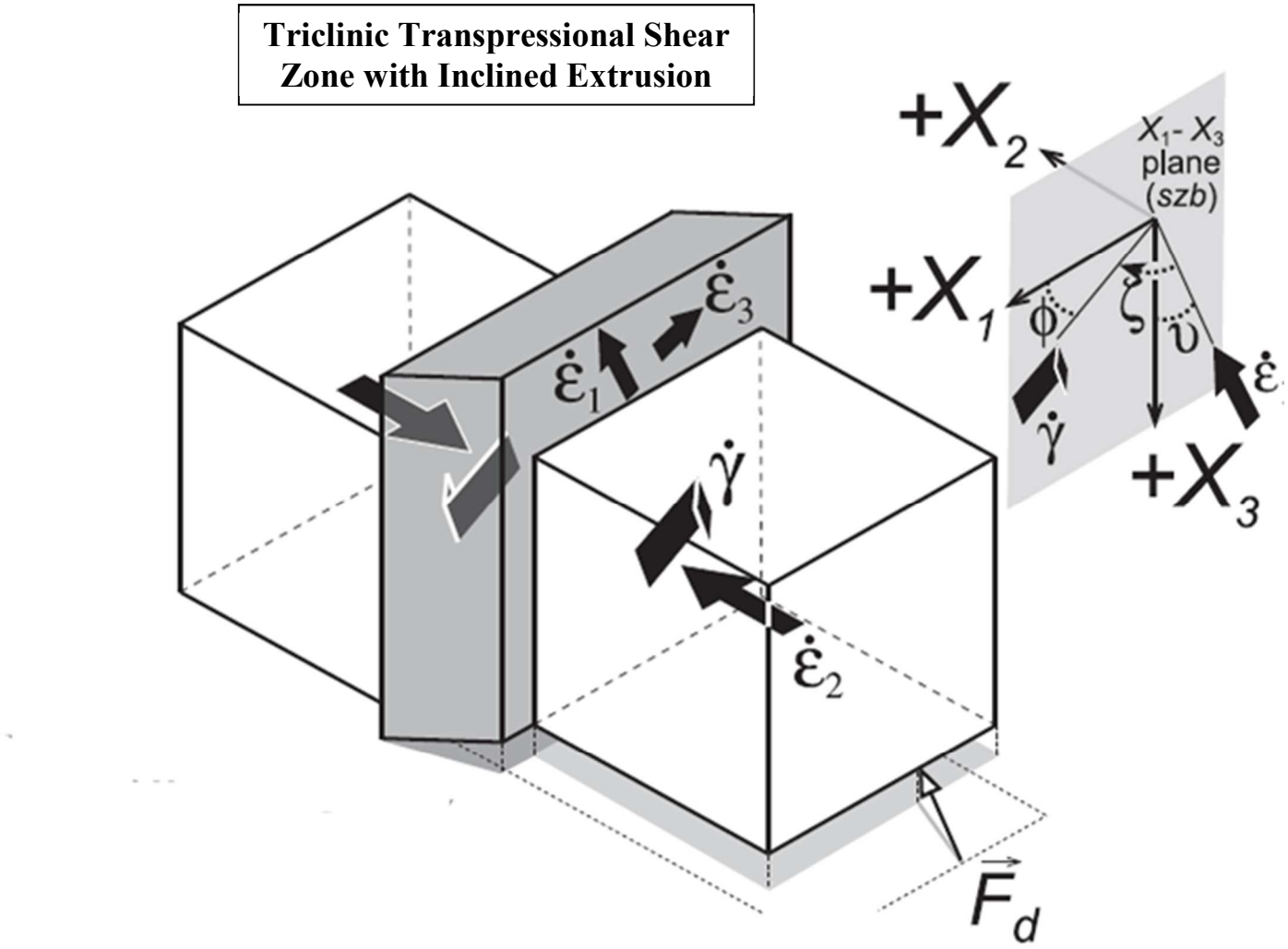

Figure 6: Model of triclinic transpression with inclined simple shear and inclined extrusion direction. Ẏ is the angle between the extrusion direction and the dip of the shear zone. ζ is the acute angle between the simple-shear direction and the extrusion direction. In the sign convention used here, ζ is negative as shown. X_1, X_2, X_3 are coordinate axes of reference frame with X_1 parallel to the strike of the shear-zone boundary, X_2 normal to the boundary, and X_3 is vertical. The three angles are coplanar and located in the surface coinciding with the shear-zone boundary (X_1-X_3 plane). Note that both the simple shear and the extrusion directions are parallel to plane X_1-X_3. Modified from Fernández et al., 2013

2.3.2 Fluid Flow

Recent geochemical and microstructural studies have uncovered that fluid was present during SISZ deformation within (Stephenson, 2018; Carman, 2020). Fluids are interpreted to have moved laterally across the shear zone (cross-fault flow) due to the enrichment of K_2O and

Al_2O_3 and depletion of SiO_2 in the BAM. This fluid likely flowed from the PdL accretionary prism (Stephenson, 2018). Evidence suggests that fluids used the shear zone as a conduit for fluid flow, while the SISZ itself was likely a leaky barrier to cross-zone flow. Fluids likely enhanced DMT and brittle processes close to the SISZ, and may have been responsible for at least some of the strain localization.

CHAPTER 3: Methods

3.1 Optical Microscopy and Point Counting

A general microstructural analysis was completed in the structural geology lab at the University of Wisconsin–Milwaukee. This analysis was completed using an optical microscope on 28 thin sections from Carman (2020). All thin sections are oriented on the presumed XZ plane of strain (perpendicular to foliation and parallel to a presumed down-dip lineation). The focus of this analysis is to determine the minerals, microstructures, and other important features such as shear sense indicators and fabrics present in each sample. The primary goal was to determine if there were microstructures that indicated dislocation or diffusional processes, and then perform further analyses to determine the relative importance of these mechanisms. A more detailed microstructural analysis on a select number of thin sections was completed by Carman (2020), which involved point-counting microstructures to quantify relative contributions of deformation mechanisms.

The mineral point count analysis was completed using an optical microscope in the structural geology lab at the University of Wisconsin-Milwaukee. An automated point counter was used with the software PetrogLite to create the map for each sample. 200 points were counted on each of twenty-four samples. The software automatically creates a grid to count 200 points for the whole sample using the dimensions of the sample on the thin section. Point counting was used to determine the concentration of quartz in each sample that will be used in later interpretations.

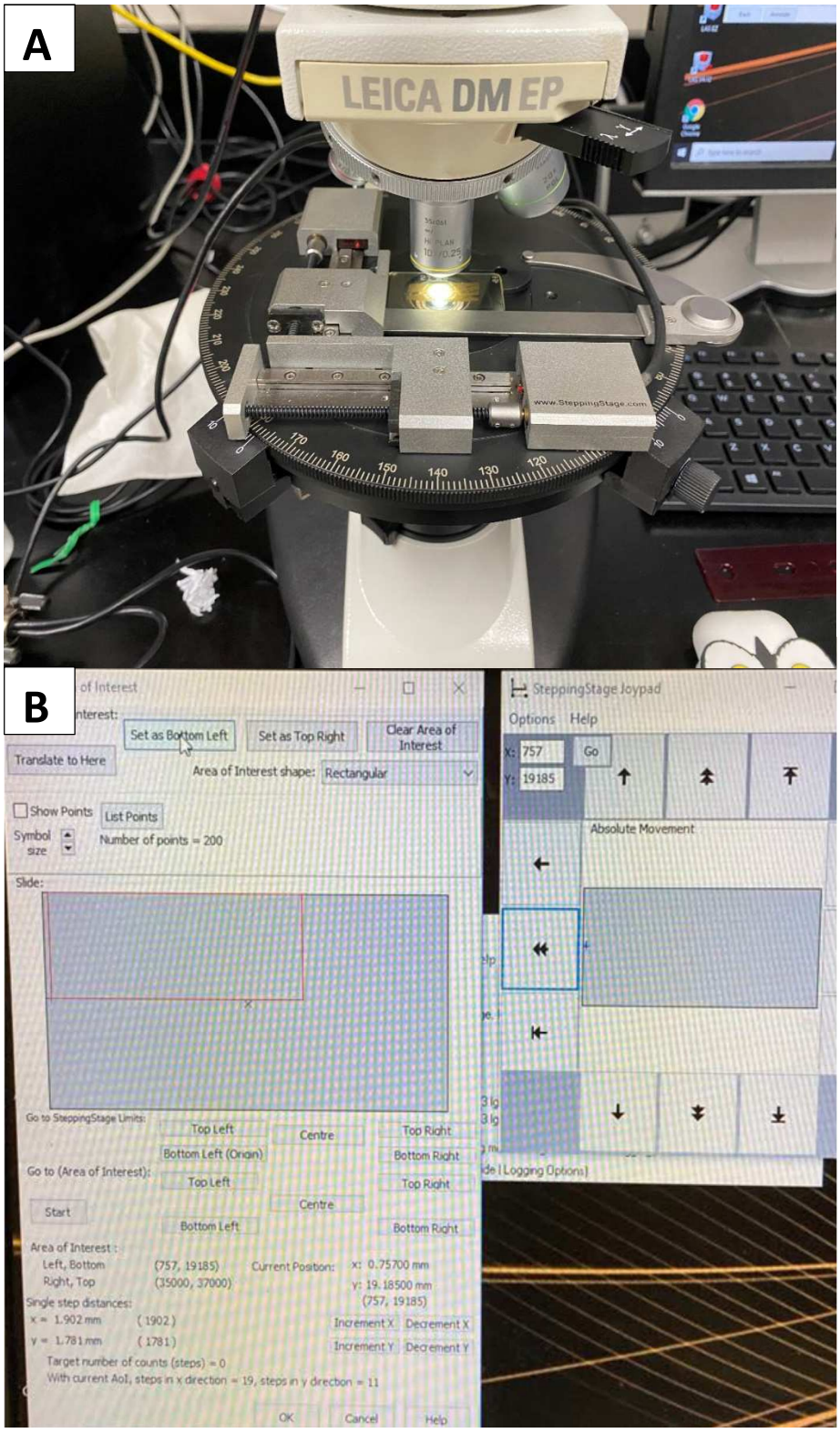

Figure 7: A) the setup utilizing an optical microscope with automatic stage used for the point count analysis. B) screenshots of the PetrogLite software that was used in the point count analysis.

3.2 Deformation Processes and Microstructures

Deformation processes microscale processes that result in change of shape or volume in a rock, and are often qualitatively classified as ductile or brittle. Generally, brittle processes occur in the upper to middle crust, and ductile processes occur in the middle to lower crust. The brittle-ductile transition may occur over a broad zone in which both these processes act. Both brittle and ductile processes are accommodated by several small-scale mechanisms. For ductile deformation, there are three groups of mechanisms: crystal plasticity also called dislocation creep, diffusion creep, and grain-boundary sliding (Vernon, 2004). For brittle deformation, the mechanisms include fracturing, frictional processes, or a combination known as cataclastic flow.

Deformation mechanisms are controlled by a myriad of variables such as mineralogy, temperature, pressure, stress, strain rate, grain size, and the presence and/or chemistry of fluids. In rocks, multiple mechanisms can act simultaneously, primarily because rocks are usually composed of multiple minerals, and the composition, structure, grain size, and orientation of minerals controls how they will deform. For example, the PdL metapelites contain quartz and mica; it is likely that quartz and biotite have different mechanisms acting on the grains.

Mechanisms may also change during deformation because location and conditions within the crust are likely variable during the duration of shear zone formation. For example, if a rock is exhumed from a higher temperature to a lower temperature, there will likely be evidence of brittle processes overprinting ductile processes. The addition of fluids, generally accelerate deformational processes and heavily impact which deformation mechanisms will act on a mineral. Deformation mechanisms are identifiable by several characteristic microstructures that can be identified petrographically.

Frictional and fracturing processes play a role in deformation processes in the upper crust, known as the brittle regime. Frictional processes occur when grains slide past each other without causing fractures in the grains. This sliding depends on loss of cohesion and overcoming friction between grains. Fracturing processes are a type of deformation that forms fractures and allows movement along the fractures. Cataclastic flow, also called cataclasis, is deformation that occurs from combined frictional and fracturing processes. Microfractures, broken grains, and displacement on cleavage are microstructures that provided evidence of cataclastic flow (Vernon, 2004). Extensive cataclastic flow results in grain size reduction. These mechanisms are typically active in conditions of lower temperatures and lower pressure, consistent with shallower depths, as well as high fluid pressure.

Ductile deformation is permanent deformation without loss of cohesion, which can be accommodated by several processes including crystal plasticity. Crystal plasticity is the internal distortion of grains due to the movement of dislocations, or line defects. Dislocations form and move with applied stress. Dislocation motion requires intracrystalline slip, and will occur more easily along weak planes in the crystal lattice. Slip along these weak planes is called dislocation glide. Both dislocation glide and deformation twinning cause changes in a grain because one part of the crystal shears with respect to its neighboring part (Vernon, 2004). Preferential intracrystalline slip along weak planes cause some minerals within a rock to deform more easily than others, resulting in the formation of crystallographic preferred orientations. Crystal plasticity is usually the dominant process at conditions associated with the middle to lower crust (Rahl and Skemer, 2016). Typical microstructures associated with crystal plasticity include undulose extinction, kink bands, deformation lamellae, and deformation twins.

Crystal plasticity has recovery mechanisms that are necessary to keep dislocation glide operational. Without recovery mechanisms, dislocations tangle, internal energy of a grain increases, and deformation undergoes strain hardening. Dislocation climb is a mechanism that allows the movement of dislocations out of their slip planes, with the addition or removal of defects through a small amount of diffusion. Dislocation climb may form subgrain boundaries that are visible under optical microscope. Dynamic recrystallization is a recovery mechanism that forms strain-free volumes in deformed grains, by creating and/or moving grain boundaries (Vernon, 2004). Microstructurally, this can be seen as aggregates of new grains that are typically much smaller than the surrounding grains. In quartz specifically, microstructures known as "necklaces" form in which larger grains are surrounded by recrystallized grains.

In diffusion creep, diffusion of chemical components allows material to move through the rock and may result in grain shape changes. Diffusion creep occurs either by aqueous solution (dissolution-precipitation creep or diffusive mass transfer, DMT) or by solid state diffusion along grain boundaries ("Coble creep") or within grains ("Nabarro-Herring creep") (Vernon, 2004). Diffusive mass transfer generally occurs in the upper to middle crust at low metamorphic grades. Solid state diffusion occurs in the lower crust where there are high temperatures. Multiple microstructures form during diffusion creep including selvage seams of residual material, indented grains, overgrowths, and a lack of crystallographic orientations. These microstructures form in either DMT or solid state diffusion.

Ductile grain boundary sliding involves relative grain movement along grain boundaries without loss of cohesion. This mechanism typically occurs without the presences of fluid. Along the SISZ, this mechanism is less likely to be present due to presence of fluids.

Several types of microstructural and metamorphic evidence indicate the presence of syndeformational fluid. For example, all microstructures formed by diffusive mass transfer including selvage seams, indented grains, and overgrowths likely required fluid. Many metamorphic reactions require addition of fluids, and alteration patterns can be assessed for fluid input as well.

3.3 Crystallographic Preferred Orientations (CPO)

Various crystallographic orientations of minerals (in this study, the c-axis and grouped a-axes of quartz) can be plotted on stereographic plots to determine whether there are Crystallographic Preferred Orientations (CPOs). CPOs typically form from dislocation creep processes, and are dependent on a variety of factors, such as slip system, grain orientation, temperature, recrystallization processes, stress, and strain. CPO patterns form due to changes in the crystallographic orientations of mineral grains during crystal plasticity (Fossen, 2016). Predictable CPO patterns within a particular mineral form due to slip systems that are controlled by crystallography (Fig. 9). Most modern studies use electron backscatter diffraction (EBSD) to map crystallographic orientations across thin sections (e.g., Toy et al., 2008; Thigpen et al., 2010; Fazio et al., 2017; Kruckenberg et al., 2019; Chen et al., 2022).

Quartz has four slip-systems that can be active, either individually or simultaneously, and each form a characteristic CPO pattern (Fig. 1). Slip systems are activated at certain temperatures during deformation, so CPO patterns can also give an indication of temperature during deformation. CPOs may weaken parts of the rock, causing deformation localization.

The presence and strength of CPO fabrics can be used to interpret the relative importance of crystal plasticity versus other deformation mechanisms. Samples will display CPO patterns if

dislocation creep was active. If no patterns are present, then it likely indicates diffusion, brittle processes, and/or grain boundary sliding dominated. If multiple mechanisms were active including dislocation creep, CPO patterns may form, but not be as strong as cases when crystal plasticity dominated.

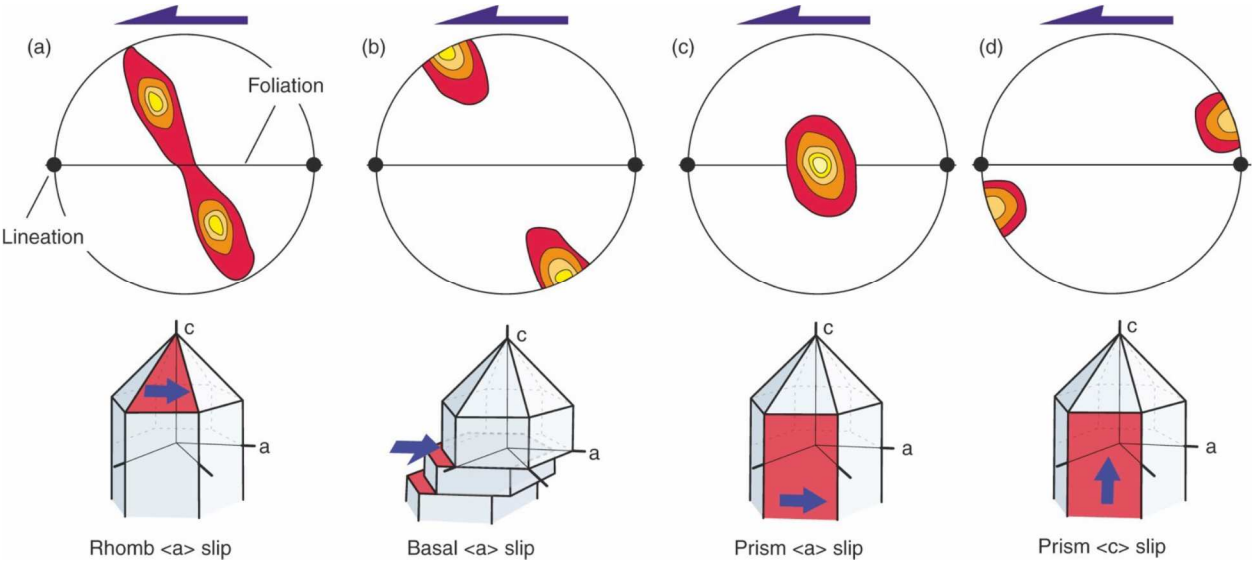

Figure 8: CPO plots with patterns that correspond to a certain slip system in quartz. From Fossen, 2016

3.4 Electron Backscatter Diffraction (EBSD)

For this project electron backscatter diffraction (EBSD) was completed by Bil Schneider at the Geoscience Department at the University of Wisconsin-Madison. To analyze crystallographic preferred orientation (CPO) of quartz grains, EBSD was used to map regions on 24 oriented thin sections using the Hitachi S3400 Variable Pressure Scanning Electron Microscope with the Oxford EBSD system. All samples were coated in 1 nanometer of Iridium and indexed using a step size of 1 um, a 30.0 kV with a specimen tilt of 70 degrees. The map size

and step size were selected for each sample based on finding appropriate values that yielded a high resolution map with a large number of quartz grains indexed. The indexed data was transferred into MATLAB to determine if the data were sufficient for reliable quartz CPO plots. If maps did not contain enough data points for reliable plots, the map size was slightly increased with a higher resolution. The map sizes and step sizes varied between samples due to differences in mineralogy and grain size. Each sample was indexed for quartz which was the only indexable mineral present in large quantities. The only other minerals of significant quantities, biotite and muscovite, do not index well in EBSD. Generally, maps were created in the most quartz-rich regions of the thin sections to obtain the highest number of indexed grains possible.

To determine which indexed points comprise individual grains, MATLAB uses a code that only focuses on the indexed points and ignores the unindexed points. To determine quartz grain boundaries, a grain reconstruction is performed. The rock microstructure of raw EBSD maps are revealed through a grain reconstruction algorithm that calculates the location of grain boundaries based on a misorientation angle of 10° relative to neighboring EBSD solutions (Kruckenburg et al., 2019). After this procedure, potential spurious grains are removed if they had less than 3 solutions. The number of grains that result from this process are used to construct CPO and CVA figures described below.

Figure 9: The Hitachi S3400 Variable Pressure Scanning Electron Microscope with the Oxford EBSD detector (on the left). The computer software is used to select the location in the thin section that will be indexed.

3.5 Creation and analysis of crystallographic preferred orientations

.

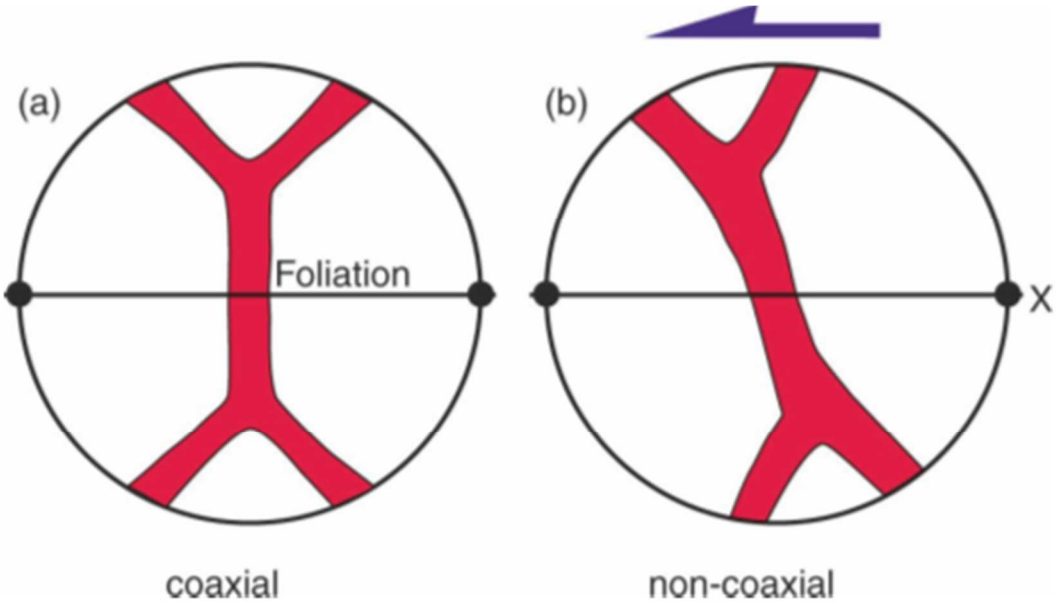

Figure 10: These schematic quartz c-axis plots show the differences between the crossed girdles of coaxial and non-coaxial deformation. Plots are drawn in a specimen fabric reference frame with foliation rotated to an EW, vertical plane and X = lineation which is rotated to an EW horizontal line. From Fossen, 2016

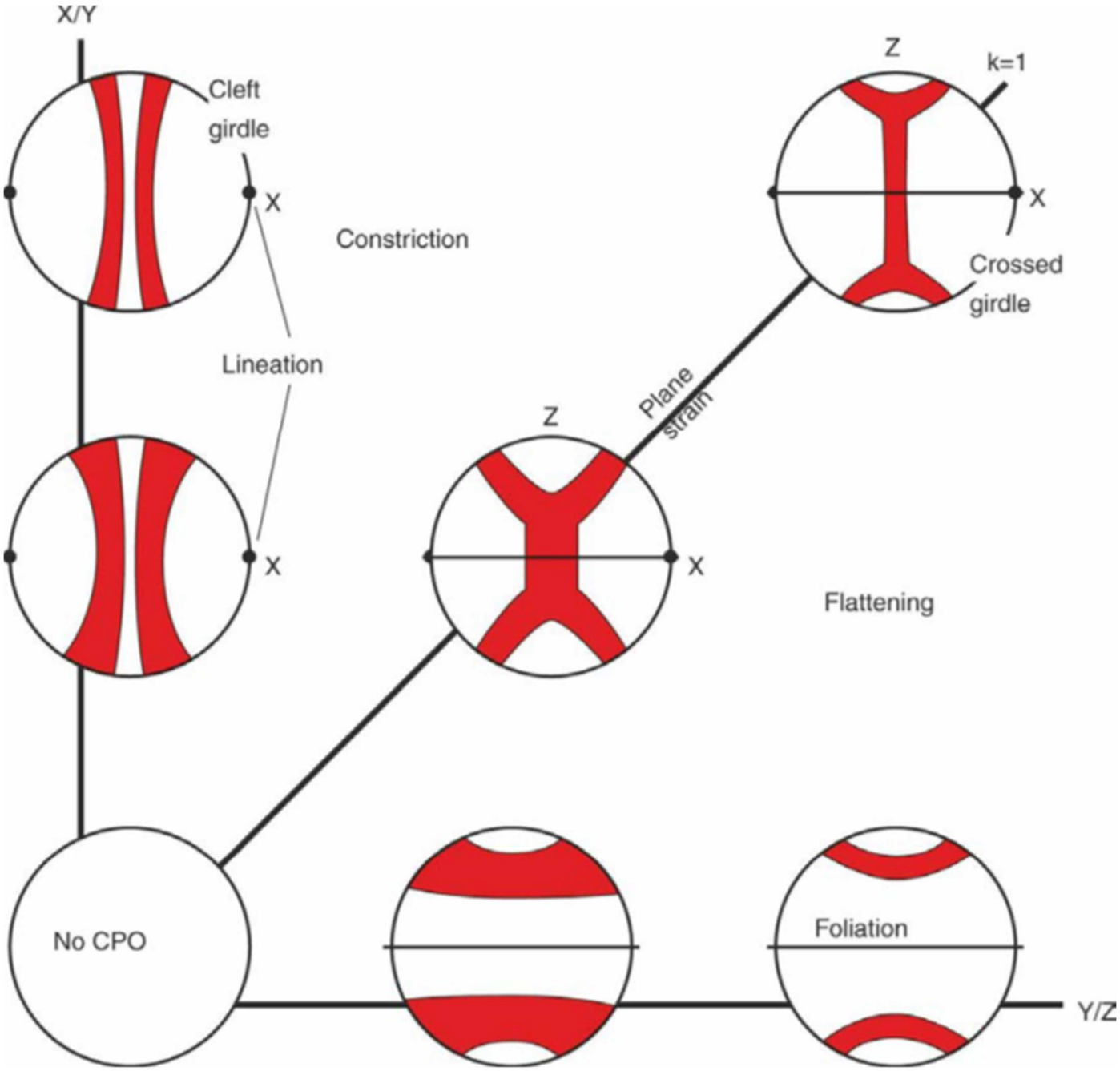

Figure 11: Patterns that are used to determine the relationship between quartz c-axis CPO patterns and strain. Plots are drawn in a specimen fabric reference frame with foliation rotated to an EW, vertical plane and X = lineation which is rotated to an EW horizontal line. From Fossen, 2016

Once the grains are reconstructed to create CPO plots, MATLAB then plots and contours the crystallographic orientations on a stereonet. If the stereonets have any pattern or preferred orientation, dislocation processes likely occurred during deformation.

To understand the importance of the pattern that emerged in these plots, the M-index has been calculated. This measurement focuses on the distribution of misorientation angles which are angles of rotation around an axis to bring two crystal lattices into the same orientation (Skemer et al, 2005). The M-index records the shift towards low angles as deformation and CPO development increases. The lower the angle that is determined, the more aligned the grains. The higher the M-index value, the stronger the pattern. This value helps to evaluate the relative importance of dislocation vs diffusion processes. If the number is low (less than .01), then the pattern is weak and indicates more diffusion than dislocation.

The shape and orientation of the CPO figures is used to determine active slip systems in quartz grains (Okudaira et al., 1995; Toy et al.,2008; Barth et al.,2010; Passchier and Trouw, 2005; Rahl and Skemer, 2016; Dutta and Mukherjee, 2020). Figure 11 shows the patterns of quartz c-axis and a-axis that are associated with a certain slip system in quartz (Jerábek et al., 2007). The slip systems are also used as an indicator for the temperature of deformation. Each slip system has a corresponding temperature that will allow its activation. In addition to the c-axis and a-axis pole diagrams, an inverse pole figure of the misorientation axes was created for each sample. The inverse pole diagram shows a point maximum that indicated which slip system was active at the time of deformation (Fig. 12).

CPO diagrams of quartz c- axis and a-axis were used to evaluate the kinematic parameters of the SISZ. CPO patterns can help to identify how much pure shear versus simple shear occured based on the opening angles of the patterns from the CPO plots. Non-coaxial

deformation has CPO patterns that are asymmetrical (Passchier and Trouw, 1998; Fazio et al., 2017). For coaxial deformation, the CPO patterns have a symmetrical pattern (Fig. 9). CPO patterns can also be used as a guide to determine strain geometry. Pole figures that are created from the CPO data are defined by a variety of terms such as cleft girdle, crossed girdles (Fig. 10), and a point maximum.

The patterns that emerged from the crystallographic orientations of quartz were also used to determine the amount of flattening and constriction the PdL underwent during deformation (Fig 10). The patterns in figure 10 are typical patterns that are generated from quartz CPOs, however, the CPOs in this study were atypical of these, so other studies that have atypical CPO patterns have been used to understand the kinematic parameters of the SISZ (Chen et al., 2022; Renjith and Mamtani, 2014; Parsons et al., 2016; Goswami et al., 2018; Fukuda et al., 2018; Barth et al., 2010; Takeshita and Hara., 1997; Cross et al., 2017). Overall, CPO patterns are a combination of active slip-systems and kinematics. Figure 13 shows theoretical patterns predicted for several possible combinations.

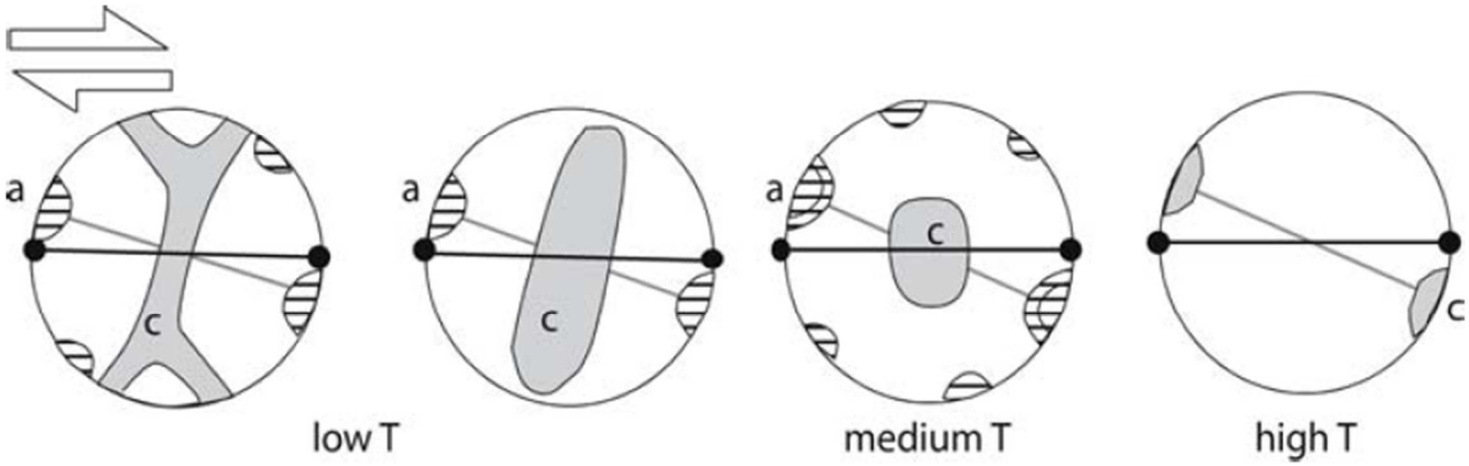

Figure 12: Expected patterns from a-axis and c-axis CPO plots that are used to infer the active slip systems during deformation. The areas with lines are the expected a-axis orientation from the CPO plots. The solid gray is the corresponding pattern produced by the c-axis CPOs. Temperature increases from right to left. From Passchier and Trouw, 1998

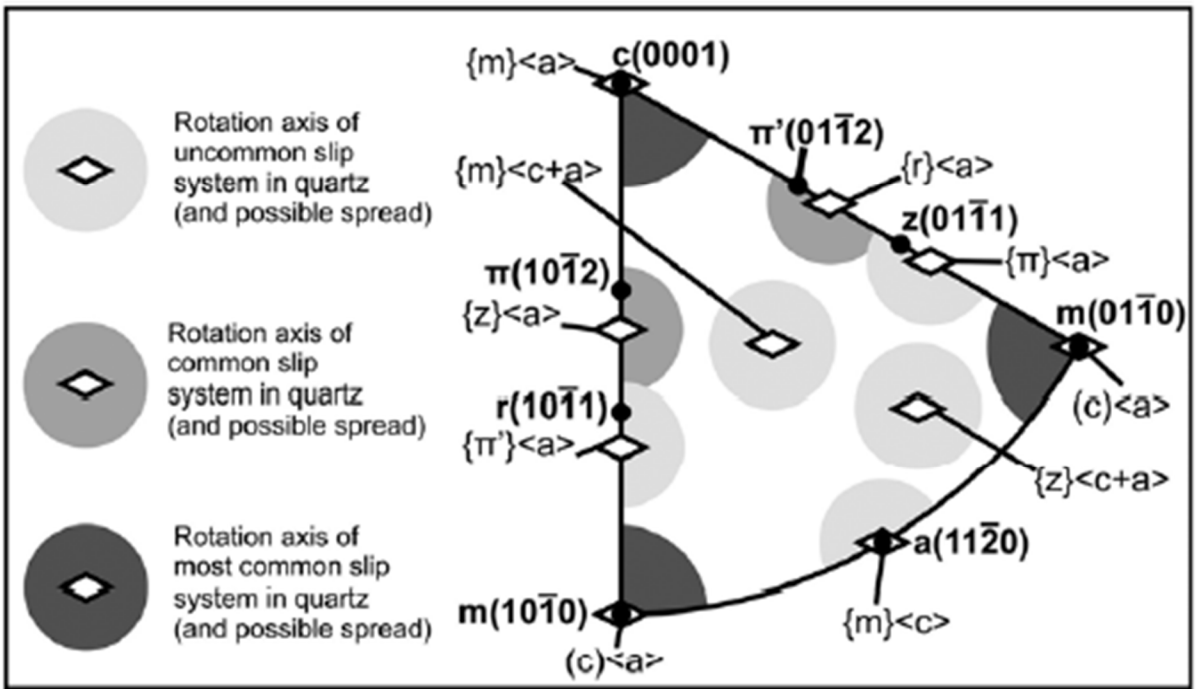

Figure 13: An inverse pole figure of the misorientation axis that show the active slip system and their corresponding point maximum. The light gray point maximum are the least common slip systems in quartz and the dark gray is the most common slip systems in quartz. From Papeschi and Musumeci, 2019

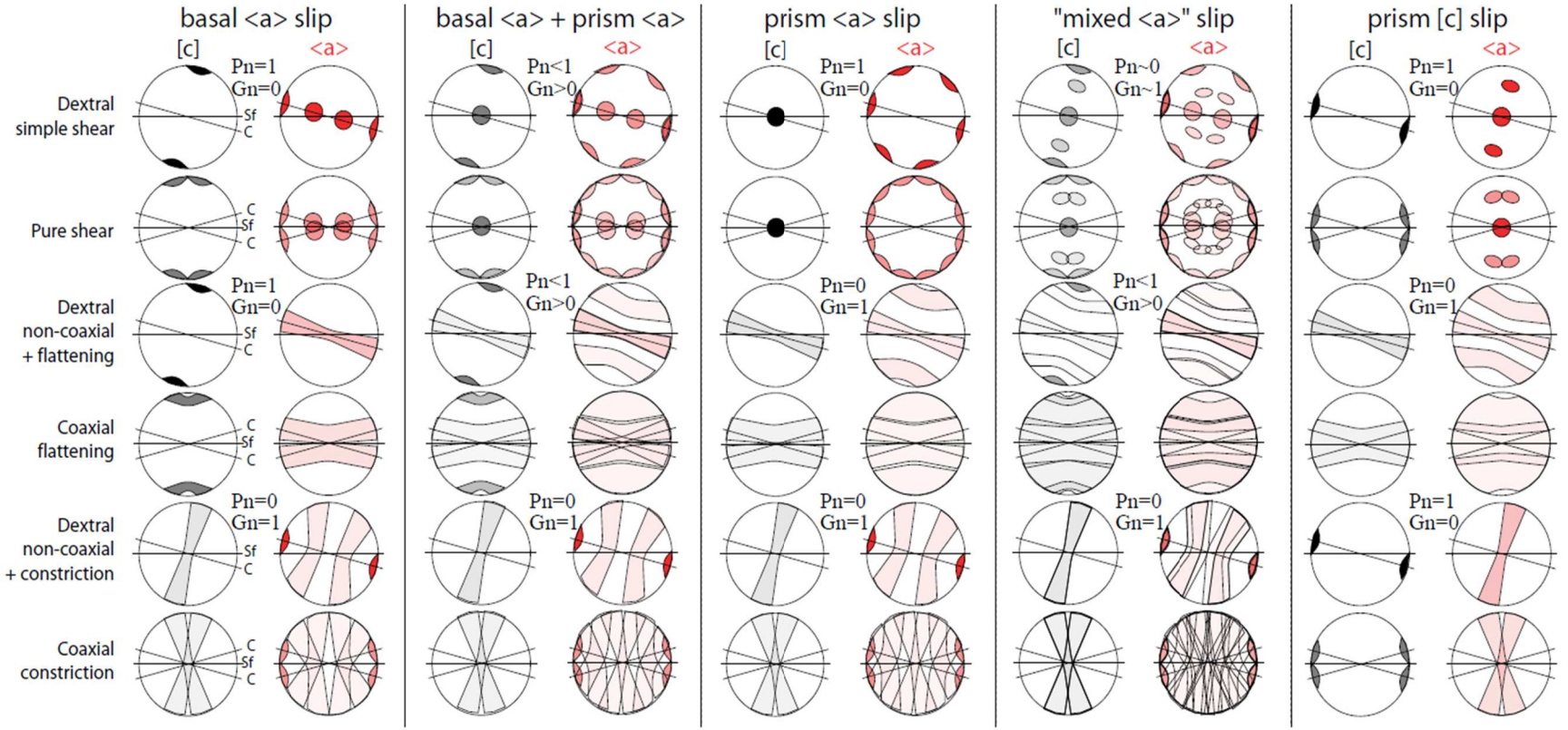

Figure 14: The associated CPO patterns of both c-axis and a-axis of quartz that demonstrate the active slip system and the corresponding kinematics. The plots with the black and gray girdles and point maximum are represent the c-axis of quartz and the red are the a-axis of quartz. Pn is the normalized point the Gn is the girdle4 indices expected for quartz slip systems. The foliation plane is the horizontal line, and the lineation is the intersection of the primitive and the foliation plane. The C planes are the inclined lines on the plots. From Barth et al., 2010

3.6 Crystallographic Vorticity Axis Analysis

Crystallographic vorticity axis (CVA) analysis is a relatively new method that can be used to find the orientation of the vorticity vector (Michels et al., 2015), which allows one to constrain the orientation of the noncoaxial strain component of the overall deformation. This method uses rotational statistics to analyze crystallographic orientations inside individual grains (Michels et al., 2015; Kruckenberg et al., 2019). A CVA analysis calculates the best fit rotation axis from numerous crystallographic orientations within a grain.

CVA analysis was completed using a custom code developed by Michels et al. (2015), which was created from the MTEX toolbox and other codes. The code was downloaded from GitHub (https:// github .com /zmichels /CVA) and run through MATLAB in a similar fashion that the EBSD data was processed for the crystallographic preferred orientation.

CVA plots are expected to have the bullseye in the middle of the plot (perpendicular to the lineation), because the thin sections are interpreted to be cut along the vorticity normal section (VNS). However, due to unknown lineations in the field, not all thin sections were cut along the VNS. If the CVA plotted as the bullseye in the middle, it means that the thin section was cut along the VNS. Because the thin section was cut along the VNS, the shear sense and kinematics can be determined by using the CPO plots in addition to the CVA. For CVA pole figures that did not produce a bullseye in the middle, a rotation was applied. The rotation is important because the rotation is also applied to the c-axis and the a-axis CPOs. This helped to make valid interpretations on the kinematics at each sample area. This was completed in Matlab using the same data for the original CVA analysis. The code is provided in the appendix.

The CVA analysis provides a preferred vorticity axis (Michels et al., 2015). To determine the preferred vorticity axis, the crystallographic vorticity axis from individual deformed grains

were isolated to calculate the best-fit grain scale crystallographic vorticity axis by using neighbor-neighbor misorientations greater than 10° from the electron back scatter maps (Michels et al., 2015). This process was completed in MATLAB using a code from GitHub (https:// github .com /zmichels /CVA).

There are two rotations that were applied to the CPO and CVA. The first rotation that was applied was a rotation to place the vorticity vector in middle of the stereonet so kinematics could be evaluated in the VNS. To better understand the SISZ kinematically, samples that had a foliation and lineation measurement from the field were also rotated into their geographic reference frame to see the kinematic changes across the PdL.

CHAPTER 4: Results

4.1 Optical Microscopy Analysis

The analyzed rocks are classified as phyllites/schists and quartzites, with some gradation between the types. The minerals contained in the phyllites are mainly biotite, muscovite, and quartz with lesser amounts of plagioclase, zircon, and one single staurolite grain. Furthest from the SISZ, the phyllites are very low grade, and could even possibly be classified as slates. The phyllites grade into schists closer to the shear zone boundary. The schists generally have the same mineralogy as the phyllites but also have garnet porphyroblasts near the shear zone. The quartzites consist of almost entirely quartz with trace amounts of mica. All schist and micas have a bimodal grain size. The general matrix includes quartz and micas of very similar grain sizes. Quartz that was not part of the overall matrix tended to have a larger grain size. The quartzites except for sample SI-92Q have a bimodal grain size between the matrix and large quartz. Sample 92Q can be paired with the phyllites and the schists because this sample contains about 50% micas and 50% quartz, where the other two quartzites have 90% or more of quartz. The grain size across all schists and phyllites are generally in the same range from 2 microns to 50 microns. There are a few grains in each sample that are larger than 50 microns, but those are rare. The quartzites have a slightly large grain size than the schist and the phyllites. The range is generally 10 to 100 microns. A majority of the grains range from 10 to 40 microns in the quartzites whereas in the phyllites, it was more common to have a range of 2 to 10 microns.

Point count analysis reveals the relative mineral abundances in the samples. Samples that are classified as quartzites (3 samples) are composed mainly of quartz. The phyllites and schists were mainly composed of micas and quartz was in lower quantities (Fig 22). Phyllites and schists

typically range from 30 to 65% quartz and 30 to 65% micas. If there was a lower amount of mica, there would be a large quartz composition and vise versa. Two quartzite samples contain about 95 percent of quartz with trace amounts of micas. The other quartzite sample (92Q) has about 50% of quartz and 50% of micas, but it is interpreted as a quartzite. There were not any trends of lithology when increasing the distance from the shear zone boundary, but chlorite tends to be in samples closer to the shear zone boundary.

Samples with at least 30% micas contained a well-developed foliation. The foliation is caused by the alignment of the micas and even some quartz grains are elongated in the foliation direction. The quartzite samples with ~95% of quartz had a very weak to no foliation. The micas also tend to pin the quartzite grains and caused them to elongate in the same direction of the micas. Most, if not all samples contain strain shadow tails that were used as shear sense indicators. The S-C fabrics were also used as a shear sense indicator. These indicators indicated a top to SW shear sense throughout most samples. Overall, the findings in this study match the findings in Carman (2020).

The microstructure analysis uncovered a variety of microstructures. All samples had similar microstructures. In the schists, there were extensive microstructures in quartz grains, including bulging, subgrains, triple junction boundaries, undulose extinction, migrating grain boundaries, fluid inclusions, and deformation lamellae (Fig. 14, 15, and 17). Plagioclase feldspar contained a few microstructures including intragranular fractures and deformation twins (Fig. 16). Strain shadows formed around the feldspar clasts, some quartz clasts, and garnet (Fig. 20). Biotite and muscovite are the fill material for strain shadows and in some cases. quartz fills the shadows as well. Garnet and plagioclase were only present in the schists within the first 60 m of the shear zone boundary. Biotite and muscovite formed crenulation cleavage in almost all

samples, regardless of distance. There are some mica kinks that formed in samples, but this was not common (Fig. 18). The schists and some phyllites also contain chlorite (Fig. 21). Solution seams form around clasts of quartz, felspars, and garnets, but there were also some within the matrix.

Almost all the microstructures found within the schists also were found within the phyllites (Fig.19). Grater than 60 m from the SISZ boundary, deformation lamellae decreased in quantity or were nonexistent. The grain size also decreased likely due to recrystallization. Most of the strain shadows and dissolution seams formed around clasts or aggregates of quartz. Throughout the PdL, there was folding and fracturing that occurred as well as veins and boudinage.

Quartz within quartzites contained the same assemblage of microstructures found in the schists and phyllites. There was some occasional pinning of quartz by micas, and dissolution seams were present.

With all the microstructures present, there is evidence of three processes occurring. Dislocation processes are indicated by deformation lamellae, undulose extinction, triple junctions, and many more. There were plenty of diffusional mechanisms occurring as seen by the strain shadows, dissolution seams, and fluid inclusions. There were some brittle processes such as intragranular fractures, boudinage, and folding.

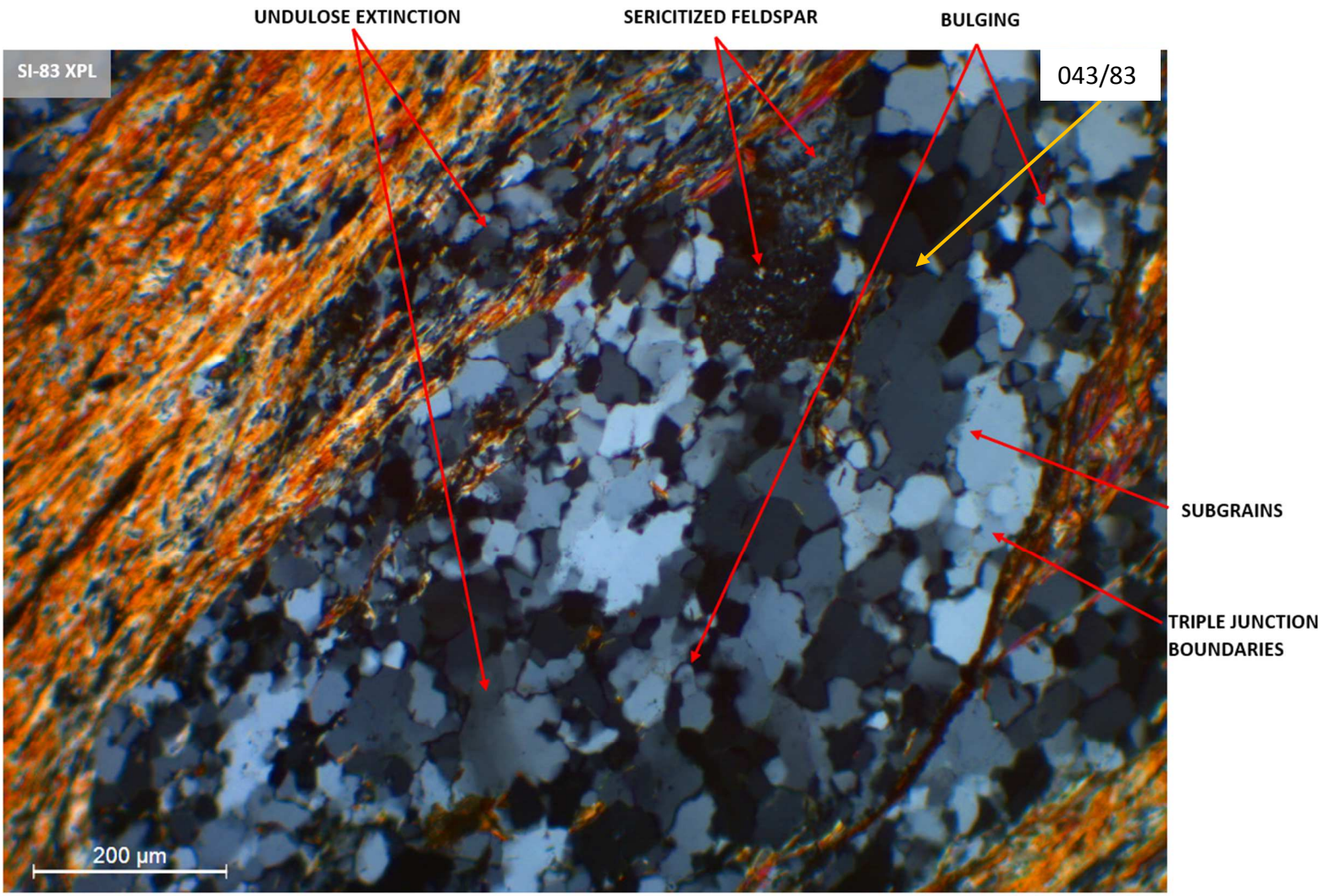

Figure 15: Selected area of SI-83 (Schist) thin section, XPL. Distance from the shear zone is 7.2m. The orientation of the long axis is shown in the top right corner (trend/plunge) (orange arrow). Quartz microstructures include undulose extinction, bulging, subgrains, triple junction boundaries. Feldspar microstructures are sericitized feldspar

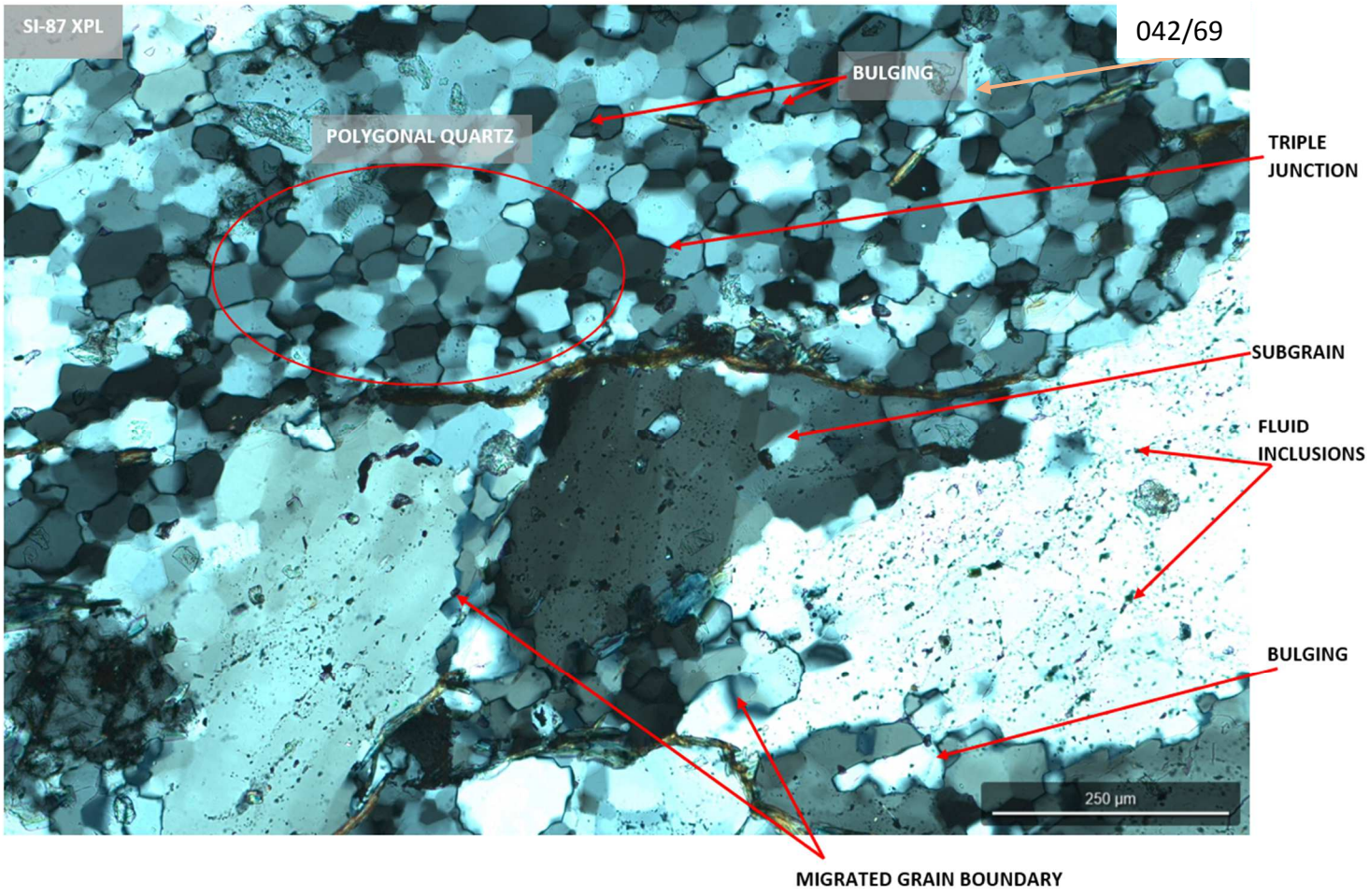

Figure 16: Selected area of SI-87 (Schist) thin section, XPL. Distance from the shear zone is 16.1m. The orientation of the long axis is shown in the top right corner (trend/plunge) (orange arrow). Quartz microstructures include polygonal quartz, bulging, subgrains, triple junction boundaries, migrated grain boundary, fluid inclusions.

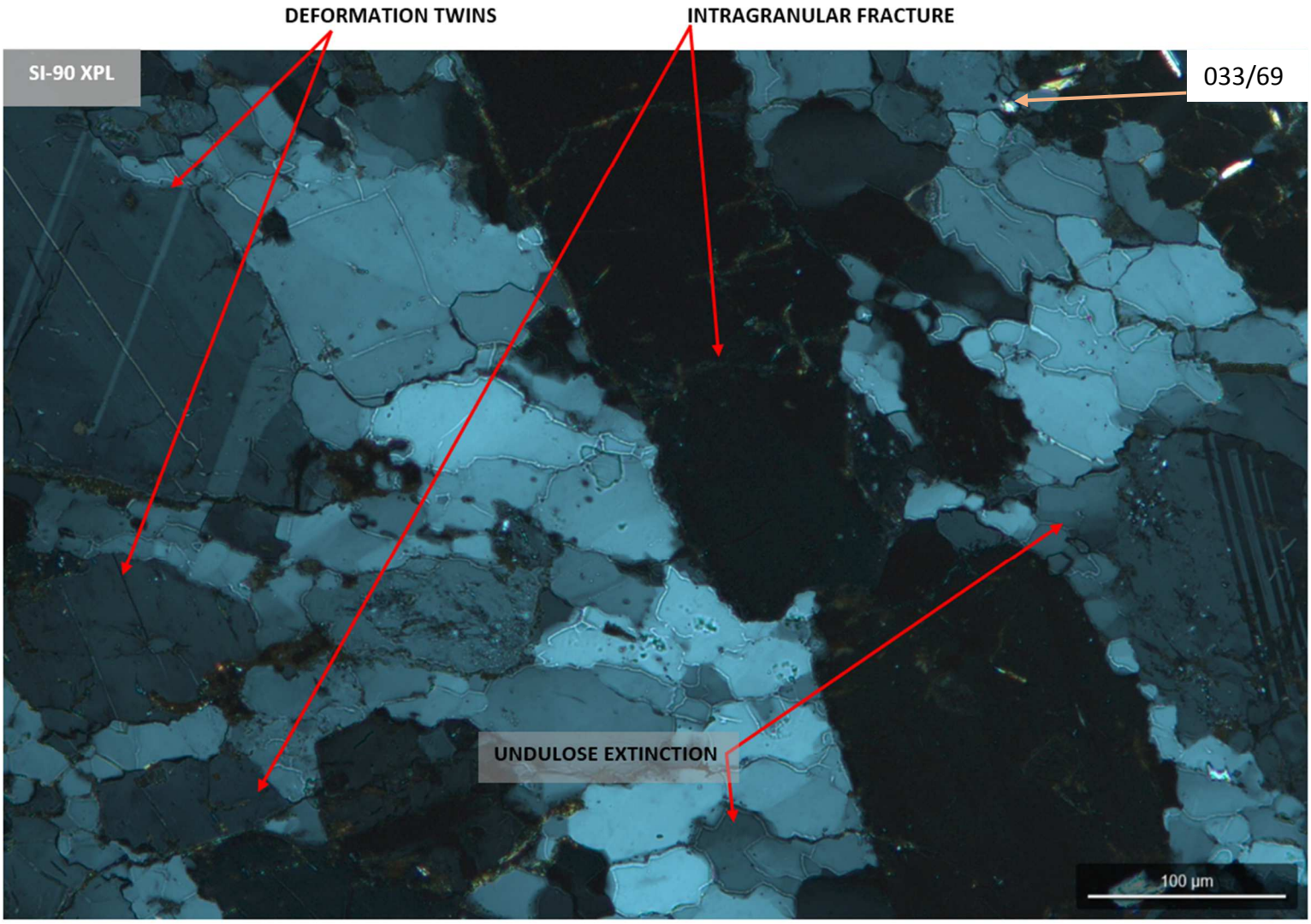

Figure 17: Selected area of SI-90 (Phyllite) thin section, XPL. Distance from the shear zone is 23.8m. The orientation of the long axis is shown in the top right corner (trend/plunge) (orange arrow). Quartz microstructures include undulose extinction and deformation lamellae. Feldspar microstructures include intragranular fracture and deformation twins

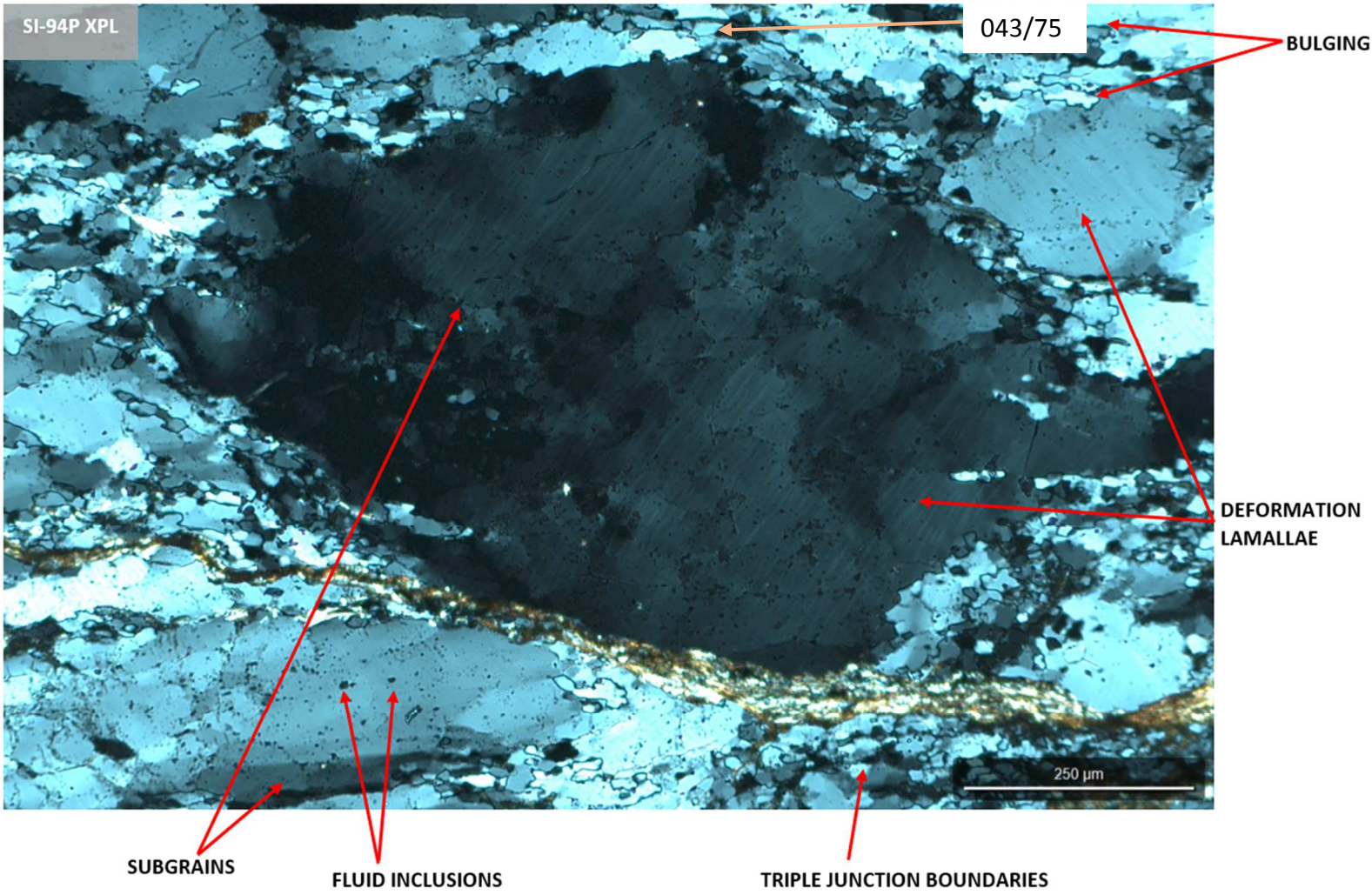

Figure 18: Selected area of SI-94P (Phyllite) thin section, XPL. Distance from the shear zone is 56m. The orientation of the long axis is shown in the top right corner (trend/plunge) (orange arrow). Quartz microstructures include bulging, subgrains, triple junction boundaries, deformation lamellae, fluid inclusions.

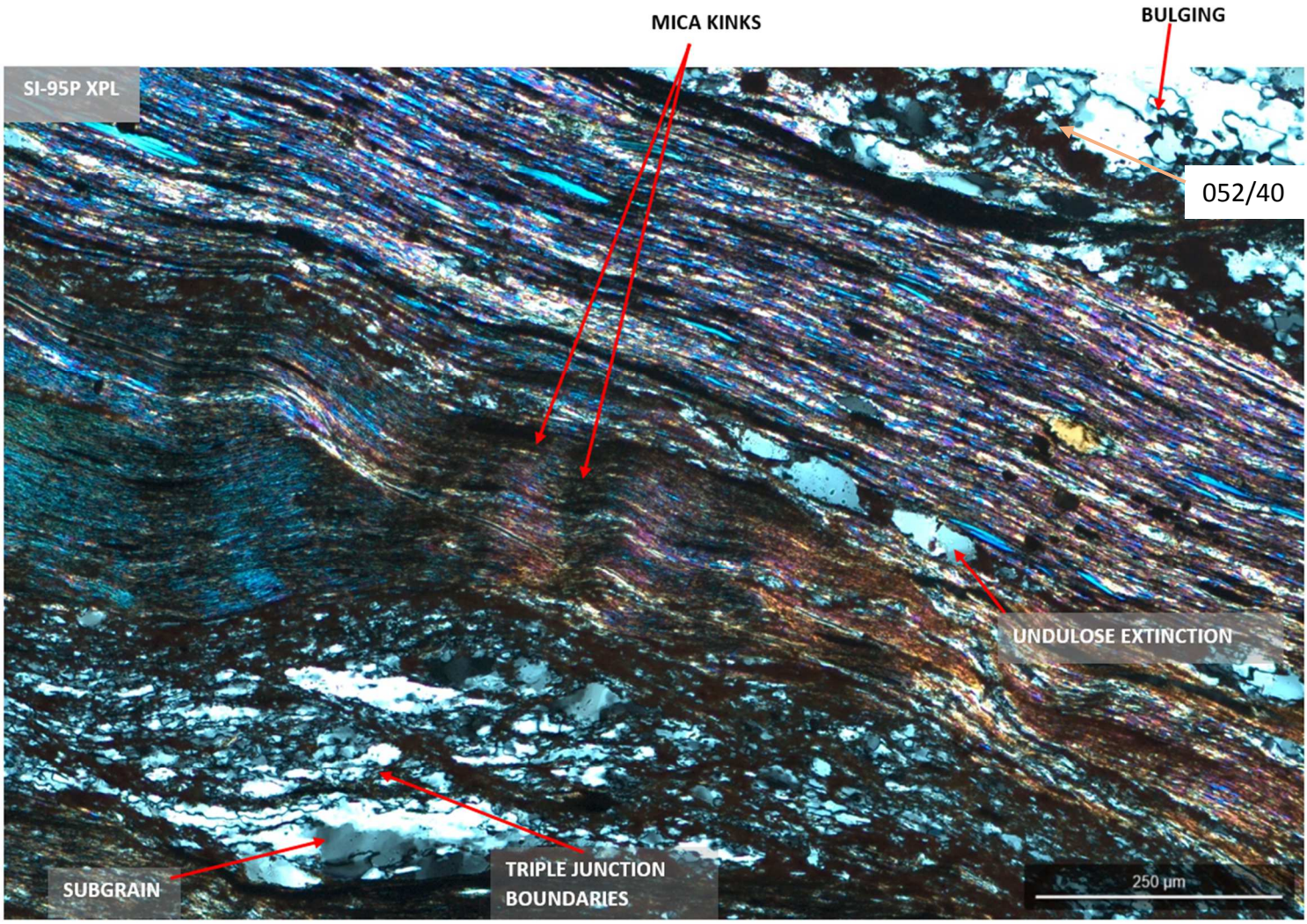

Figure 19: Selected area of SI-95P (Phyllite) thin section, XPL. Distance from the shear zone is 71.3m. The orientation of the long axis is shown in the top right corner (trend/plunge) (orange arrow). Quartz microstructures include bulging, subgrains, triple junction boundaries, undulose extinction. Mica microstructures include mica kinks.

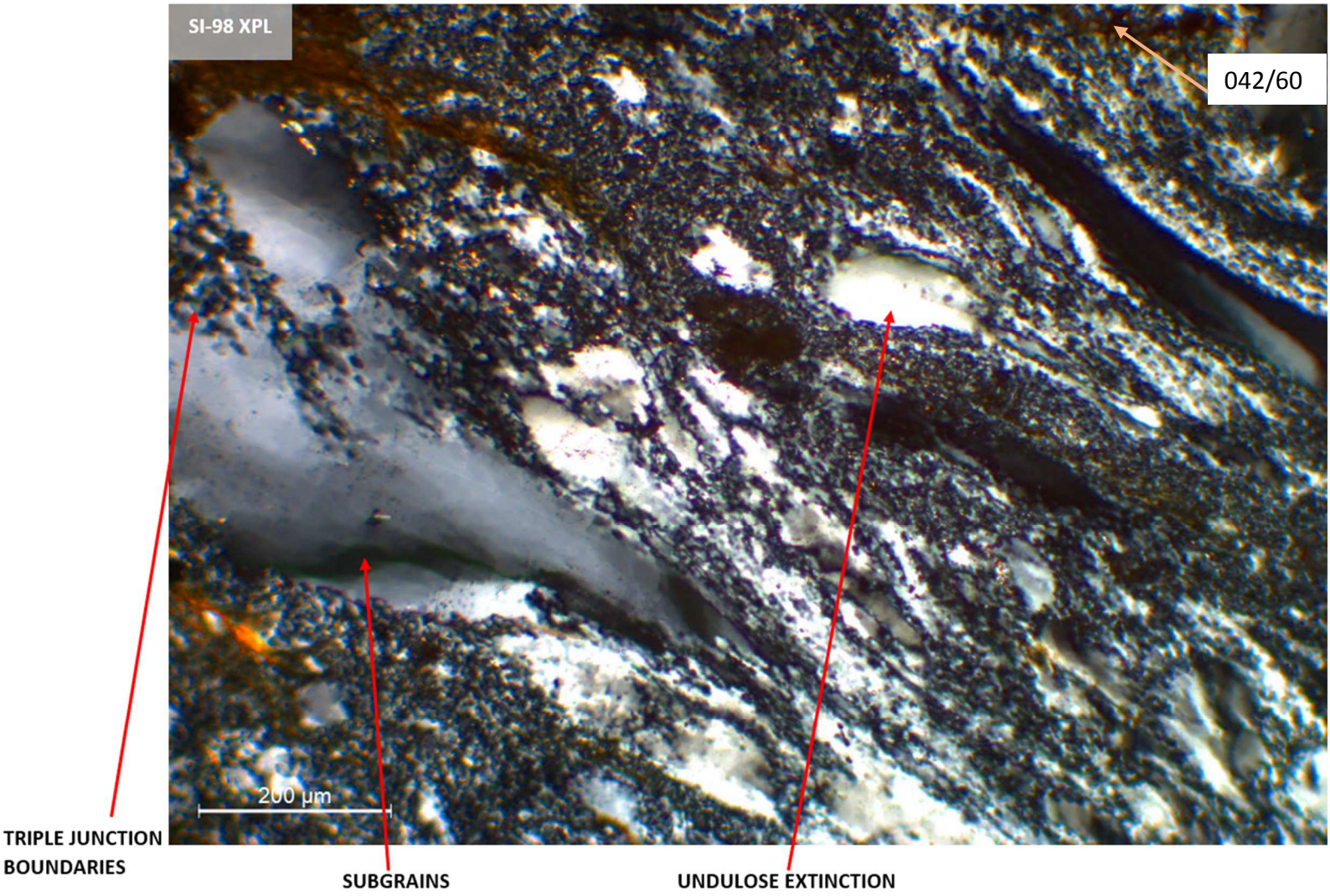

Figure 20: Selected area of SI-98 (Phyllite) thin section, XPL. Distance from the shear zone is 120.7m. The orientation of the long axis is shown in the top right corner (trend/plunge) (orange arrow). Quartz microstructures include subgrains, triple junction boundaries, undulose extinction.

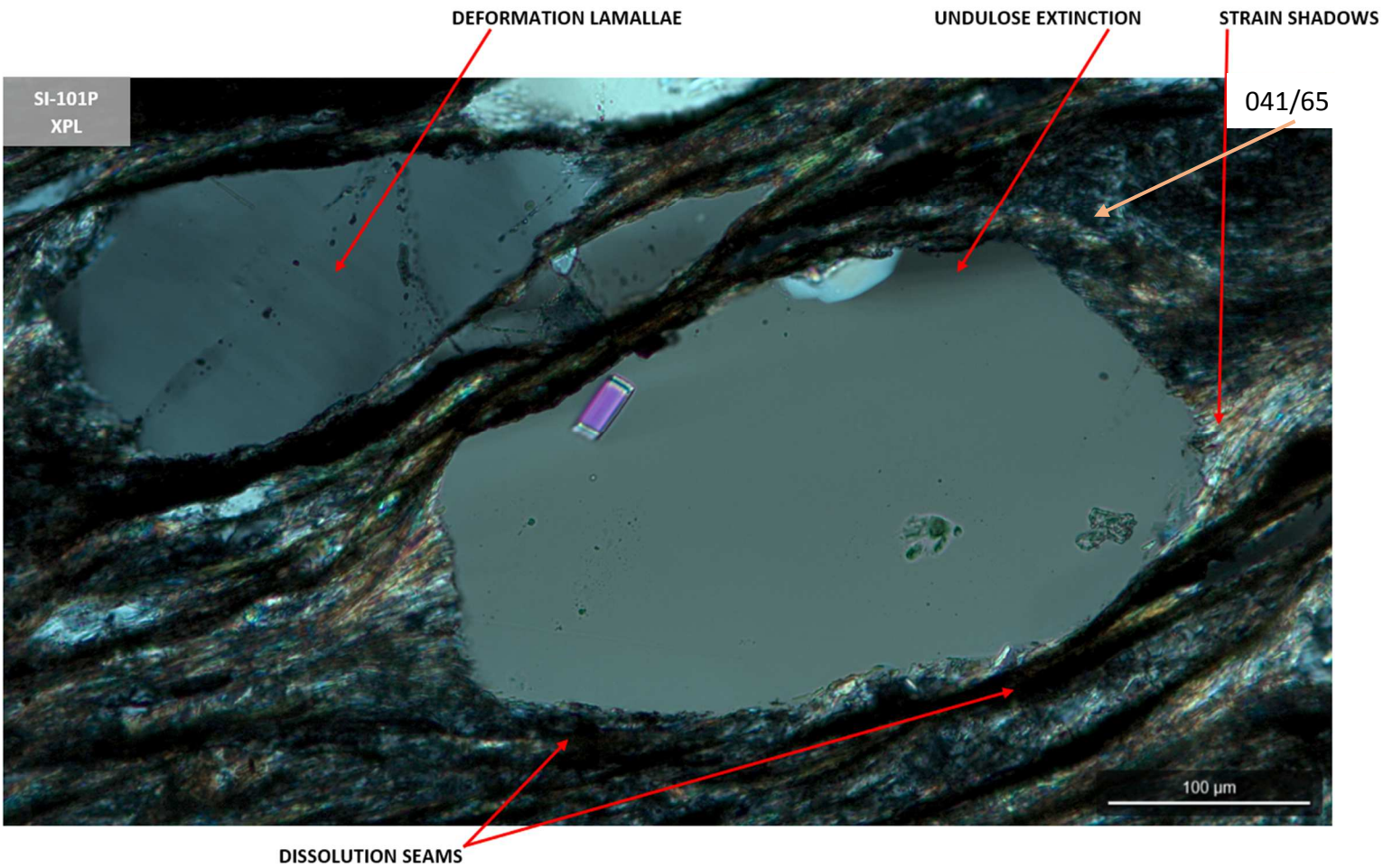

Figure 21: Selected area of SI-101P (Phyllite) thin section, XPL. Distance from the shear zone is 173m. The orientation of the long axis is shown in the top right corner (trend/plunge) (orange arrow). Quartz microstructures include undulose extinction and deformation lamellae. Biotite and muscovite make up the strain shadows. The dissolution seams are cause by insoluble minerals.

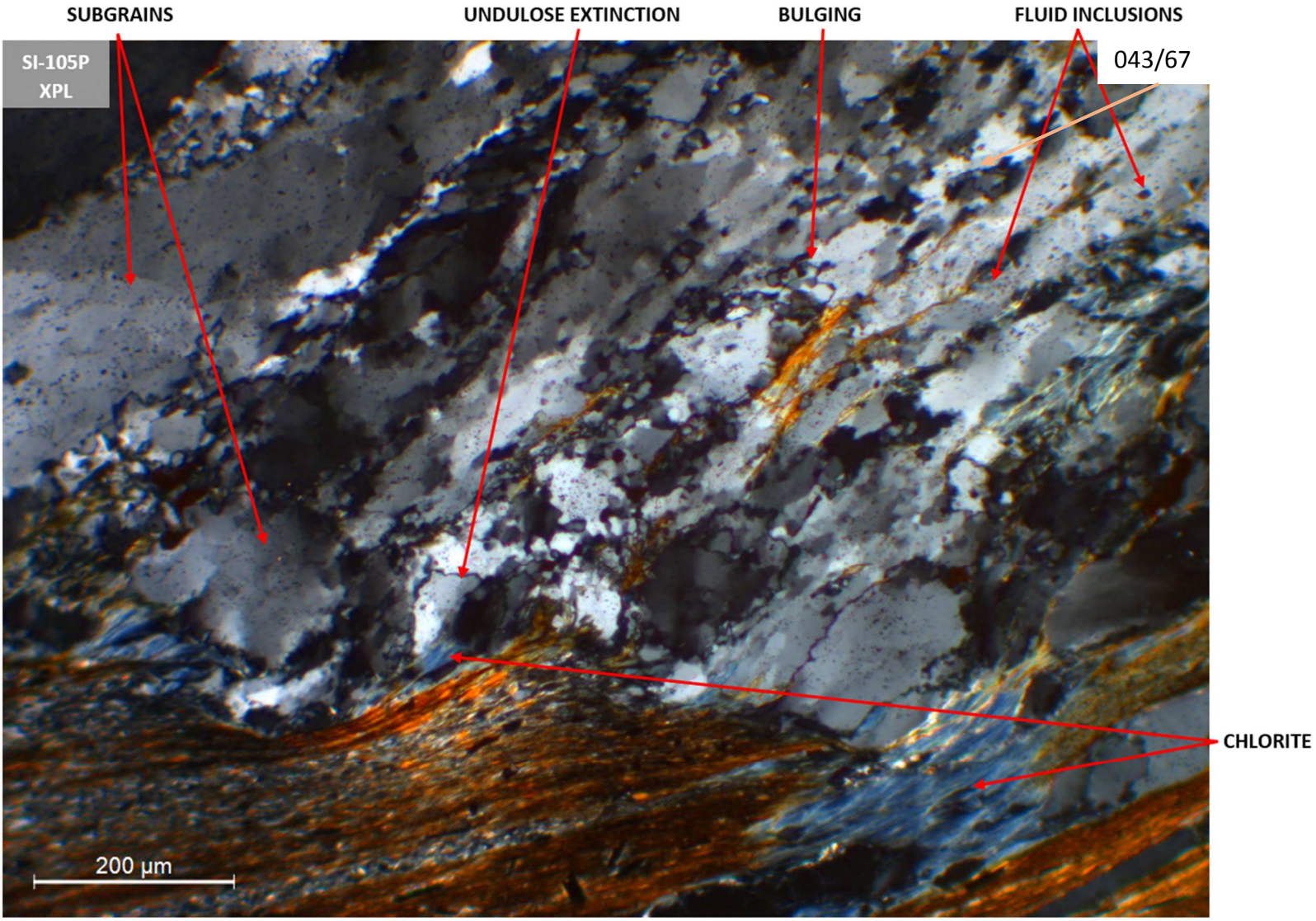

Figure 22: Selected area of SI-105P (Slate) thin section, XPL. Distance from the shear zone is 212m. The orientation of the long axis is shown in the top right corner (trend/plunge) (orange arrow). Quartz microstructures include bulging, subgrains, undulose extinction and fluid inclusions. Mica microstructures include mica kinks.

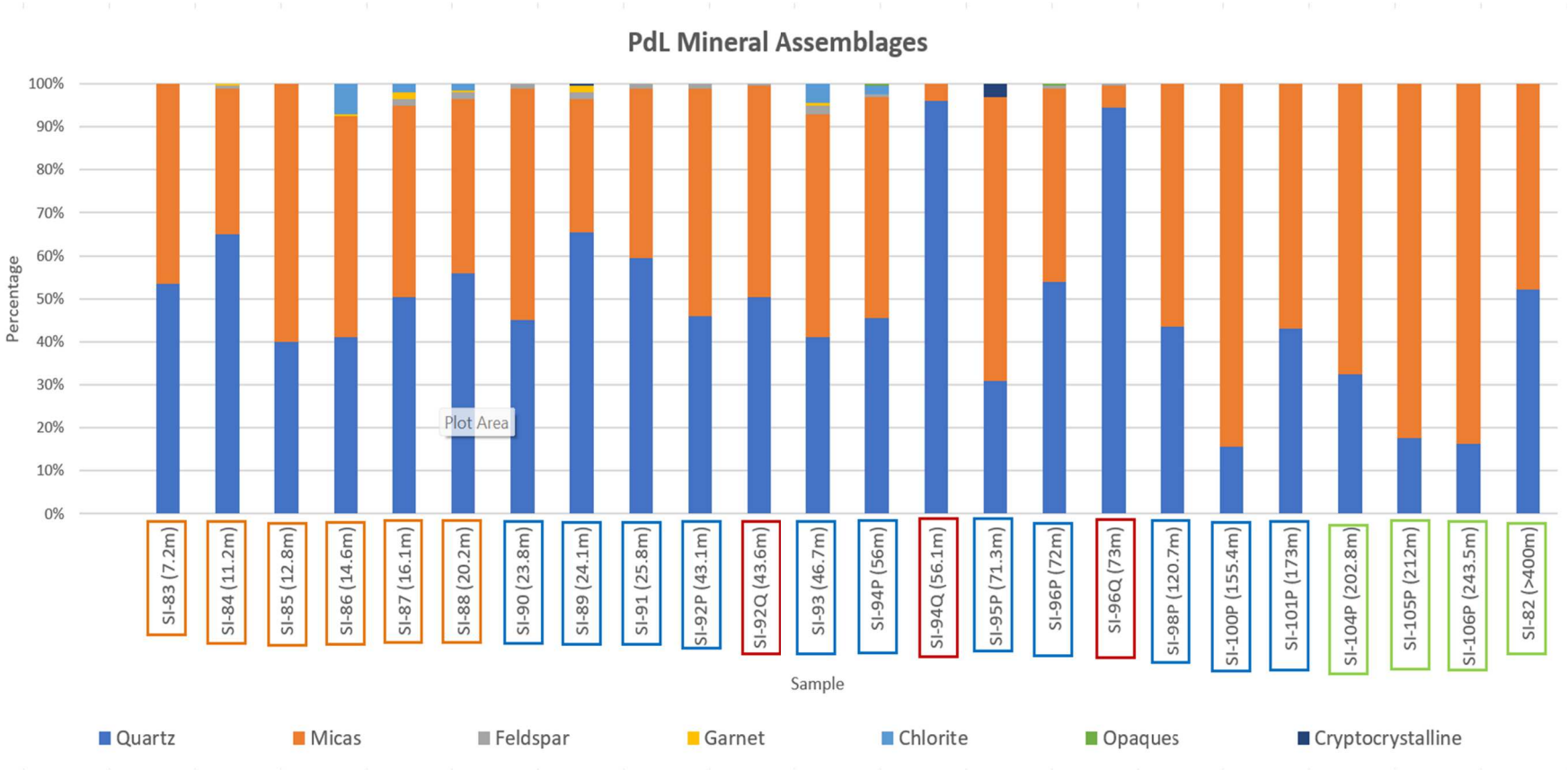

Figure 23: The mineral composition of all 24 samples collected in the PdL. Samples are organized by distance from the shear zone boundary and the distance is provided in the paratheses next to the sample name. Samples outlined in orange are schists, the blue outline is phyllites, red are quartzites, and green are slates. Colors indicate the different minerals shown in the legend below the graph.

4.2 Electron Backscatter Diffraction Analysis

Regions from twenty-four samples were indexed for quartz. The amount of quartz that was indexed out of all point analyzed ranges from 10% to 60% in the schists and phyllites (Fig. 23). In the quartzites, about 80% of quartz was indexed, excluding 92Q. For mica rich samples, the amount of quartz that was present in many of these samples was low, making it difficult to achieve a high phase fraction of quartz (Table 2). The quartzites indexed well and had the highest phase fraction (Table 2). The area of all mapped regions can be found in Table 2. A few samples that had similar areas such as SI-84,86,88. A lot of the schists and phyllites indexed quartz above 40%, but there are a few very low samples like SI-96P. Most samples had about 2000-4000 grains that were from the amount of indexed quartz. The samples with the largest number of grains are the quartzites and some phyllites with a higher quartz composition (Table 2). There is not a common pattern with the number of grains that were used for CPOs, but the samples with the highest number of grains was located at 70 m from the shear zone boundary.

Sample Name	Distance from Shear Zone (m)	Area Mapped (um^2)	Phase Fraction (%)	Total Points Analyzed	Phase Count (Qtz)	Standard Deviation Band Contrast	Step-size (um)	Grains used from indexed points	Rock Type
SI-83	7.2	350x1255	43.63	431430	188246	32.98	1	2929	Schist
SI-84	11.2	386x1308	52.50	431977	226781	26.49	1	3573	Schist
SI-85	12.8	391x1253	46.83	431868	202223	27.72	1	2985	Schist
SI-86	14.6	388x1252	23.47	431977	101392	20.79	1	2380	Schist
SI-87	16.1	393x1247	53.22	432306	230076	25.92	1	2609	Schist
SI-88	20.2	360x1249	29.02	431977	125361	27.60	1	2269	Schist
SI-89	24.1	394x1254	51.69	432306	223473	22.65	1	1824	Phyllite
SI-90	23.8	606x844	60.25	576079	347107	20.11	1	1956	Phyllite
SI-91	25.8	386x1251	32.22	432306	139307	27.18	1	2009	Phyllite
SI-92Q	43.6	430x1662	81.04	575970	466760	25.13	1	1731	Quartzite
SI-92P	43.1	401x1260	49.84	432306	215450	23.66	1	2056	Phyllite
SI-93	46.7	399x1251	60.25	431540	347107	20.11	1	3577	Phyllite
SI-94P	56	401x1257	37.82	431539	163220	21.75	1	2848	Phyllite
SI-94Q	56.1	630x844	79.24	575641	456123	18.62	1	3845	Quartzite
SI-95P	71.3	356x1258	35.67	432306	154188	21.46	1	9344	Phyllite
SI-96P	72	391x1294	11.93	431102	51417	22.12	1	3252	Phyllite
SI-96Q	73	1521x1620	57.76	721824	416927	17.60	2	14752	Quartzite
SI-98	120.7	391x1255	27.22	431868	117535	23.06	1	5230	Phyllite
SI-100P	155.4	391x1299	20.18	431539	87068	22.25	1	4638	Phyllite
SI-101P	173	399x1301	37.58	431977	162324	26.71	1	7019	Phyllite
SI-104P	202.8	387x1253	33.92	431540	146377	26.80	1	6975	Slate

SI-105P	212	439x1669	12.47	575970	71812	23.92	1	3388	Slate
SI-106P	243.5	394x1259	52.72	431868	227685	24.23	1	9982	Slate
SI-82	>400	362x846	13.08	287766	37643	18.49	1	2591	Slate

Table 1: EBSD data for each sample and the distance from the shear zone boundary.

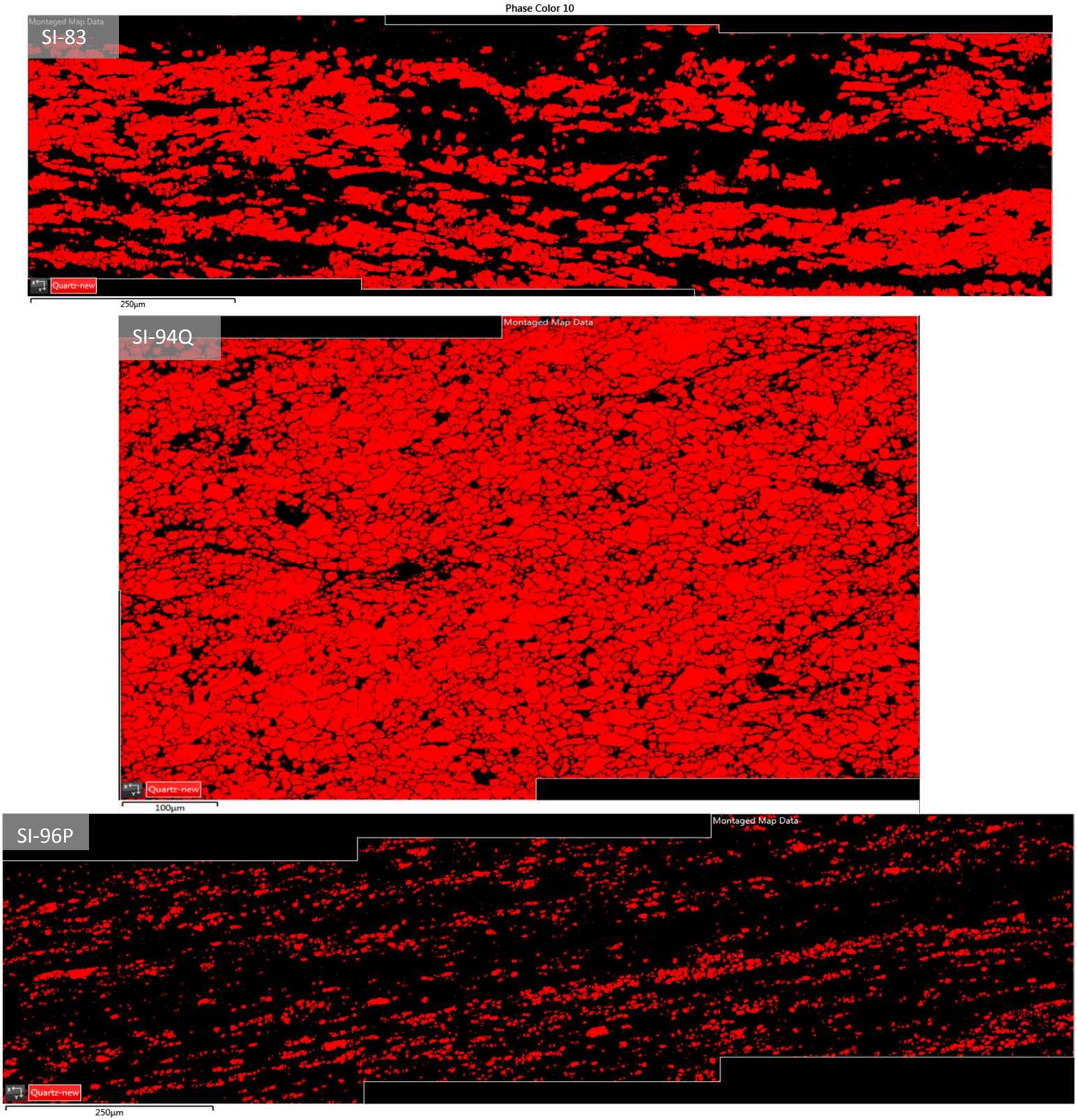

Figure 24: Three different EBSD phase maps. The red represents the index quartz. The top map shows a schist/phyllite sample with a higher quartz composition. The middle map is the result of mapping quartzites. The bottom map are schist/phyllites with a lower quartz composition.

4.2.1 Vorticity Analysis

4.2.1.1 CPO Results

Quartz c-axis and a-axis CPO plots were created from the EBSD data (Fig. 23 and 26). The overall patterns from this transect varied throughout. There are several plots at varying distances where there is not a clear pattern that has developed meaning there is not a preferred orientation. Samples SI-84, SI-88, SI-95P, SI-100P, SI-101P, SI-104P, SI-82 have an EW single girdle for the c-axis. Samples SI-85, SI-86, SI-87, SI-92P, SI-93, SI-94Q, SI-96P, SI-105P, SI-106P have a one or two point maximum within the c-axis. There are not many consistencies in the overall patterns, but the EW single girdle further than 173 m from the shear zone boundary have a more evident pattern than other EW single girdle closer to the boundary. The other samples don't present a clear pattern of a preferred orientation (Fig. 26). To aid in the interpretation of these patterns, the a-axis is also included, which allows for more complete interpretation of kinematics (Parsons et al., 2016; Renjith and Mamtani, 2014; Barth et al., 2010; Chen et al., 2022).

4.2.1.2 CVA Results

The CVA pole figures vary across the transect. There are three types of patterns that are seen in these rocks that can help to determine the kinematics of this shear zone (Michels et al., 2015). Samples SI-83, SI-85, SI-87, SI-89, SI-92A, SI-94P, SI-95, SI-96Q, SI-101P, SI-104P, SI-105P, SI-106P have the CVA 'bullseye' in the middle, meaning that the vorticity vector is assumed perpendicular to the lineation (Fig. 26). Samples SI-89 and SI-93 have a vorticity vector that is assumed to be parallel to the lineation, the vorticity vector for SI-89 may be oblique to the assumed lineation. In these, the CVA "bullseye" plots around the 090° and 270° points on the

outside of the pole figures. Eight samples, SI-84, 86, 88, 91, 92P, 94Q, 98P, 100P contain a vorticity vector that is assumed oblique to the lineation. The samples that had the vorticity vector oblique or parallel to the lineation, were rotated to try and achieve 'bullseye' in the middle of the CVA plot. This rotation was also applied to the CPO of the a-axis and the c-axis because the rotation moves the bullseye to the middle of the plot to assume the thin section was cut along to VNS (Fig. 25). For some samples that had to be rotated, the vorticity vector plotted in the middle of the pole figure, the others however are still a bit oblique. The vorticity vector is likely as close as it can be without extreme rotation of the data.

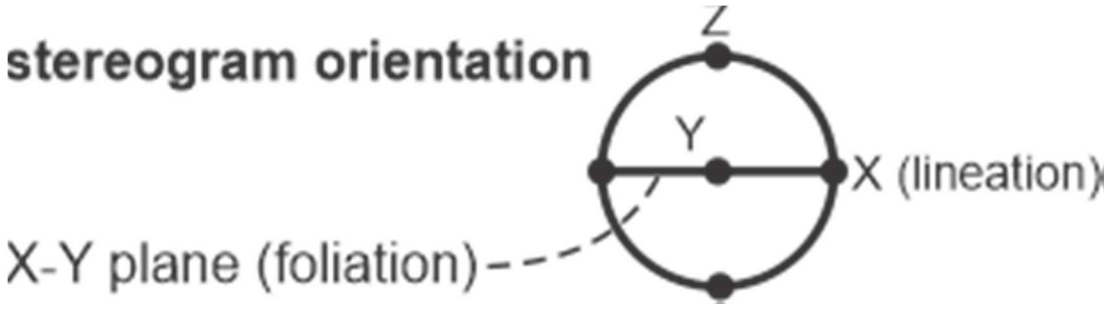

Figure 25: Orientation of all stereograms.

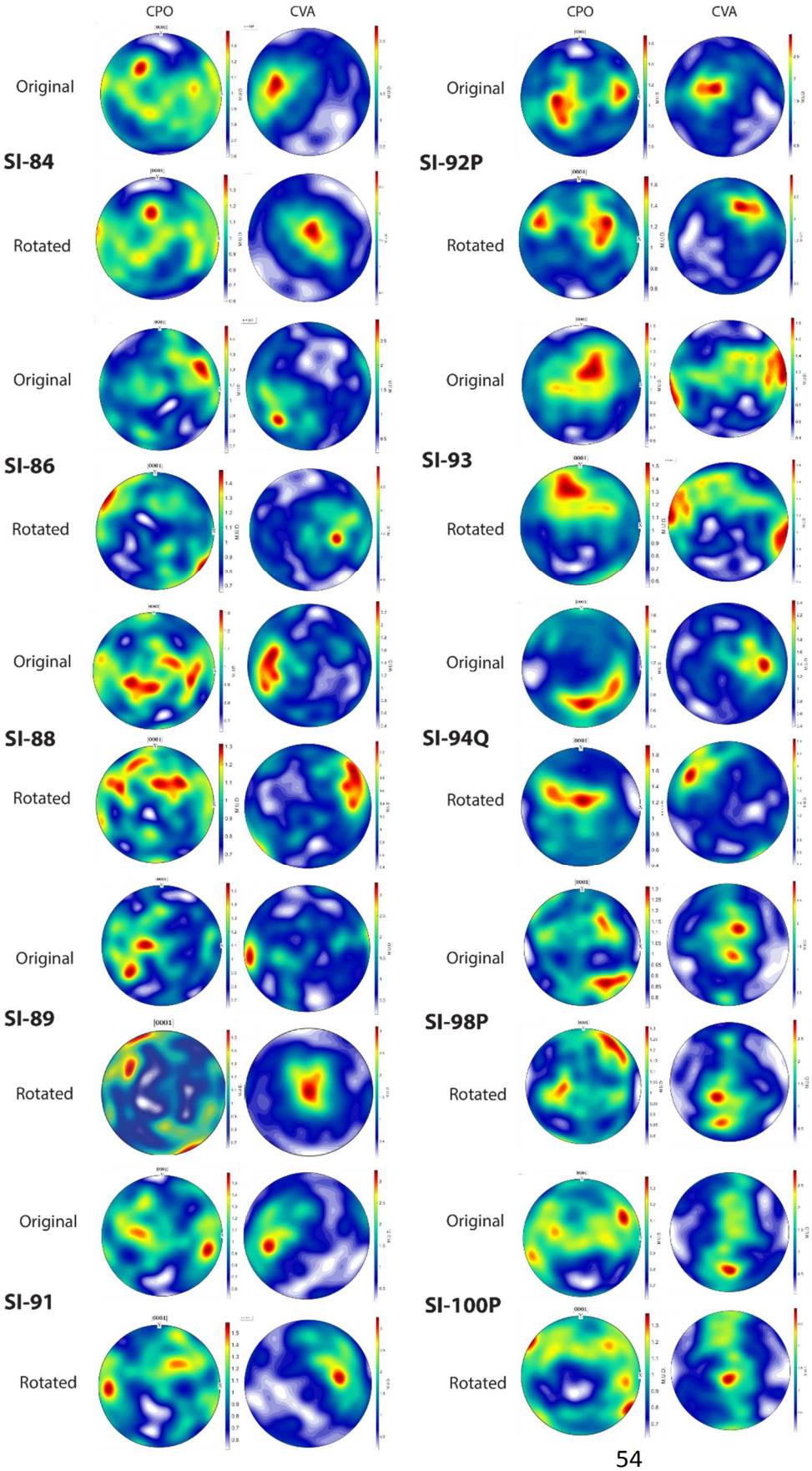

Figure 26: Ten original plots of quartz c-axis and CVA versus the rotated plots. Sample number is provided between the original and rotated plots to the left of the CPO plots. The top two figures are the original CPO and CVA plots. The bottom two are the rotated CPO and CVA plots. The color bar is the MUD for each sample.

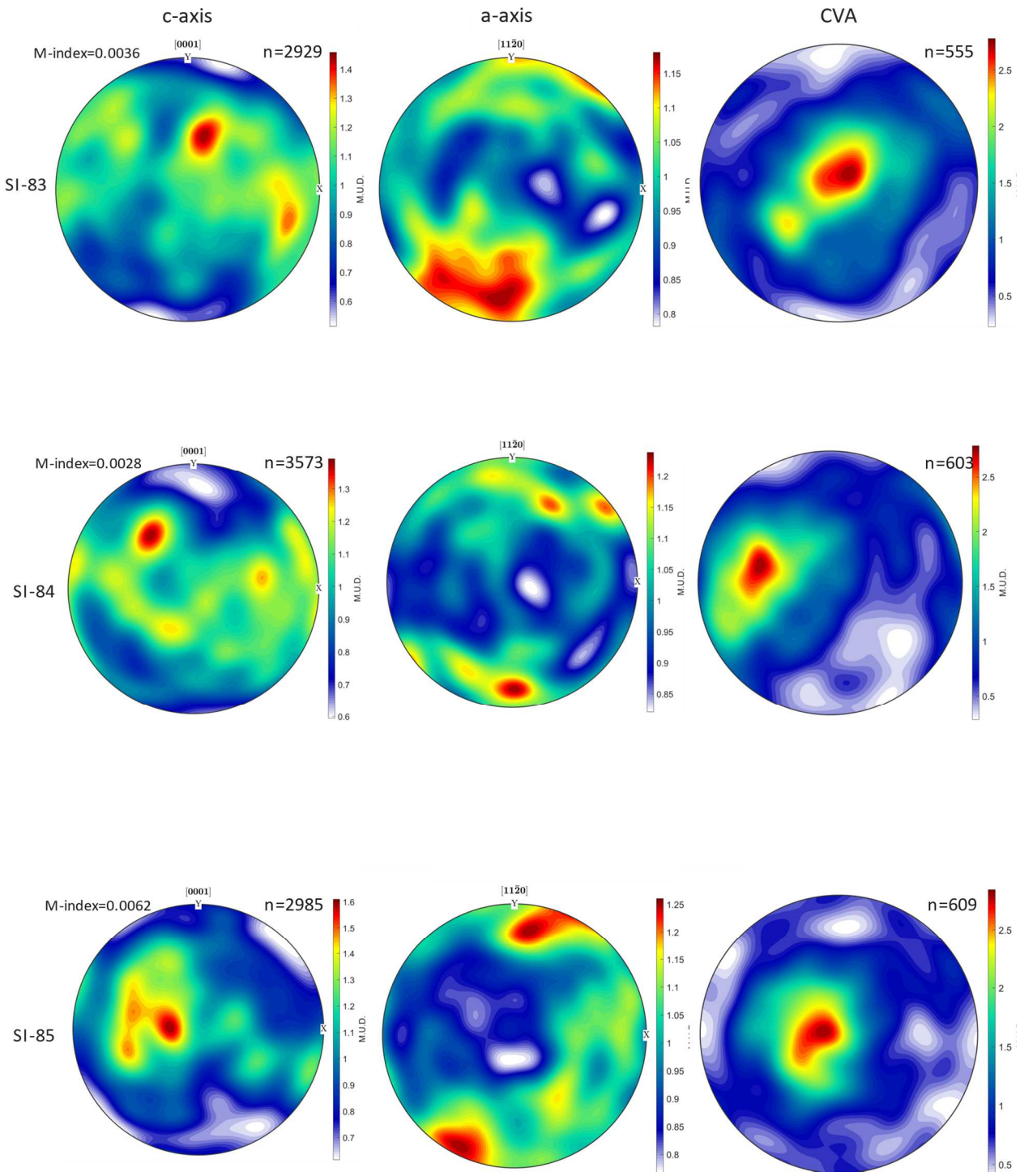

Figure 27: CPOs of quartz c-axis and a-axis with the CVA for each sample (c-axis on the left, a-axis in the middle, and CVA on the right). Sample name is provided to the left in the center of the figure. M-index is shown in the top left of the c-axis plot. N= the number of grains per sample. The color bar represents the MUD for each sample. The X and Y directions are where MATLAB places them but not the actual specimen reference frame. X is on the right; z is on top of the plot; and y is in the middle of the plot (see figure 24 for reference).

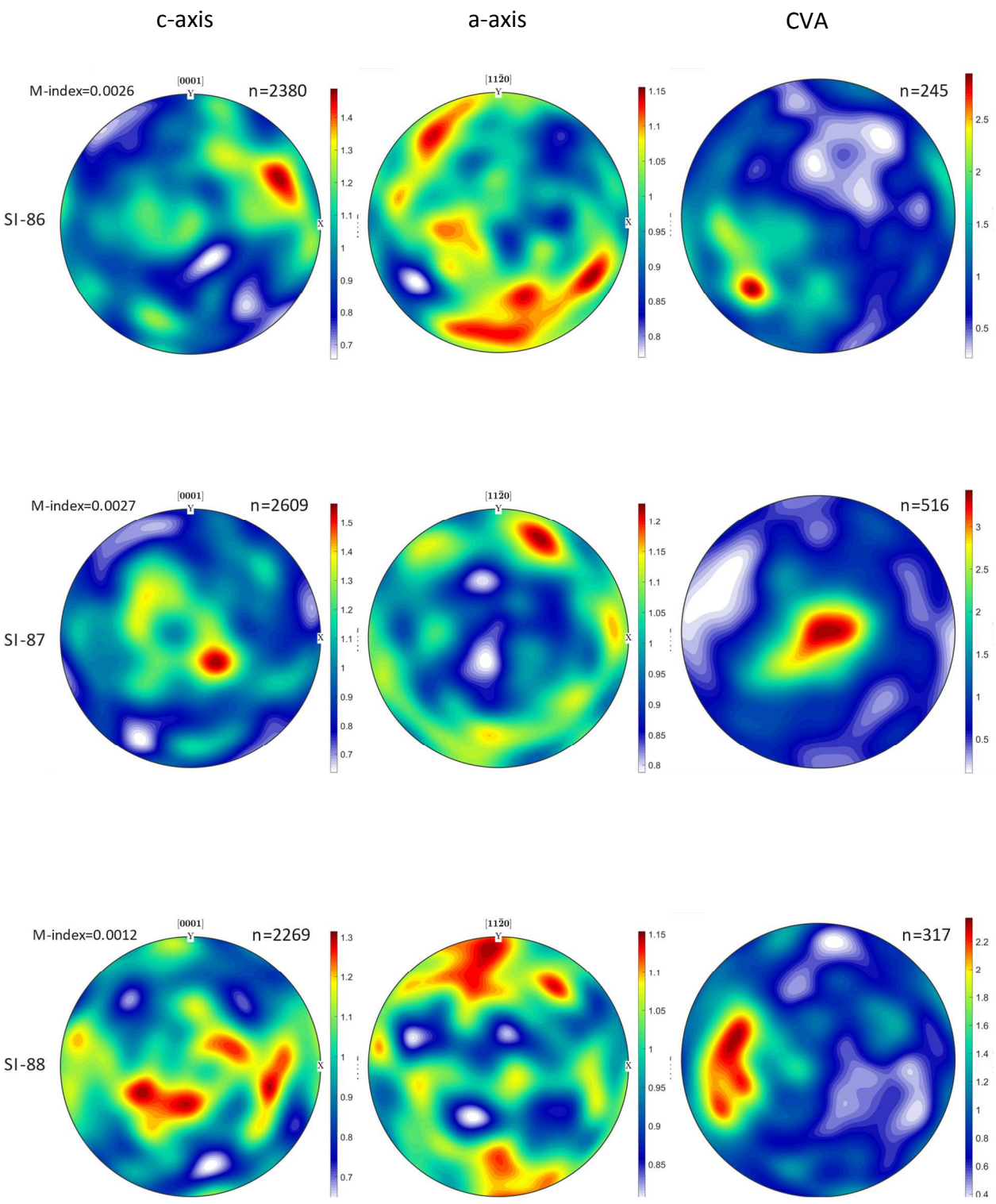

Figure 27 continued

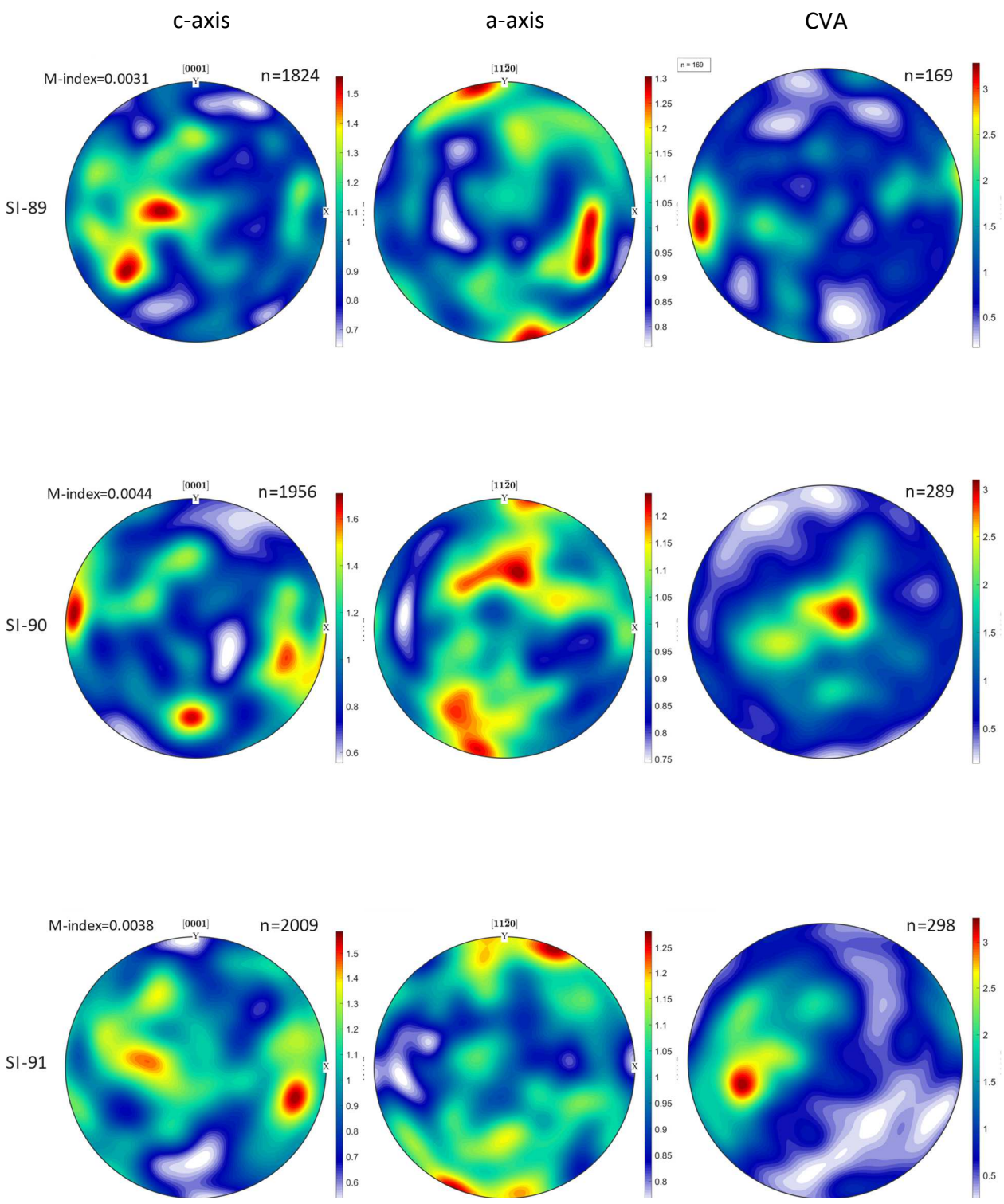

Figure 27 continued

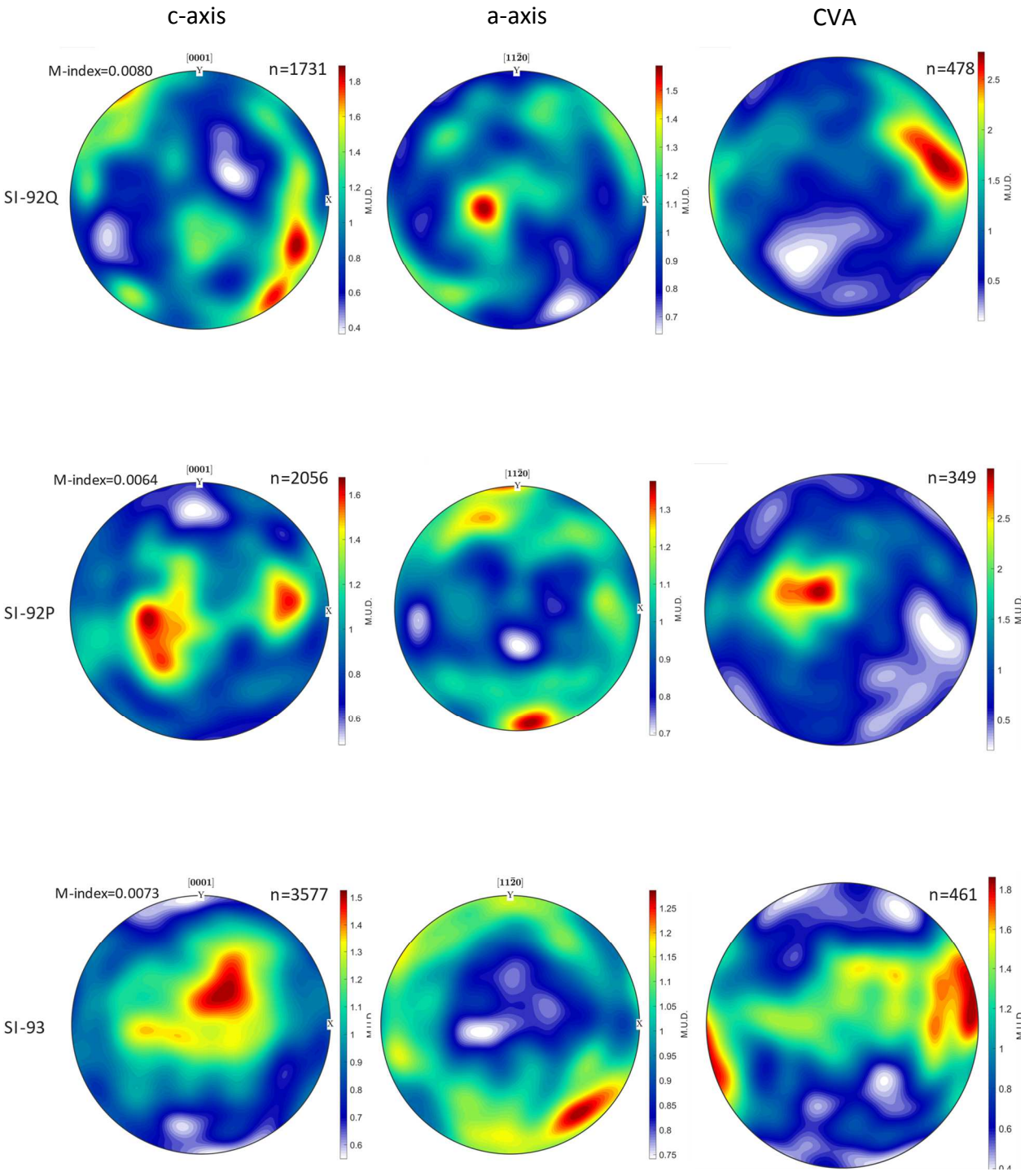

Figure 27 continued

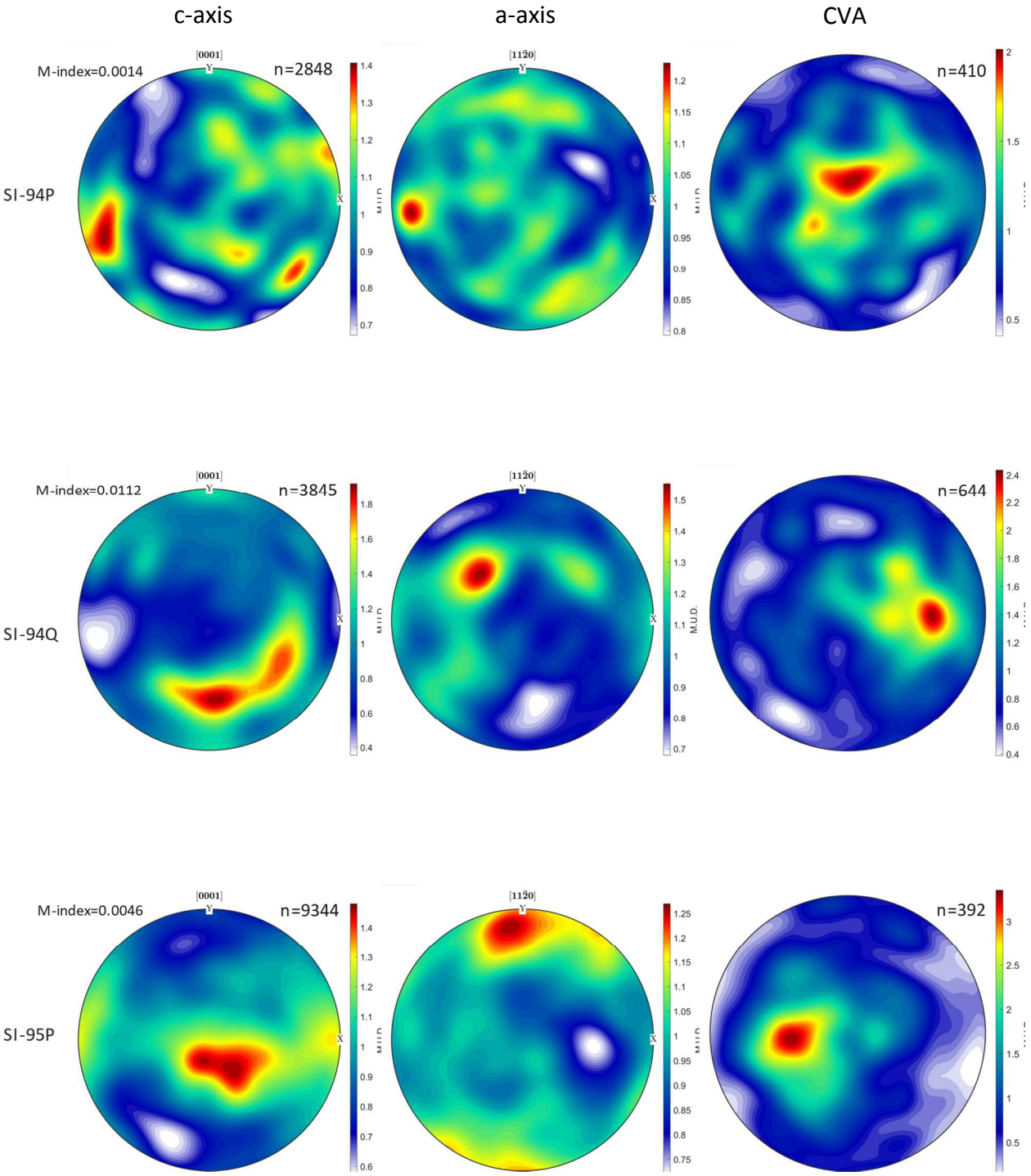

Figure 27 continued

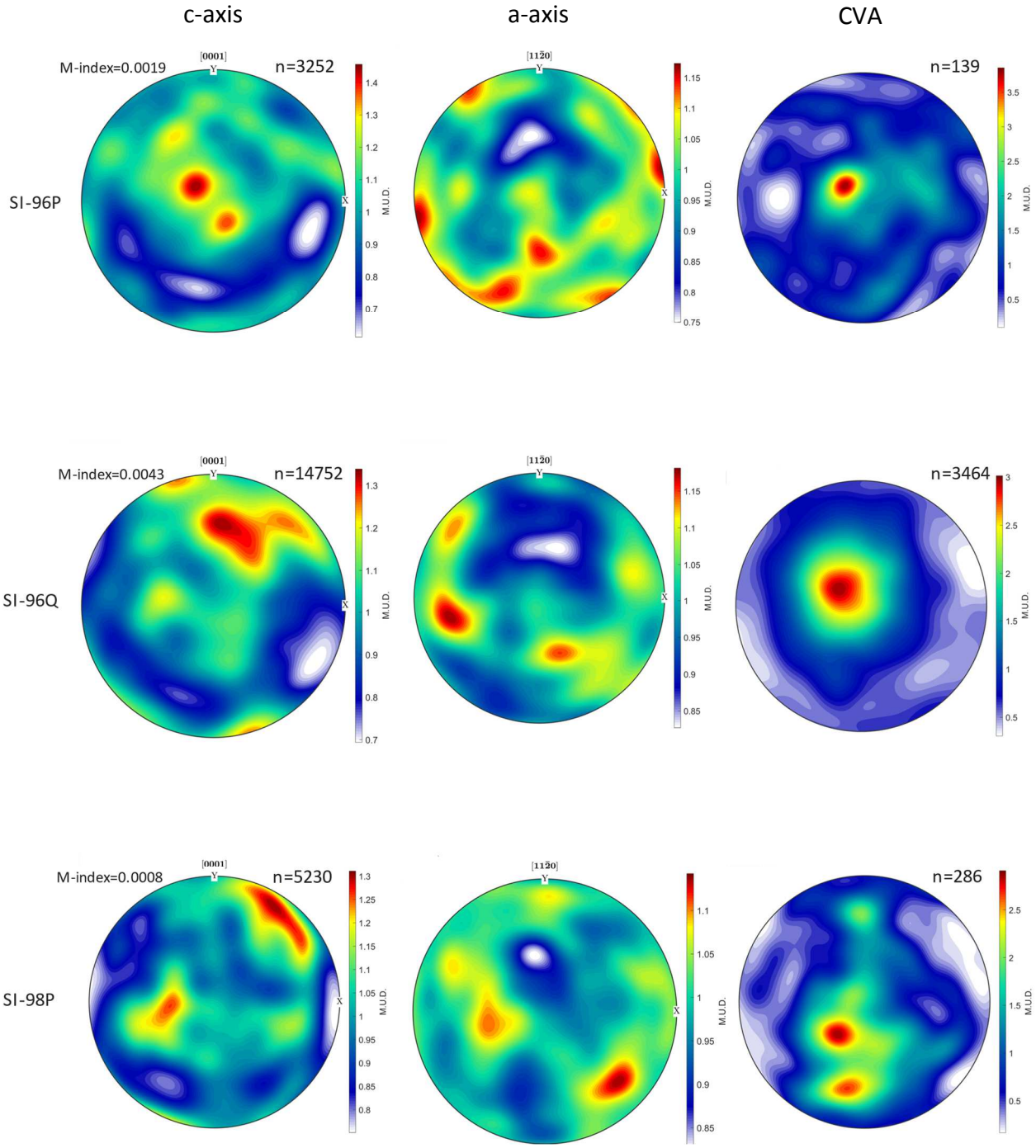

Figure 27 continued

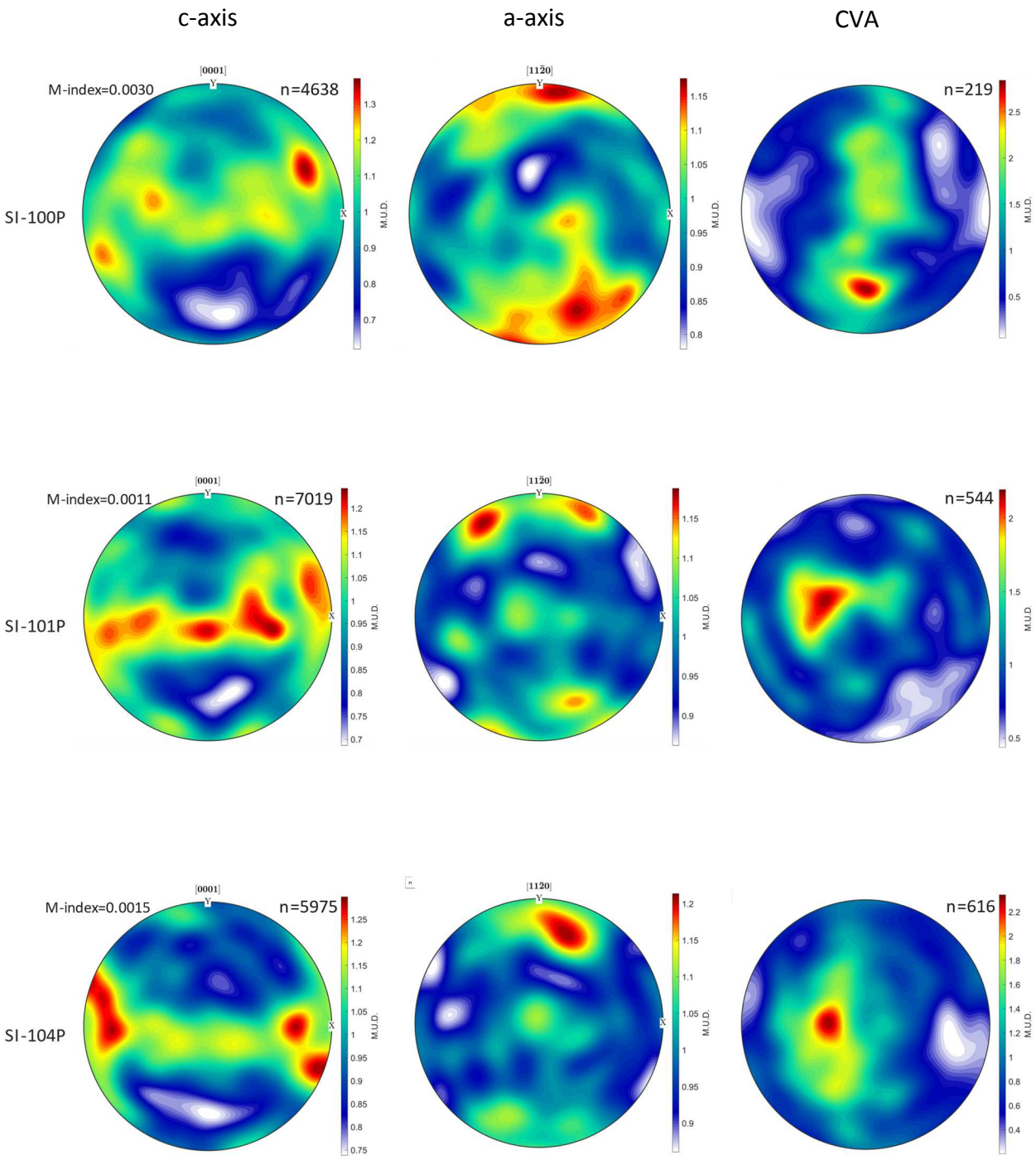

Figure 27 continued

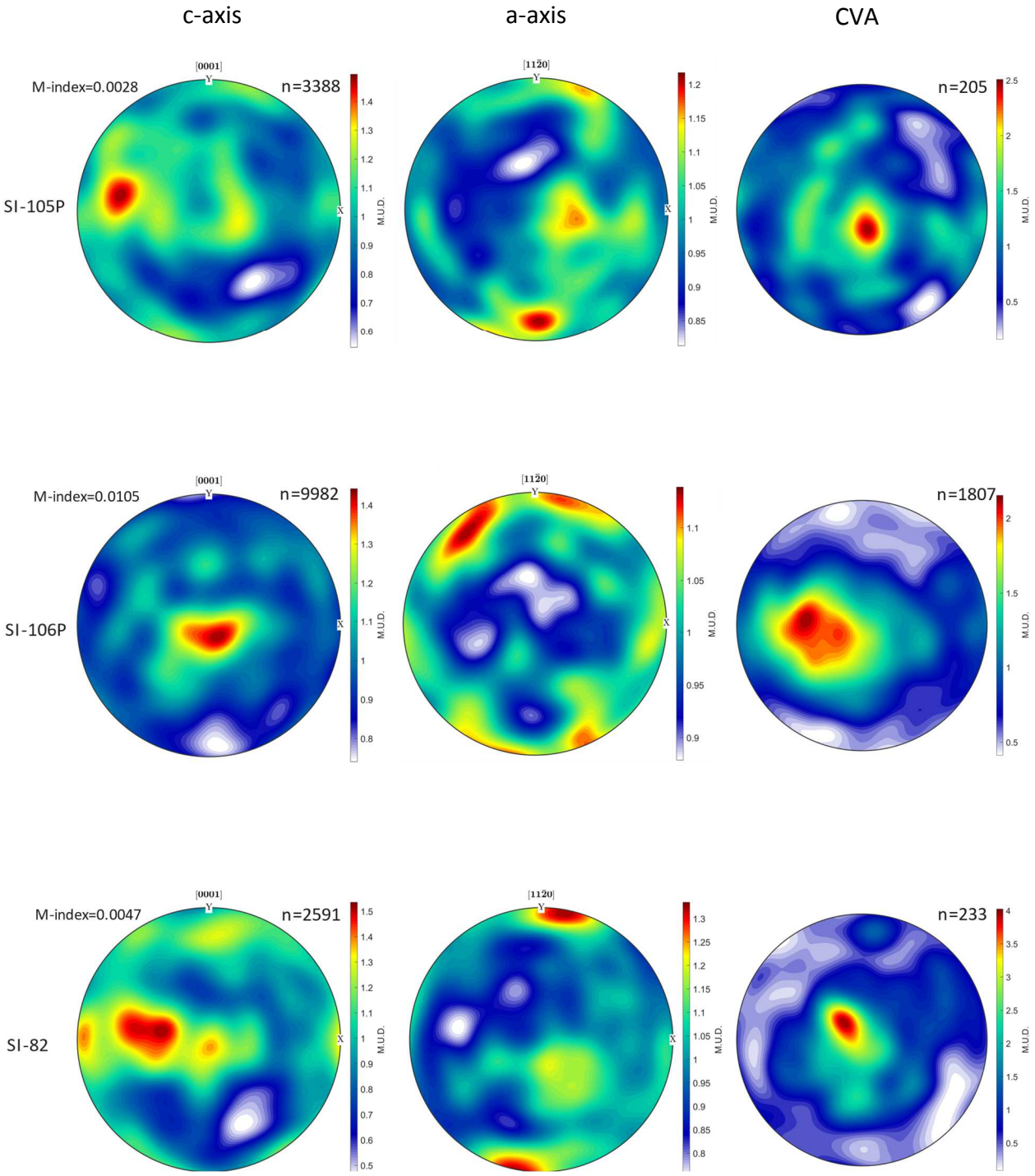

Figure 27 continued

CHAPTER 5: Discussion

5.1 Microstructures and deformation mechanisms

Regardless of mineral assemblage or distance from the shear zone, all samples have multiple types of microstructures related to brittle deformation, diffusive mass transfer (DMT), and dislocation creep. Carman (2020) found that brittle microstructures are most abundant closest to the shear zone (<10 m) and that DMT features are most abundant within approximately 50 m of the shear zone. She hypothesized that the increased evidence for brittle mechanisms (especially fracturing and fluid inclusion planes) and DMT close to the SISZ is related to syn-deformational fluid flow along the shear zone. The metamorphic phases documented here within approximately 50 m of the SISZ boundary are consistent with syndeformational fluid interaction. In particular, the presence of chlorite suggests water rich metamorphism and the relatively high temperature phase of garnet is consistent with contact metamorphism as the SISZ brought the hotter metabasites up against the colder PdL. Also consistent with the findings of Carman (2020), the abundance of dislocation creep microstructures in quartz gradually increases towards the shear zone which suggests that either there was higher strain and/or that relatively more of deformation was accommodated by dislocation creep near the shear zone. These hypotheses can be further evaluated with the EBSD data.

The type and strength of the quartz CPO pattern can be used to determine whether dislocation creep accommodated more strain toward the shear zone. The dislocation creep microstructures present in quartz indicated that there should be fairly strong CPO patterns. Quartz also has a slight shape preferred orientation to help form a foliation in quartz rich samples. However, a lot of diffusional microstructures and foliations are present, so it is difficult to predict the strength of the CPO patterns from microstructures alone.

5.2 Quartz CPO patterns and relative contribution of deformation mechanisms

The quartz CPO patterns helped to determine if diffusional or dislocation processes dominated in the quartz deformation. All samples had a quartz CPO, which confirms the interpretation from the microstructural observations that quartz deformed partially by dislocation creep in all samples regardless of lithology or distance from the SISZ. However, the strength of the CPO was weak (with M-index values ranging between 0.001 - 0.008) suggesting that DMT was the dominant mechanism over dislocation in quartz in all locations and lithologies. Other studies have higher M-indices; 0.10-0.6 (Rahl and Skemer, 2016); 0.01 - 0.34 (Cross et al., 2017); 0.01 - 0.34 (Starnes et al., 2020); 0.004 - 0.3 with 0.004 considered to be a week pattern and 0.3 being a stronger pattern (Stenvall et al., 2019); 0.03 - 0.28 (Kruckenberg et al., 2019). Generally, M-indices below 0.01 are considered weak. However, in each of these studies the factors are variable, such as mineralogy, grain size and temperature being the biggest factors. Mineralogy plays a large role on the strength of the patterns.

With M-index being a fairly new concept, there are few papers that use this value. Most studies that do include a M-index analyze metaigneous rocks, and few consider metasedimentary rocks. The composition between the metaigneous rocks in these studies compared to the metasedimentary rocks in this study is drastically different. Samples that contain about 40% of feldspar and quartz are consistent with higher m-indices (Kruckenberg et al., 2019; Stenvall et al., 2019). Starnes et al., (2020) explored samples that range from 0 to 20% mica that underwent deformation temperatures above 500° C and reaching to 700° C. The samples with the higher mica content and higher deformation temperature have a higher M-index. These factors influence rocks under deformation differently and it can be hard to interpret how mineralogy, grain size,

and temperature worked together to form CPO patterns. With the variation in the strength of the CPO pattern across the transect, there may be some areas that have dislocation as the dominant mechanism and diffusion plays a smaller role in deformation (Fig. 26)

5.2.1 Factors controlling CPO strength and relationship to strain magnitude

To determine if the relative contribution of dislocation creep to the overall deformation is controlled by factors such as composition, distance from shear zone (assumed to be a proxy for strain in this case), and grain size, the M-index was plotted against each factor. Generally, we would expect that the strength of the M-index would increase if more deformation was accommodated by dislocation creep.

One of the main objectives of this project was to determine the role lithology plays in controlling deformation mechanism at the micrometer scale. Previous studies have found that in quartz and mica rich metasedimentary rocks, dislocation creep is more dominant in samples with higher quartz concentrations and DMT is more dominant in samples with higher mica concentrations (Little et al., 2015; Wenk et al., 2019; Schmidt and Platt, 2021). Therefore, when comparing the M-index and the quartz content, we would expect that there would be a positive correlation between higher quartz content and higher m-index. To test this hypothesis, 24 samples were point counted to determine the quartz concentration in each sample. The number of quartz was counted and then divided by the total points counted, which was 200 points. The M-index that was calculated for each sample was paired with the percent of quartz to determine if the CPO strength is correlated with quartz composition. The resulting plot indicates that despite our predictions, quartz concentration and strength of CPO pattern do not have a clear relationship (Fig. 28).

From these results, there is an indication that lithology did not play a big role in strain partitioning of the SISZ at the micrometer scale, but it is known to affect strain localization at much larger scales (Carman, 2020). The discrepancy may be related to the effects of scale, but also possibly due to a lack of indexed quartz grains in this study. Figure 30 shows a correlation between the M-index and the amount of quartz that was indexed in each sample. The samples did not have a very large area that was indexed to increase confidence in data of a smaller area. It is possible that too few quartz grains were indexed to determine the effects lithology has on strain partitioning. The higher the phase fraction (# of quartz grains indexed) the higher the strength of the pattern of the CPOs (Fig. 29). Indexing more quartz may result in different.

Figure 29 shows how the phase fraction of quartz within the EBSD maps and the M-index are correlated. Before making this graph, predictions were made that the higher the phase fraction, the higher the M-index value. More quartz grains mean there are a lower number of micas, so when these rocks are deformed, the mica orientation will not interfere with quartz growth. In addition, it seemed likely that if more quartz grains were used to determine the M-index, a stronger value would result.

The PdL transect studied here has a known strain gradient (Carman, 2020). The PdL generally has higher strain closest to the shear zone boundary and it decreases as the distance from the SISZ boundary increases. Closest to the boundary, the samples were expected to have a lot of dislocation processes occurring because the close distance corresponds to higher strain. However, the strength of the patterns has no obvious correlation to the distance from the shear zone (Fig. 30). Many samples close to the boundary had low M-indices (Fig. 30). In addition, the M-index was calculated for different grain size bins to determine if there is a pattern between

grain size and strength of the CPOs. It is hard to interpret the results from this set of data. Of the three bins used, only the smallest two bins had an abundant number of grains. The larger the grain, the stronger the pattern, but this is likely skewed because of the limited number of grains that were indexed. With current data, it appears that smaller grain size allows more diffusional processes than the larger grains (Fig. 31).

When thinking of factors that controlled strain partitioning, increased distance from the shear zone was thought to likely correspond with a lower M-index moving away from the shear zone boundary. Based on figure 30, this is no obvious correlation between the distance from the boundary and the m-indices. A correlation was expected because distance is thought to be inversely related to strain. Figure 31 shows a slight correlation between grain size and distance from the shear zone. Smaller grains ~ 10 um tend to have a smaller M-index throughout the distance from the shear zone although, ~3 um and above show a slight increase in the M-index with increasing distance from the shear zone boundary. The more noticeable comparison is between the ~10 um-30um M-index and distance. With increasing distance from the shear zone boundary, the M-indices increase in value. However, this may be biased because there are not as many ~10-30 um grains as there are >10 um grains.

While correlations between these individual parameters and fabric strength are not clear, plotting the M-index, distance, and phase fraction together provides a more complete picture. The two highest M-indices plot at the intersection between these points. Samples that contain a higher phase fraction with a short distance to the shear zone boundary have a higher m-index value (Fig 30). While these factors may not individually explain CPO strength, when viewed all together, there is a clear connection between these three factors.

5.3 Quartz CPO patterns, CVA analysis, and kinematic interpretation

The orientation of the quartz CPO pattern varied throughout the entire transect. Although the CPO patterns were weak where present, they can be used to interpret kinematic framework. The patterns that did emerge were atypical of most shear zone studies (Fig. 26) (Law et al., 1986; Thigpen et al., 2010; Little et al., 2015; Faleiros et al., 2016; Rahl and Skemer, 2016; Kruckenberg et al., 2019; Starnes et al., 2019; Stenvall et al., 2019), which are generally dominated by simple shear or, to a lesser extent, pure shear deformation. In contrast, the CPO patterns in the PdL that contained a crossed girdle or a cleft girdle are unusual, and most likely indicate an overall flattening deformation and/or a combination of both constriction and flattening (Fig 10). SI-100P is a one of very few patterns that has a cleft or a crossed girdle, and it plots on the plain strain line. (Fig 10).

The CPO girdles are also used to determine coaxial versus noncoaxial deformation. For the samples that contain a girdle, the girdles look symmetrical. This implies that these samples underwent coaxial deformation, however other evidence such as the shear sense indicators and the vorticity analysis from Carman (2020) don't correlated with these findings and is likely not a useful for interpretations.

The PdL may have unusual CPO patterns due to its kinematics. The SISZ is interpreted to have undergone transpression, which implies that it results in an overall flattening shape. This is consistent with the quartz c-axis and a-axis CPO observations. In comparison, many other studies look at discrete thrust faults such as the Moine Thrust zone, and strike slip faults such as the Alpine fault in New Zealand (Norris and Cooper, 1995; Law and Johnson, 2010).

The CVA patterns are like the CPO patterns in the sense that they vary throughout the transect. The CVA patterns can be used to interpret the type of deformation that likely occurred

in different areas of the PdL. The CVA patterns revealed three different types of kinematic frameworks when compared with the assumed lineation (Michels et al., 2015). In one or two locations (SI-89 and SI-93), the vorticity axis was subparallel to the lineation which is consistent with pure shear dominated transpression (Giorgis et al., 2016). In eight locations (SI-84, SI-86, SI-88, SI-91, SI-92P, SI-94Q, SI-98P, SI-100P), the vorticity vector was oblique to the lineation which is consistent with a triclinic transpression (Michels et al., 2015). Lastly, in most of the locations (SI-82, SI-83, SI-85, SI-87, SI-89, SI-92Q, SI-94P, SI-95P, SI-96P, SI-96Q, SI-101P, SI-104P, SI-105P, SI-106P), the vorticity vector is subperpendicular to the lineation (Fig. 27). This implies these samples underwent wrench (simple shear) dominated transpression (Michels et al., 2015). Through studies on the metabasites to the northern side of the shear zone, lineation data helped determine the best fit kinematic models. Through varying orientations across the metabasite series of the SISZ, the lineations were only explained by a triclinic transpression model with a dominant left- lateral component. The data uncovered by the CVA analysis is consistent with a triclinic model with a large component of left lateral simple shear. The most common patterns that exist throughout the PdL transect are related to triclinic transpression and simple shear dominated transpression. There are shear since indicators in these rocks that help to infer the shear sense, which the CVA analysis cannot. The quartz c-axis CPOs indicate some left lateral shear in combination with a flattening component.

5.4 Slip-systems and deformation temperature

Previous studies reported that deformation of the Acebuches metabasite reached amphibolite facies and the PdL underwent lower greenschist facies (Crespo-Blanc and Orozco, 1988). These metapelites contain chlorite and garnet porphyroblasts which form around at upper

greenschist facies. There is a large metamorphic gradient likely caused by multiple factors. Evidence from EBSD may reveal a slightly different story about the deformation temperature of the PdL unit. Samples SI-85, SI-87, SI-93, SI-95P, SI-96P, and SI-106P contain a single or multiple point maxima that are generated from higher temperatures above 450°. The plots with prism <a> slip (point maxima), indicate temperatures of ~500° C, potentially making deformation temperature within the Pulo do Lobo slightly higher than previously thought, especially in the slates furthest from the SISZ. There are a lot of variations in metamorphic grade throughout the PdL. Close to the shear zone (~60 m) a higher greenschist facies temperature makes sense because the Acebuches metabasites to the north underwent amphibolite facies and the mineral assemblages of chlorite and garnet correspond with higher temperatures. The formation of chlorite and garnet close to the shear zone may be caused by contact metamorphism. The problems lie farther from the SISZ where low grade metamorphism is not likely compatible with temperatures around 500°C indicated by dominant prism <a> slip. Moving away from the shear zone boundary, metamorphic grade decreases based on mineral assemblages and overall rock composition. Chlorite is not present in rocks that are >45 m from the shear zone and garnets cease to form around ~70 m from the shear zone boundary. If the temperature was lower, then it would be likely for basal <a> slip to dominate, however prism <a> dominates throughout the whole transect from 7.2 m->400 m from the shear zone boundary. There is not any indication of prism <c> slip meaning the temperature hovered around 500 °C or below for deformation (Fig. 11). The girdles that appeared in this transect are consistent with lower temperature deformation (Fossen, 2016). With this information, it hard to accurately determine the deformation temperature without more data.

The PdL transect has multiple slip systems that were active during deformation. In some areas there is one slip system that is active, some cases there is a mix of two different slip systems. A lot of these samples have prism <a> as the active slip system. Throughout the transect there is a slight variation of active slip systems. Figures 11, 12 and 13 together are used to make interpretations of the quartz slip systems. This is done by matching the c-axis and the a-axis CPOs with figures 11 and 13. Figure 12 is compared to the inverse pole diagrams of the misorientation axis. According to the misorientation inverse pole figures, almost all samples excluding SI-104 and 105, have slip along prism <a> plane (Fig. 12 and 34). In addition to prism <a> slip, there are samples that also slip along the r plane and the z plane. This may indicate that there may be a combination of both prism <a> and basal <a> slip. While many of these indicate prism <a> as the slip system, samples SI-88, SI-89, SI-90, SI-91, and SI-92Q do not have the c-axis and a-axis patterns that are consistent with prism <a> (Fig. 13). These samples only indicate prism <a> in the misorientation axis plot. The CPO patterns don't match any of the other patterns for different slip systems (Fig. 13 and 34). There are two samples SI-104 and SI-105 that only have slip along the r and z plane. There is no indication that there is any prism <a> slip in these samples. These samples are >200 m, so it is a possibility the low amount of strain these rocks underwent should correlate to a lower temperature slip system. While this is a possibility samples SI-106 and 82 have distances farther at 243.5 and >400 respectively that contain prism <a> to be one of the planes that underwent slip. Samples 106P and SI82 may not have experienced the D_2 event, but instead is a result of the low temperature D_1 deformation that is not related to the SISZ. From Sample SI-83 at 7.2 m from the shear zone boundary and sample SI-95P at 71.3 m from the boundary, all are consistent with prism <a> slip indicated by the CPOs and the misorientation axis plot. SI-96Q (~73 m) is also consistent with prism<a>, but at >73 m

is where the slip systems change. At this distance the slip systems are variable from prism <a> to only slip on planes r and z strongly indicated by the patterns of the misorientation axis. This may be due to the increasing distance from the shear zone boundary where the strain is lower.

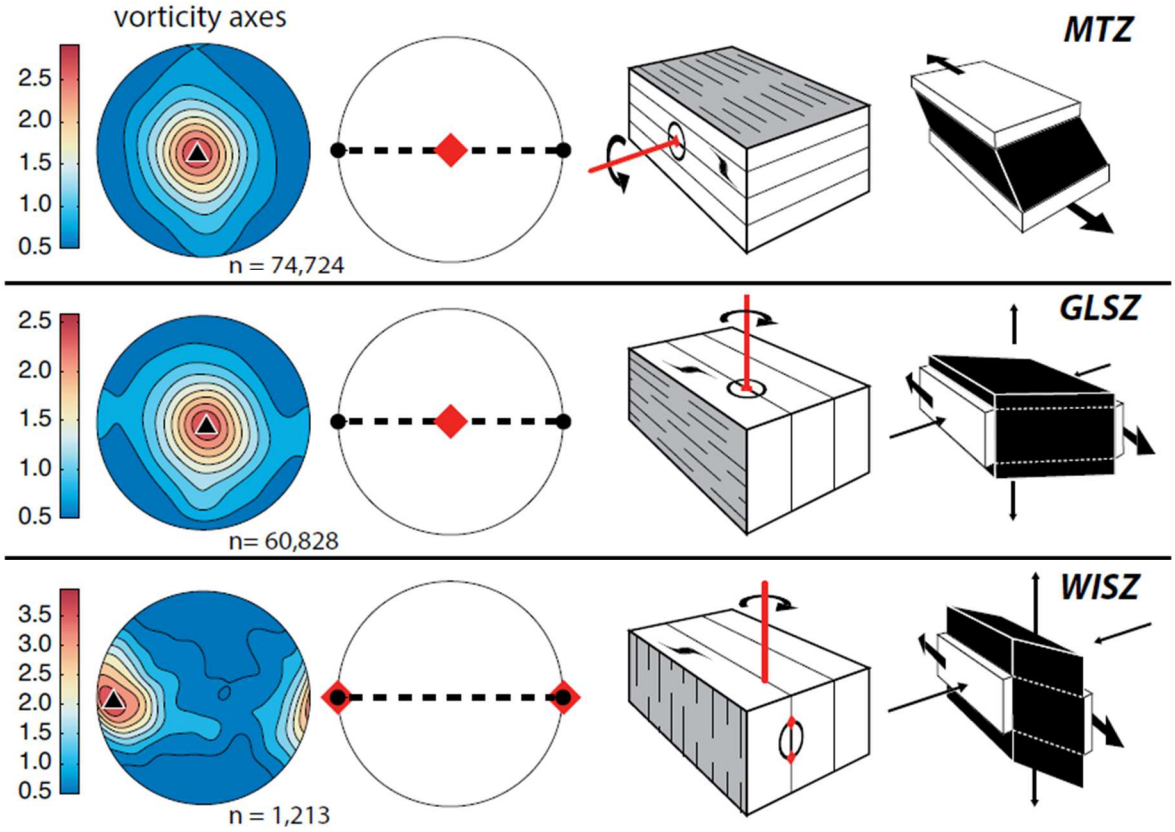

Figure 28: CVA patterns (left) that show the inferred kinematics of the shear zone. From Michels et al., 2015

The SISZ is known to have components of left-lateral simple shear thrusting. Field observations in the PdL indicate more thrusting, whereas in the BAM left-lateral dominates. To look for these components in the CVA plots, the lineation, foliation, and vorticity axis were plotted together to see if the vorticity vector and the lineation made sense with left-lateral simple shear or thrusting (Fig 35 to 44). The results of this were quite interesting because a lot of the

samples indicated a larger component of thrusting over left-lateral simple shear. However, there are some samples that don't make sense with the kinematics that are known about this shear zone. It leaves some questions about why some are different than others. Are there lithology differences, slip systems, or fluid interactions that caused some of these interesting lineations to form based on the vorticity vector? Does the kinematic partitioning between thrusting and left-lateral slip vary across the shear zone and at a smaller scale within the PdL?

For all the samples in which the CVA was found to be not perpendicular to the assumed lineation, the plots were rotated to try and make the vorticity vector appear perpendicular to the lineation. This was done in order to interpret the kinematics based on established models which There are a total of 10 plots that were rotated, but some of them were unable to be rotated to the middle of the CVA plot to avoid clockwise and counterclockwise rotation of the vorticity vector (Fig. 25). By rotating the vorticity vector, the CPO of the c and a axis of quartz slightly changed. When all the CPO plots were rotated for the vorticity vector to be perpendicular to the lineation, it revealed slightly different CPO patterns than the original CPOs. This is because these 10 samples used the vorticity vector's orientation to plot the c-axis and a-axis.

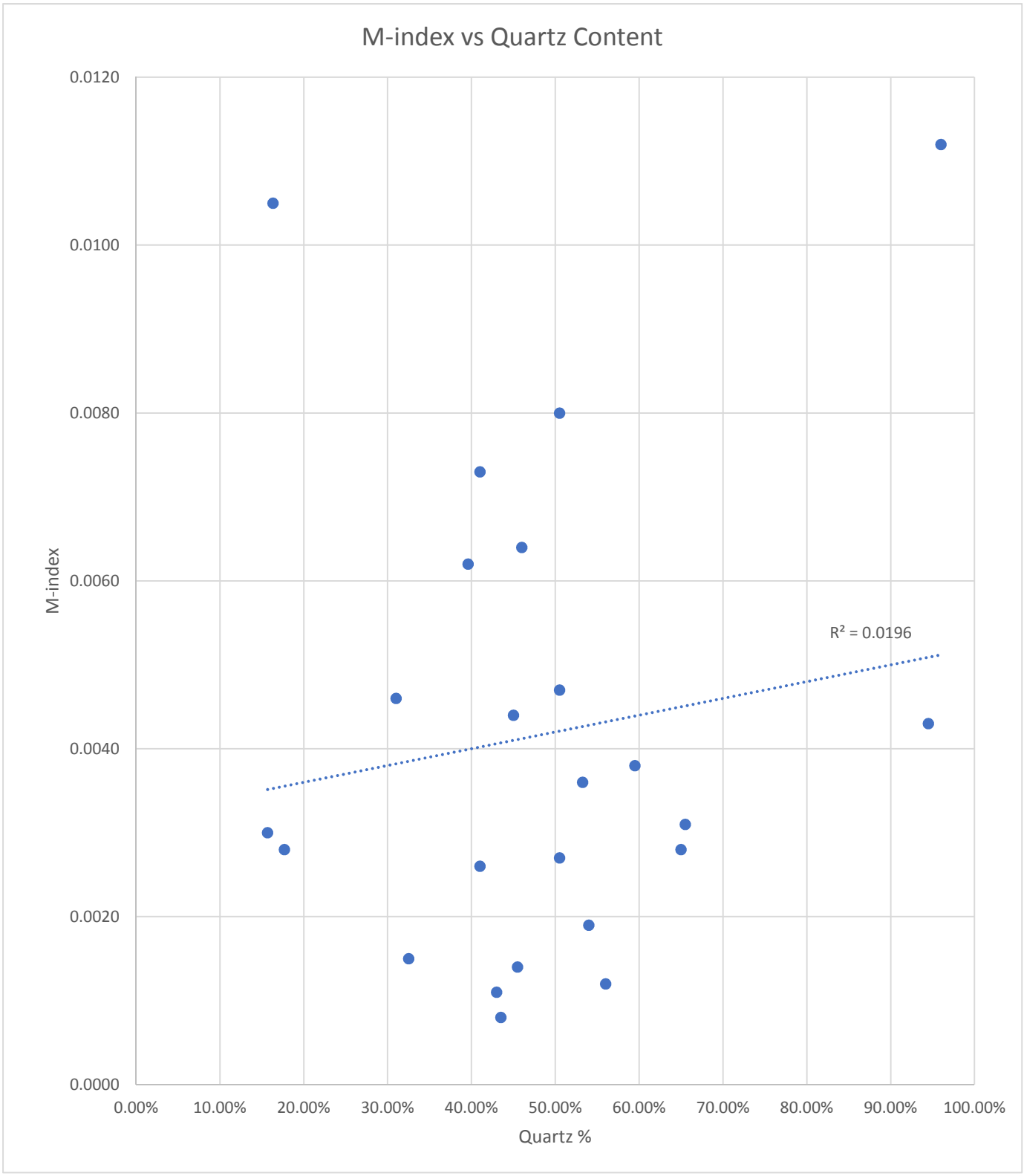

Figure 29: Relationship between the M-index of quartz CPOs and the quartz content determined from point counting.

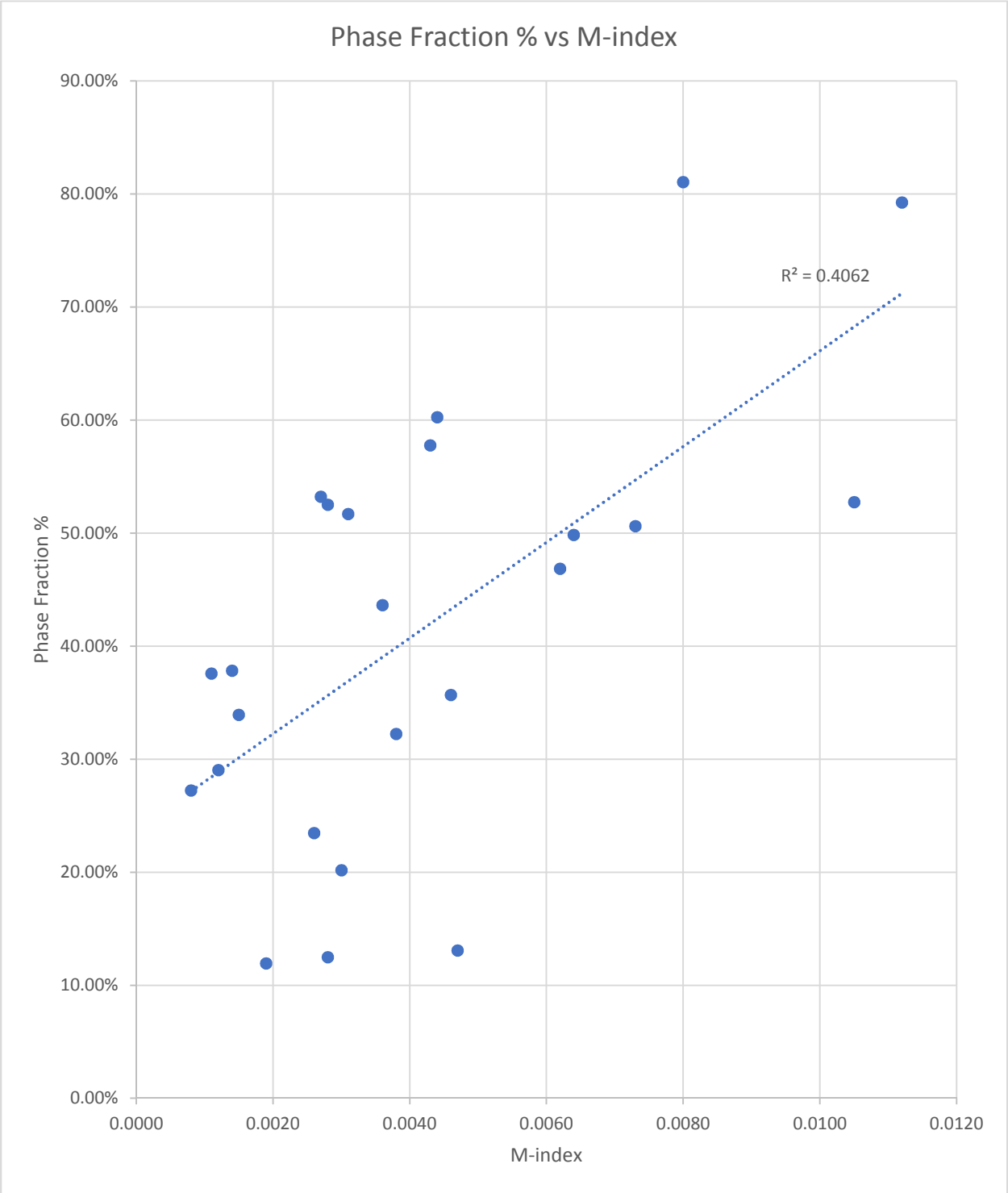

Figure 30: Relationship between percent of quartz that was indexed and the m-index of quartz CPOs.

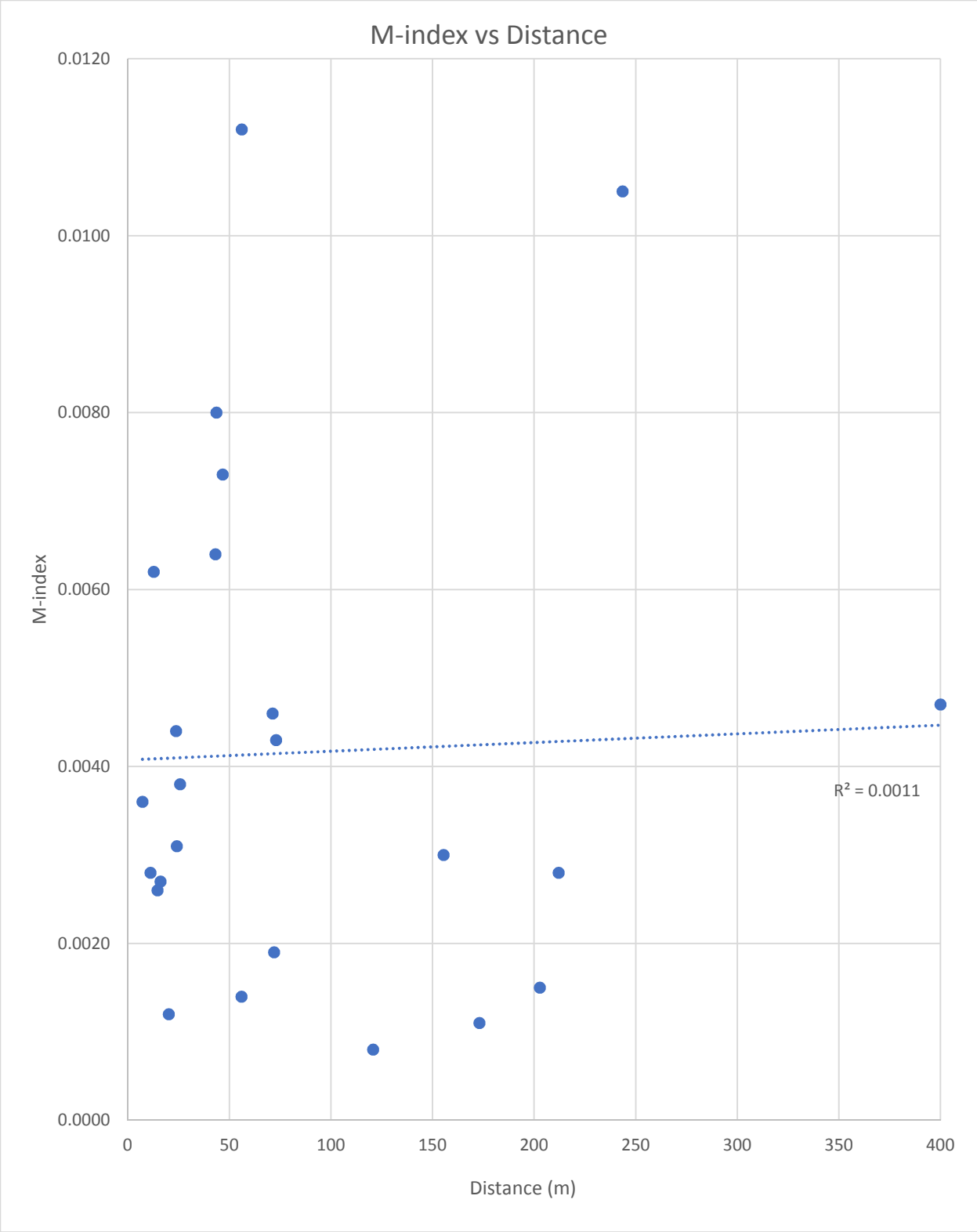

Figure 31: Relationship between the M-index of quartz CPOs and distance from the shear zone boundary.

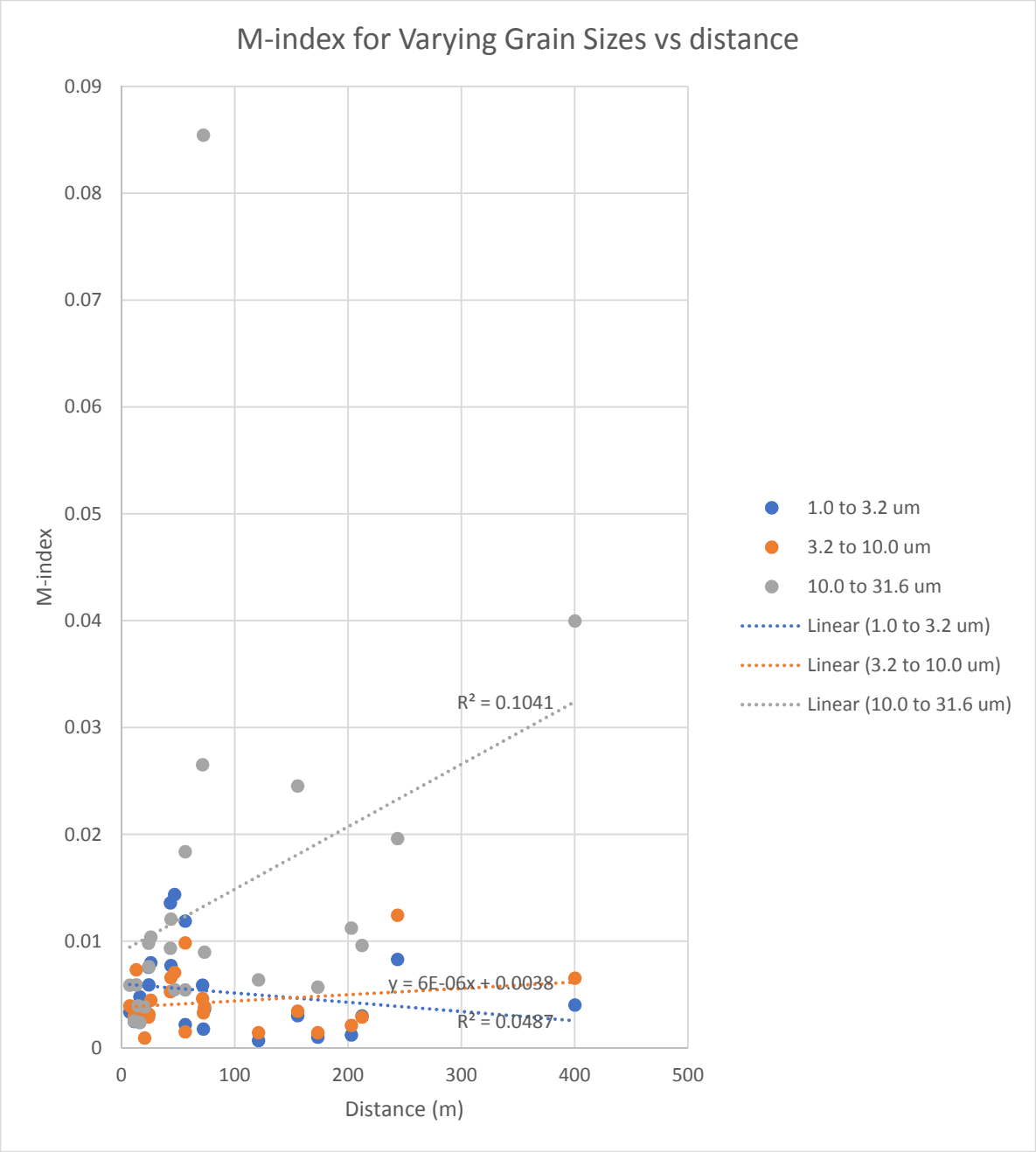

Figure 32**:** Relationship between M-index for varying grain size bins and the distance from the shear zone boundary.

Figure 33: Relationship between the M-index, distance, and the amount of quartz that was indexed.

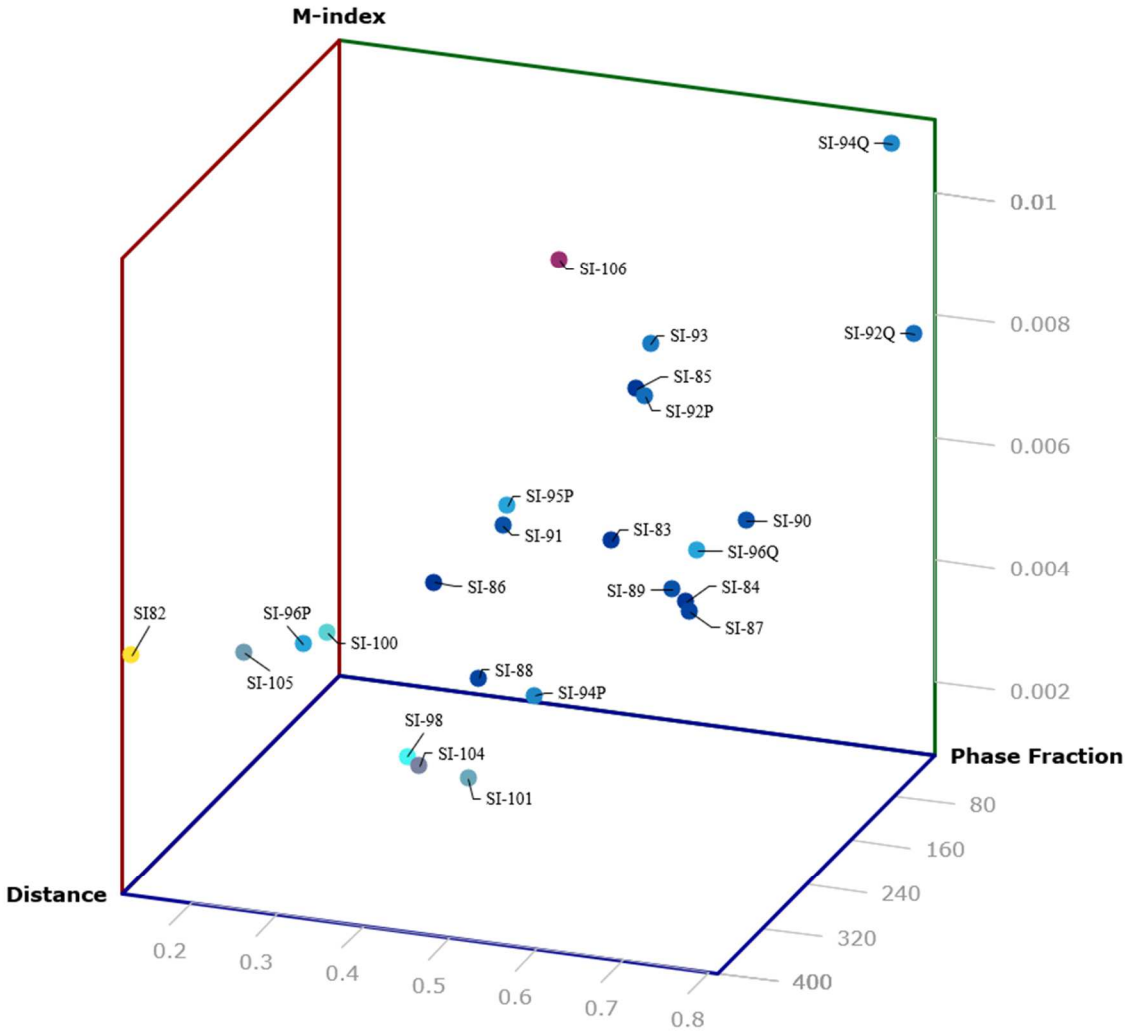

Figure 34: Sample map with the approximate locations of each sample and the corresponding quartz c-axis CPO. CPOs are ordered in distance from the shear zone. See Table 2 for distances and sample names. The map is rotated so that the foliation strike is horizontal on the page. The stereogram orientation can be found at the top right of the figure. The yellow line with arrows indicates the shear zone boundary.

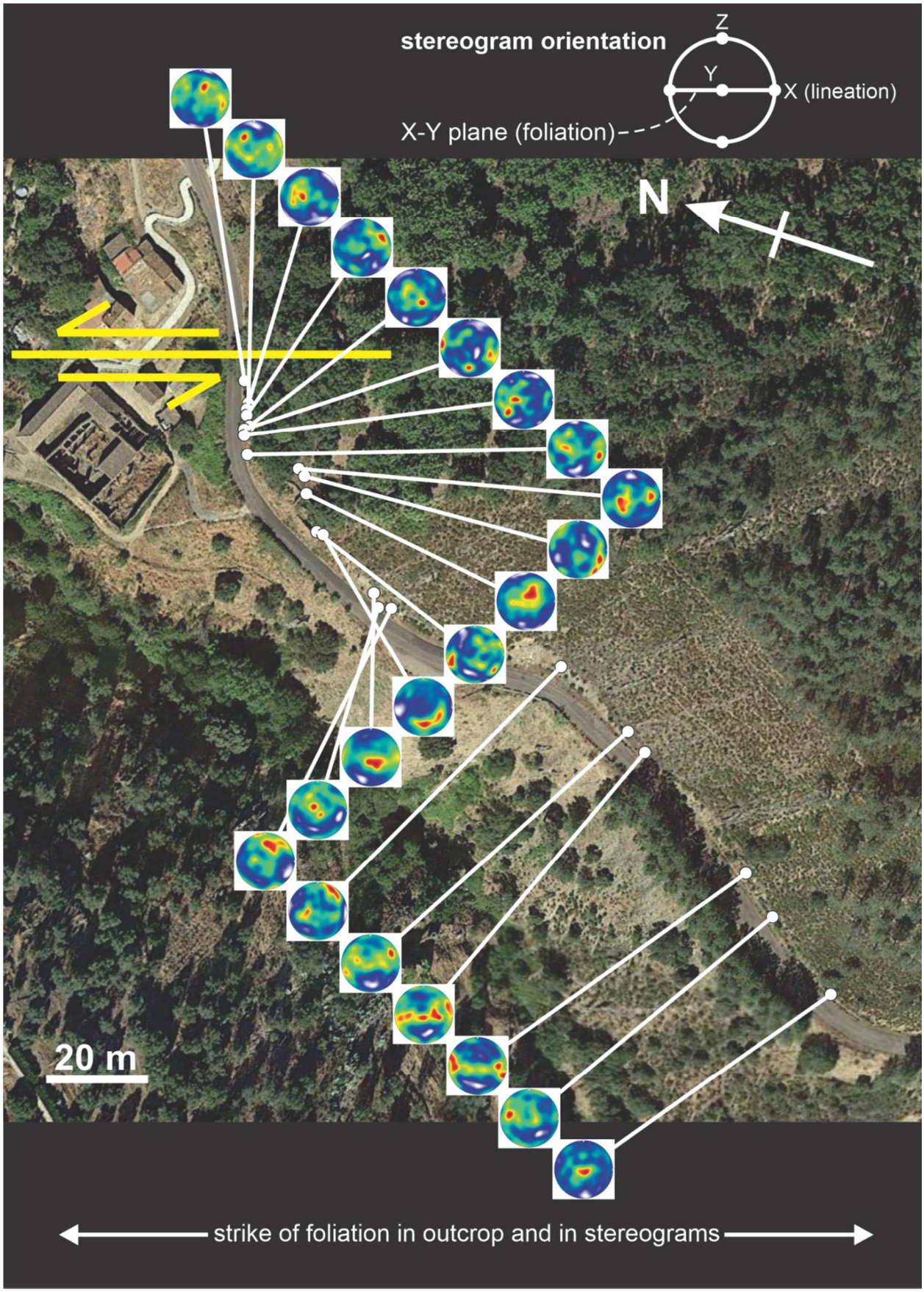
stereogram orientation
Z
Y
X (lineation)
X-Y plane (foliation)
N
20 m
strike of foliation in outcrop and in stereograms

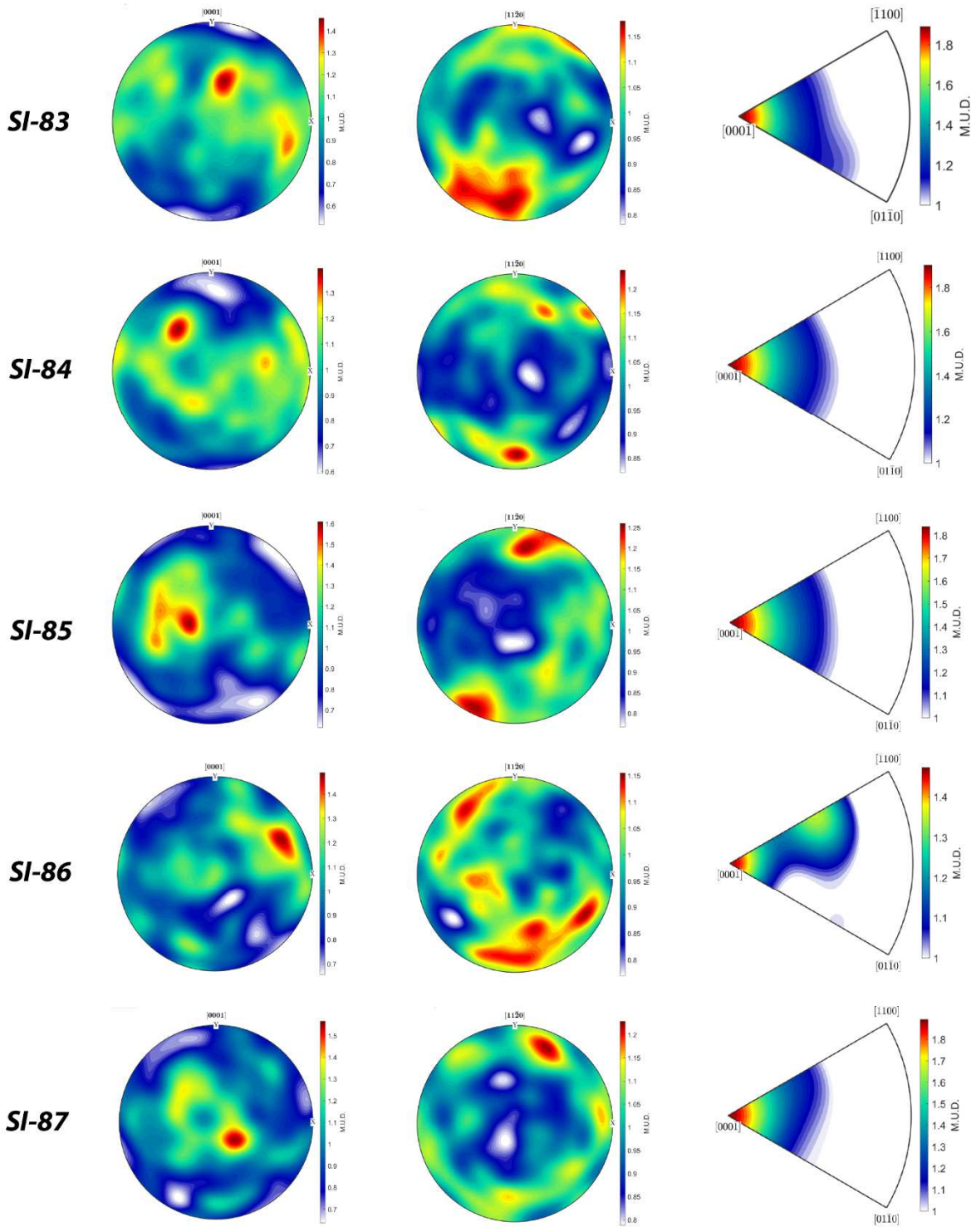

Figure 35: Quartz C-axis and A-axis CPOs with an inverse pole figure of the misorientation axis. The stereogram orientation is the same as in Figure 25.

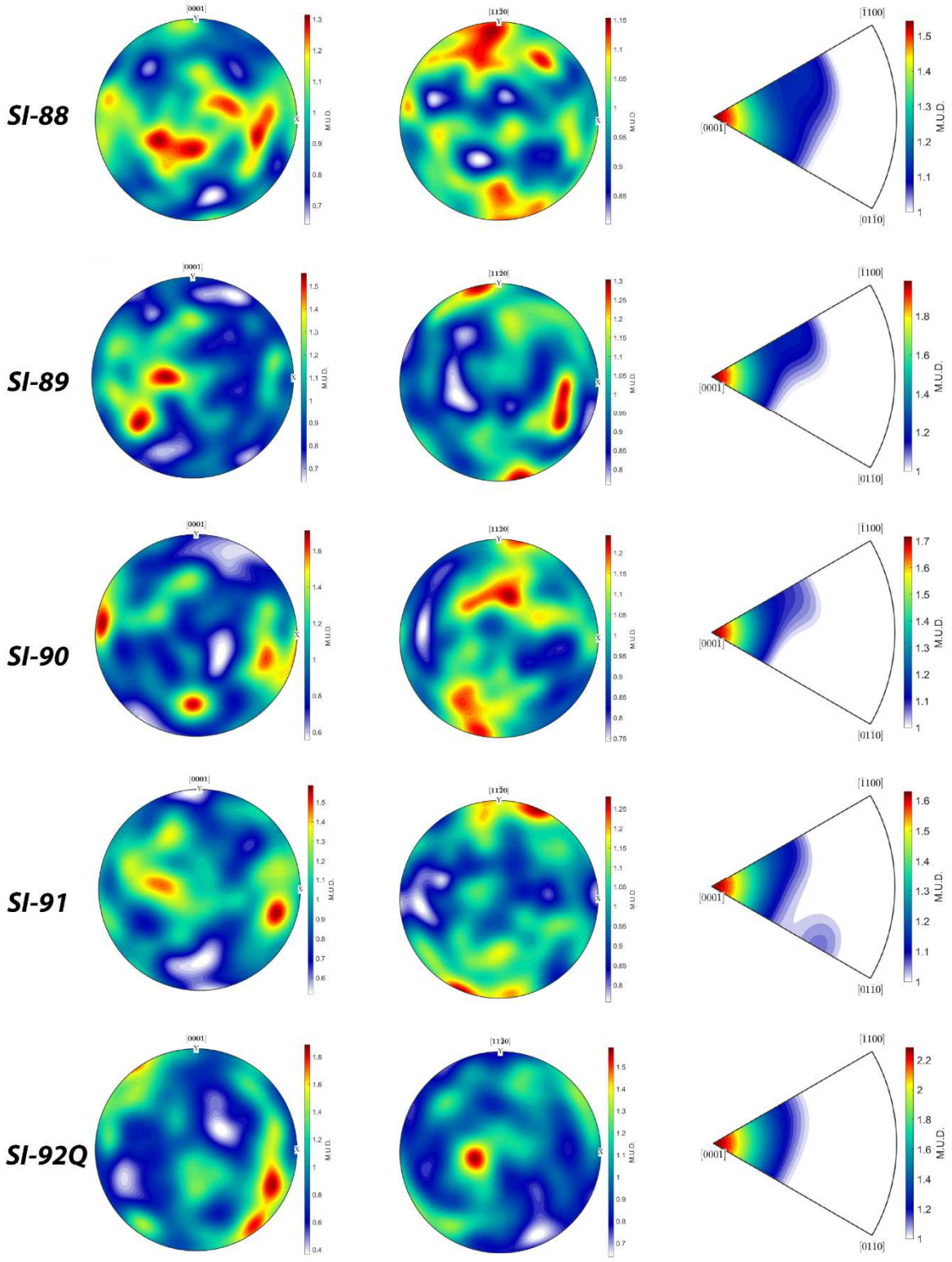

Figure 35 Continued

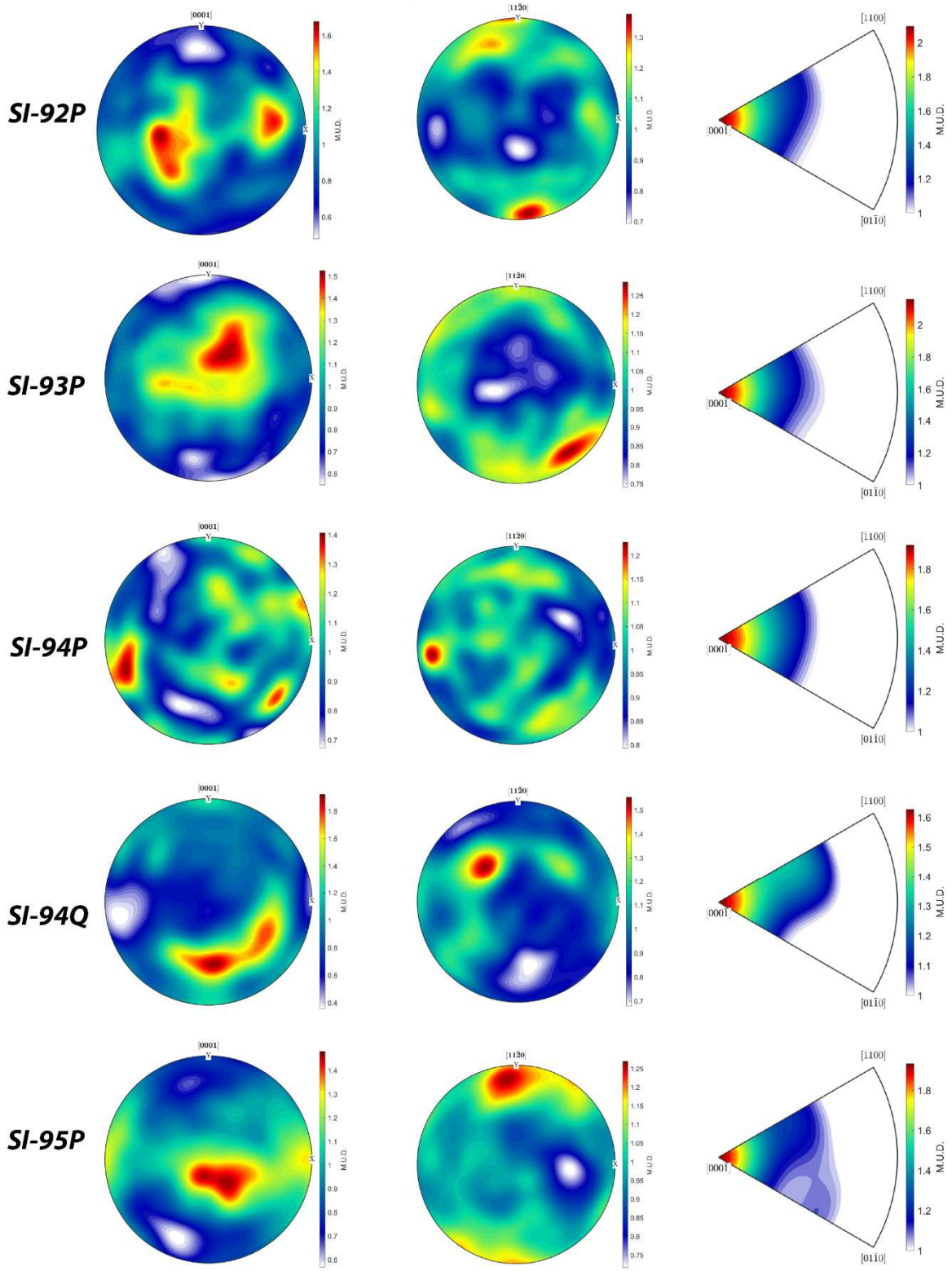

Figure 35 Continued

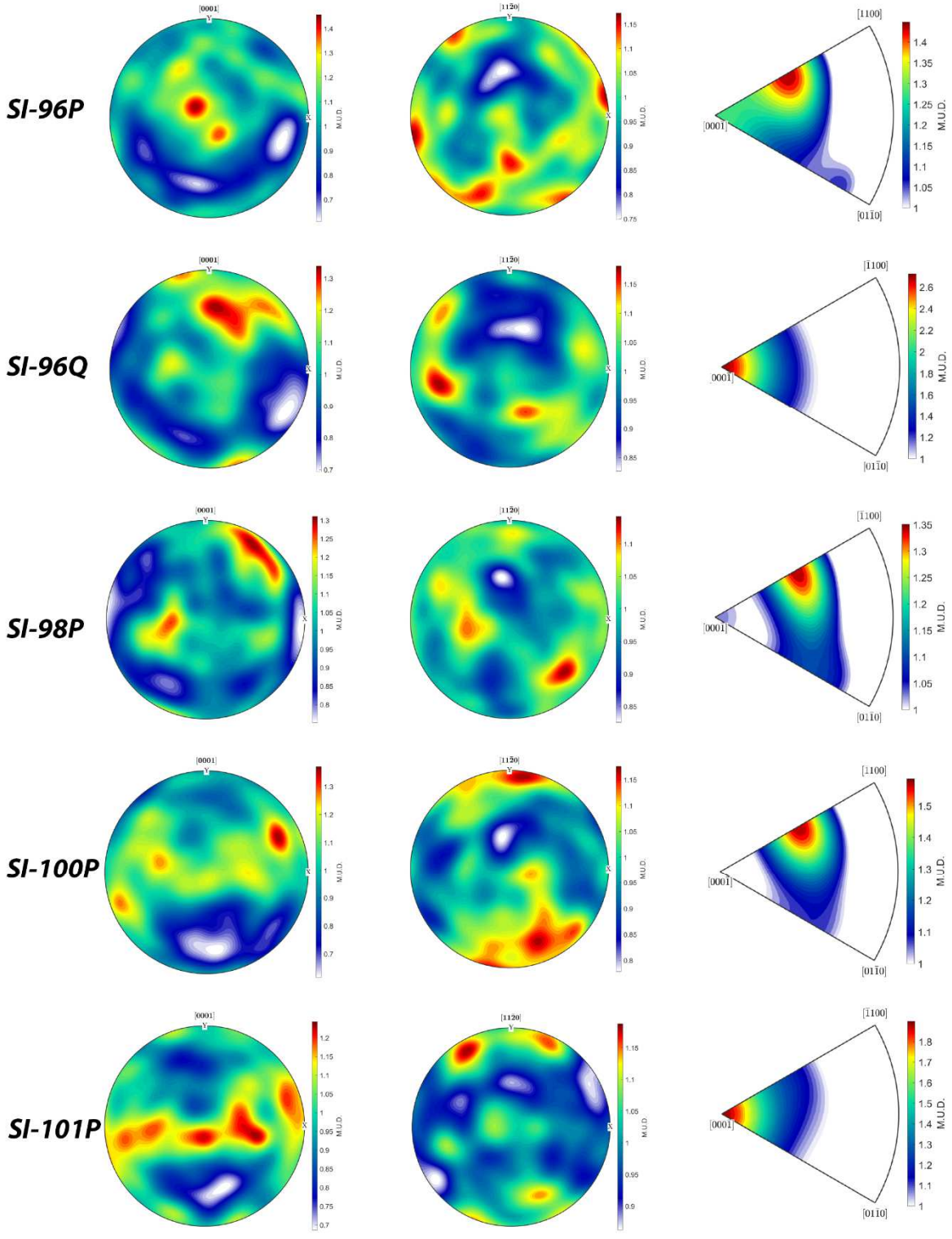

Figure 35 Continued

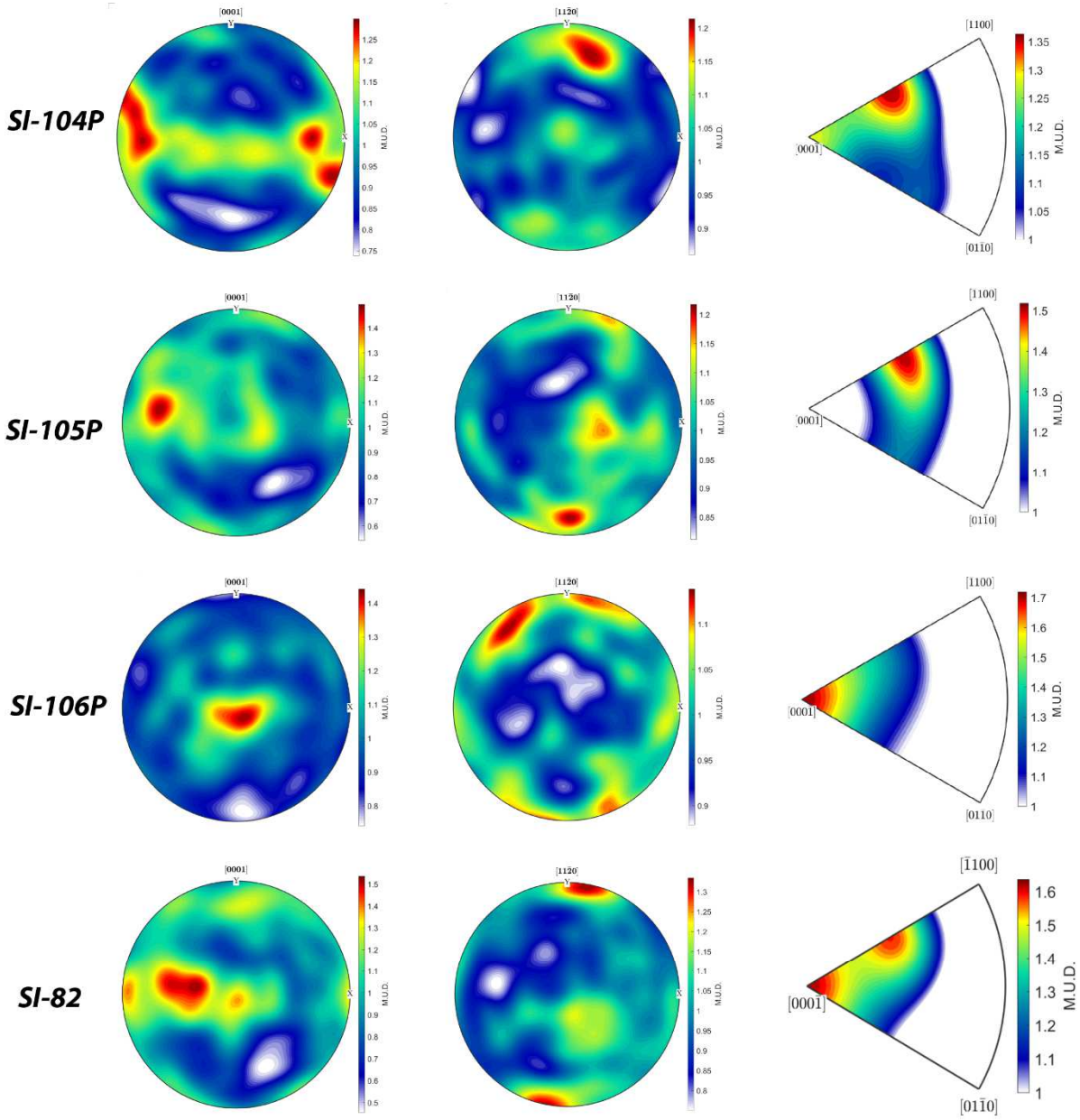

Figure 35 Continued

CHAPTER 6: Future Work

6.1 More kinematic study of the Pulo do Lobo affected by the SISZ

This project demonstrated that the kinematics of the SISZ are complex. There were key differences in kinematics between the metabasites on the north side of the shear zone with largely left-lateral shear and flattening and the PdL on the south side of the shear zone with largely oblique thrust/left-lateral shear and flattening. However, the new data in the PdL also indicate that there was meter and potentially sub-meter scale variation in kinematics. Further kinematic work is needed to accurately document this variation and determine the controlling factors. For the next phase of work, new samples should be collected and made into new thin sections. The samples that are collected should contain a lineation and a foliation so they can be observed in a geographical reference frame and not the specimen reference frame, and so the kinematic parameters are better understood. Due to the necessity of using previously collected samples because of pandemic related travel restrictions, this project lacked lineation and foliation data for most of the samples that were mapped by EBSD. Therefore, the CPO patterns and CVA analyses had to be compared to nearby field fabrics from nearby samples to put the results into geographic and kinematic context. However, the potential for small scale fabric variation may result in only tentative conclusions. Visible lineations in the field are rare, so samples can either be selected in key locations where they are found, or Anisotropy of Magnetic Susceptibility (AMS) can be used to find a tectonic lineation within samples, a promising technique studied by a member of our research group Devin Lang (research in progress).

Because many of these samples contain a high percentage of micas, the thin sections had relatively few quartz grains. Figure 28 shows the relationship between m-index and quartz composition. The more quartz that is in the thin section, the higher the m-index is; so if samples

were selected with more quartz or a larger map size was selected to index more quartz, maybe better or different patterns can be detected with stronger patterns. Based on observations made in this study, the whole section should be analyzed for quartz.

In addition, certain areas on the thin section should be specifically analyzed to evaluate whether the kinematics vary at the small scale due to composition. For example, there may be a connection between quartz c-axis orientations and mica content. It would be interesting to compare the quartz c-axis CPOs in areas where quartz is surrounded by micas to areas that have no micas interfering with the quartz deformation. This might provide a better understanding of the effects composition can have in strain and kinematic localization.

6.2 Detailed metamorphic study of the Pulo do Lobo affected by the SISZ

The data in this project has found potential inconsistences with the temperature inferred from metamorphic grade. With slip systems inferring higher temperatures, a detailed thermobarometry study would help to confidently determine the deformation temperature in the PdL. By using the TWEEQU method of Berman (1991) and the thermodynamic dataset of Berman (1988), the temperature can be better interpreted by using mineral phases chlorite and garnet (Horváth and Árkai, 2002).

CHAPTER 7: Conclusions

Compared to extensively studied Acebuches metabasites, deformation in the Pulo do Lobo unit is relatively understudied, with little knowledge of the kinematics, fluid interactions, and strain partitioning. This project and Carman (2020) have helped reveal interesting information how the Southern Iberian Shear Zone affected lithologies within the PdL.

Microstructural observations by Carman (2020) and in this study indicated that deformation mechanisms in the PdL associated with the SISZ were complex with brittle mechanisms, DMT, and dislocation creep all active within quartz. Quartz Crystallographic Preferred Orientation (CPO) plots derived from EBSD data were used for further analysis to understand the relative importance of dislocation creep as a deformation mechanism. Quartz CPO patterns were weak, indicating that diffusional processes likely dominated deformation, but dislocation was an important coeval mechanism. Strength of the patterns was dependent on both proximity to the SISZ and quartz concentration, increasing with both. These patterns suggest that both the amount of strain accommodated by dislocation creep increased near the shear zone, and also that the relative importance of dislocation creep was higher in quartz-rich samples. Conversely, mica-rich samples were likely even more dominantly deformed by DMT. The microstructural and metamorphic evidence that suggests fluid flow was channelized near the shear zone likely enhanced both the DMT through faster diffusion rates and dislocation creep through hydrolytic weakening.

The EBSD data, including quartz c-axis and a-axis CPOs and inverse pole diagrams of the misorientation axis, also aided in understanding quartz slip systems that were active during deformation and the deformation temperature of the SISZ. Overall, these rocks underwent slip along the prism <a> plane, with minor slip along the R and Z planes. Prism <a> is active around temperatures of 500°

C and above and these results are broadly compatible with previous metamorphic temperature estimates, at least of rocks close to the shear zone.

However, these rocks did not undergo temperatures much higher than 500° C. Previous studies report peak metamorphism in the PdL reached greenschist facies with temperatures of 400-450° C (Ábalos et al., 2002); however metamorphic conditions in the PdL near the SISZ boundary have not been extensively studied. The temperature interpreted from the quartz slip systems is compatible with metamorphic evidence near the SISZ where chlorite and garnet formed, but incompatible with metamorphic evidence >180 m away from the shear zone where the rocks were slates with low-T metamorphic minerals. Further metamorphic work is warranted to understand this potential discrepancy.

The CPOs of quartz with the addition of a CVA analysis, were used to further understand the kinematics of the shear zone. First, it is clear that the kinematics associated with the SISZ are different within the PdL and the BAM. The kinematics of the BAM are less complex, dominated by transpression with left-lateral shear and somewhat variable oblique extrusion direction. The kinematics throughout the PdL is very complex as they seem to change throughout the studied transect (7.2 m to >400 m from the SISZ boundary). In a broad sense, the majority of the samples fit a sinistral triclinic transpression model. While this matches the kinematic model for the BAM, the PdL kinematics are still not fully understood. For example, the CVA analyses indicate that the orientation of the vorticity vector varies throughout the transect, which likely explains at least some of the variation in lineation orientation. This variation in effect means that there were different combinations of left-lateral and thrust components of deformation throughout the transect. Some samples were deformed by transpression in which the simple shear component was dominated by thrust motion while others were deformed by transpression in

which the simple shear component was dominated by left-lateral motion. Still others were deformed via transpression with oblique simple shear. These variations in the orientation of the vorticity vector occur at least at the meter scale, but further studies are needed to see if they vary at smaller scales. It is also possible that the degree of flattening or extrusion angle vary across the PdL transect, but current data do not allow evaluation of those hypotheses

There are many factors that likely control strain partitioning within the PdL. This study provided data that advance our knowledge of strain partitioning in these rocks. First, this study documented more detailed deformation mechanisms, particularly in the dominant mineral quartz. Interestingly, the deformation mechanisms did not substantially vary across the transect regardless of lithology or presumed strain magnitude. In all cases, DMT dominated the quartz deformation mechanisms, but dislocation creep also played a substantial role, and brittle processes a minor role. While the amount of dislocation creep was higher near the shear zone and with higher modal quartz abundance, it is not known whether the relative contribution of dislocation creep and DMT varied. Second, this study documented that at least one aspect of strain, kinematic framework, was heavily localized, both across the SISZ boundary and within the PdL. It will be interesting to see if future studies find a relationship between this kinematic localization and mineralogy, grain size, strain magnitude, or other factors.

CHAPTER 8: References

Aspiroz, M.D., Lloyd, G.E. and Fernández, C., 2007. Development of lattice preferred orientation in clinoamphiboles deformed under low-pressure metamorphic conditions. A SEM/EBSD study of metabasites from the Aracena metamorphic belt (SW Spain). Journal of Structural Geology, 29(4), pp.629-645.

Ayarza, P., Martinez Catalan, J.R., Martinez Garcia, A., Alcalde, J., Andrés, J., Fernando Simancas, J., Palomeras, I., Martí, D., DeFelipe, I., Juhlin, C. and Carbonell, R., 2021. Evolution of the Iberian Massif as deduced from its crustal thickness and geometry of a mid-crustal (Conrad) discontinuity. Solid Earth, 12(7), pp.1515-1547.

Azor, A., Rubatto, D., Simancas, J.F., González Lodeiro, F., Martínez Poyatos, D., Martín Parra, L.M., Matas, J., 2008. Rheic Ocean ophiolitic remnants in Southern Iberia questioned by SHRIMP U Pb zircon ages on the Beja-Acebuches amphibolites. Tectonics 27, TC5006.

Azpiroz, M.D. and Fernández, C., 2003. Characterization of tectono-metamorphic events using crystal size distribution (CSD) diagrams. A case study from the Acebuches metabasites (SW Spain). Journal of Structural Geology, 25(6), pp.935-947.

Bard, J.P. and Moine, B., 1979. Acebuches amphibolites in the Aracena hercynian metamorphic belt (southwest Spain): Geochemical variations and basaltic affinities. Lithos, 12(4), pp.271-282.

Barth, N.C., Hacker, B.R., Seward, G.G., Walsh, E.O., Young, D. and Johnston, S., 2010. Strain within the ultrahigh-pressure Western Gneiss region of Norway recorded by quartz CPOs. Geological Society, London, Special Publications, 335(1), pp.663-685.

Berman, R.G. 1988: Internally-consistent thermodynamic data for minerals in the system Na2OK2O-CaO-MgO-FeO-Fe2O3-Al2O3-TiO2-H2O-CO2. J. Petrol., 29, pp. 445522.

Berman, R.G. 1991: Thermobarometry using multi-equilibrium calculations. A new technique, with petrologic applications. Can. Mineral., 29, pp. 835855.

Braid, J.A., Murphy, J.B. and Quesada, C., 2010. Structural analysis of an accretionary prism in a continental collisional setting, the Late Paleozoic Pulo do Lobo Zone, Southern Iberia. Gondwana Research, 17(2-3), pp.422-439.

Braid, J.A., Murphy, J.B., Quesada, C., Bickerton, L. and Mortensen, J.K., 2012. Probing the composition of unexposed basement, South Portuguese Zone, southern Iberia: implications for the connections between the Appalachian and Variscan orogens. Canadian Journal of Earth Sciences, 49(4), pp.591-613.

Carman, N., 2020 Analyzing strain localization, kinematic partitioning and fluid flow in the Pulo do Lobo metasedimentary rocks along the Southern Iberian shear zone, Andalucia, Spain. MS Thesis. University of Wisconsin-Milwaukee, 133 pages.

Carter, N.L., Kronenberg, A.K., Ross, J.V. and Wiltschko, D.V., 1990. Control of fluids on deformation of rocks. Geological Society, London, Special Publications, 54(1), pp.1-13.

Castro, A., Fernandez, C., de La Rosa, J.D., Moreno-Ventas, I. and Rogers, G., 1996. Significance of MORB-derived amphibolites from the Aracena metamorphic belt, southwest Spain. Journal of Petrology, 37(2), pp.235-260.

Chen, S., Zhang, B., Zhang, J., Wang, Y., Li, X., Zhang, L., Yan, Y., Cai, F. and Yue, Y., 2022. Tectonic transformation from orogen-perpendicular to orogen-parallel extension in the North Himalayan Gneiss Domes: Evidence from a structural, kinematic, and geochronological investigation of the Ramba gneiss dome. Journal of Structural Geology, 155, p.104527.

Crespo-Blanc, A. and Orozco, M., 1988. The Southern Iberian Shear Zone: a major boundary in the Hercynian folded belt. Tectonophysics, 148(3-4), pp.221-227.

Cross, A.J., Hirth, G. and Prior, D.J., 2017. Effects of secondary phases on crystallographic preferred orientations in mylonites. Geology, 45(10), pp.955-958.

Czeck, D.M. and Hudleston, P.J., 2003. Testing models for obliquely plunging lineations in transpression: a natural example and theoretical discussion. Journal of Structural Geology, 25(6), pp.959-982.

Czeck, D.M., Stephenson, S.I., Díaz-Azpiroz, M., Fernández, C., García-Arias, M., 2019. Syndeformational fluid flow in metabasite rocks along the Southern Iberian Shear Zone. Geological Society of America Abstracts with Programs 51, No. 5. Phoenix, AZ.

Díaz Azpiroz, M., Fernández, C., 2005. Kinematic analysis of the southern Iberian shear zone and tectonic evolution of the Acebuches metabasites (SW Variscan Iberian Massif). Tectonics 24, TC3010.

Díaz-Azpiroz, M., Fernández, C. and Czeck, D.M., 2019. Are we studying deformed rocks in the right sections? Best practices in the kinematic analysis of 3D deformation zones. Journal of Structural Geology, 125, pp.218-225.

Díaz-Azpiroz, M. and Fernández, C., 2021. The Southern Iberian Shear Zone (SW Spain): Inclined transpression related to Variscan oblique convergence in a HT/LP metamorphic belt. In Structural Geology and Tectonics Field Guidebook—Volume 1 (pp. 137-166). Springer, Cham.

Dutta, D. and Mukherjee, S., 2021. Extrusion kinematics of UHP terrane in a collisional orogen: EBSD and microstructure-based approach from the Tso Morari Crystallines (Ladakh Himalaya). Tectonophysics, 800, p.228641.

Faleiros, F.M., Moraes, R.D., Pavan, M. and Campanha, G.A.D.C., 2016. A new empirical calibration of the quartz c-axis fabric opening-angle deformation thermometer. Tectonophysics, 671, pp.173-182.

Fazio, E., Punturo, R., Cirrincione, R., Kern, H., Pezzino, A., Wenk, H. R., ... & Mamtani, M. A. 2017. Quartz preferred orientation in naturally deformed mylonitic rocks (Montalto shear zone–Italy): a comparison of results by different techniques, their advantages and limitations. International Journal of Earth Sciences, 106(7), pp.2259-2278.

Fernández, C., Czeck, D.M. and Diaz-Azpiroz, M., 2013. Testing the model of oblique transpression with oblique extrusion in two natural cases: steps and consequences. Journal of Structural Geology, 54, pp.85-102.

Fossen, H. and Tikoff, B., 1993. The deformation matrix for simultaneous simple shearing, pure shearing and volume change, and its application to transpression-transtension tectonics. Journal of Structural Geology, 15(3-5), pp.413-422.

Fossen, H., 2016. Structural geology. Cambridge university press.

Fukuda, J.I., Holyoke III, C.W. and Kronenberg, A.K., 2018. Deformation of fine□grained quartz aggregates by mixed diffusion and dislocation creep. Journal of Geophysical Research: Solid Earth, 123(6), pp.4676-4696.

García□Navarro, E. and Fernández, C., 2004. Final stages of the Variscan orogeny at the southern Iberian massif: Lateral extrusion and rotation of continental blocks. Tectonics, 23(6).

Getsinger, A.J., Hirth, G., Stünitz, H. and Goergen, E.T., 2013. Influence of water on rheology and strain localization in the lower continental crust. Geochemistry, Geophysics, Geosystems, 14(7), pp.2247-2264.

Goswami, S., Mamtani, M.A. and Rana, V., 2018. Quartz CPO and kinematic analysis in deformed rocks devoid of visible stretching lineations: An integrated AMS and EBSD investigation. Journal of Structural Geology, 115, pp.270-283.

Horsman, E. and Tikoff, B., 2005. Quantifying simultaneous discrete and distributed deformation. Journal of Structural Geology, 27(7), pp.1168-1189.

Horsman, E., Tikoff, B. and Czeck, D., 2008. Rheological implications of heterogeneous deformation at multiple scales in the Late Cretaceous Sierra Nevada, California. Geological Society of America Bulletin, 120(1-2), pp.238-255.

Horváth, P. and Árkai, P., 2002. Pressure-temperature path of metapelites from the Algyő-Ferencszállás area, SE Hungary: thermobarometric constraints from coexisting mineral assemblages and garnet zoning. Acta Geologica Hungarica, 45(1), pp.1-27.

Huntington, K.W. and Klepeis, K.A., 2018. Challenges and opportunities for research in tectonics: Understanding deformation and the processes that link Earth systems, from geologic time to human time. A community vision document submitted to the US National Science Foundation.

Kruckenberg, S. C., Michels, Z. D., & Parsons, M. M. 2019. From intracrystalline distortion to plate motion: Unifying structural, kinematic, and textural analysis in heterogeneous

shear zones through crystallographic orientation-dispersion methods. Geosphere, 15(2), pp.357-381.

Law, R.D., Casey, M. and Knipe, R.J., 1986. Kinematic and tectonic significance of microstructures and crystallographic fabrics within quartz mylonites from the Assynt and Eriboll regions of the Moine thrust zone, NW Scotland. Earth and Environmental Science Transactions of The Royal Society of Edinburgh, 77(2), pp.99-125.

Law, R.D. and Johnson, M.R.W., 2010. Microstructures and crystal fabrics of the Moine Thrust zone and Moine Nappe: history of research and changing tectonic interpretations. Geological Society, London, Special Publications, 335(1), pp.443-503.

Little, T.A., Prior, D.J., Toy, V.G. and Lindroos, Z.R., 2015. The link between strength of lattice preferred orientation, second phase content and grain boundary migration: A case study from the Alpine Fault zone, New Zealand. Journal of Structural Geology, 81, pp.59-77.

Lin, A., Miyata, T. and Wan, T., 1998. Tectonic characteristics of the central segment of the Tancheng–Lujiang fault zone, Shandong Peninsula, eastern China. Tectonophysics, 293(1-2), pp.85-104.

Michels, Z.D., Kruckenberg, S.C., Davis, J.R. and Tikoff, B., 2015. Determining vorticity axes from grain-scale dispersion of crystallographic orientations. Geology, 43(9), pp.803-806.

Norris, R.J. and Cooper, A.F., 1995. Origin of small-scale segmentation and transpressional thrusting along the Alpine fault, New Zealand. Geological Society of America Bulletin, 107(2), pp.231-240.

Okudaira, T., Takeshita, T., Hara, I. and Ando, J.I., 1995. A new estimate of the conditions for transition from basal< a> to prism [c] slip in naturally deformed quartz. Tectonophysics, 250(1-3), pp.31-46.

Parsons, A.J., Law, R.D., Lloyd, G.E., Phillips, R.J. and Searle, M.P., 2016. Thermo□kinematic evolution of the Annapurna□Dhaulagiri Himalaya, central Nepal: The Composite Orogenic System. Geochemistry, Geophysics, Geosystems, 17(4), pp.1511-1539.

Passchier, C. W. & Trouw, R. A. J., 1998. Microtectonics. Germany: Springer-Verlag Berlin Heidelberg.

Pérez-Cáceres, I., Martínez Poyatos, D.J., Vidal, O., Beyssac, O., Nieto, F., Simancas, J.F., Azor, A. and Bourdelle, F., 2020. Deciphering the metamorphic evolution of the Pulo do Lobo metasedimentary domain (SW Iberian Variscides). Solid Earth, 11(2), pp.469-488.

Rahl, J. M. & Skemer, P., 2016. Microstructural evolution and rheology of quartz in a mid-crustal shear zone. Tectonophysics 680, 129-139.

Ramsay, J.G., 1967. Folding and fracturing of rocks. Mc Graw Hill Book Company, 568.

Ramsay, J.G. and Graham, R.H., 1970. Strain variation in shear belts. Canadian Journal of Earth Sciences, 7(3), pp.786-813.

Renjith, A.R. and Mamtani, M.A., 2014. Domainal petrofabric analysis of micaceous quartzite using EBSD data: role of muscovite in LPO evolution of quartz. Journal of the Geological Society of India, 83(5), pp.479-482.

Romeo, I., Capote, R. and Lunar, R., 2007. Crystallographic preferred orientations and microstructure of a Variscan marble mylonite in the Ossa-Morena Zone (SW Iberia). Journal of structural geology, 29(8), pp.1353-1368.

Schmidt, W.L. and Platt, J.P., 2022. Stress, microstructure, and deformation mechanisms during subduction underplating at the depth of tremor and slow slip, Franciscan Complex, northern California. Journal of Structural Geology, 154, p.104469.

Skemer, P., Katayama, I., Jiang, Z. and Karato, S.I., 2005. The misorientation index: Development of a new method for calculating the strength of lattice-preferred orientation. Tectonophysics, 411(1-4), pp.157-167.

Stephenson, S. I., 2018. Characterizing the geochemical changes across a strain gradient in the Beja-Acebuches metabasites due to retrograde metamorphism and fluid flow along the Southern Iberian Shear Zone. MS Thesis. University of Wisconsin-Milwaukee, 112 pages.

Sullivan, W.A. and Law, R.D., 2007. Deformation path partitioning within the transpressional White Mountain shear zone, California and Nevada. Journal of Structural Geology, 29(4), pp.583-599.

Takeshita, T. and Hara, I., 1998. c-Axis fabrics and microstructures in a recrystallized quartz vein deformed under fluid-rich greenschist conditions. Journal of Structural Geology, 20(4), pp.417-431.

Thigpen, J.R., Law, R.D., Lloyd, G.E., Brown, S.J. and Cook, B., 2010. Deformation temperatures, vorticity of flow and strain symmetry in the Loch Eriboll mylonites, NW Scotland: implications for the kinematic and structural evolution of the northernmost Moine Thrust zone. Geological Society, London, Special Publications, 335(1), pp.623-662.

Toy, V.G., Prior, D.J. and Norris, R.J., 2008. Quartz fabrics in the Alpine Fault mylonites: Influence of pre-existing preferred orientations on fabric development during progressive uplift. Journal of Structural Geology, 30(5), pp.602-621.

Vernon, R.H., 2004, A practical guide to rock microstructure, Cambridge University Press, Cambridge, UK..

Wenk, H.R., Yu, R., Vogel, S. and Vasin, R., 2019. Preferred orientation of quartz in metamorphic rocks from the Bergell Alps. Minerals, 9(5), p.277.

Winter, J.D., 2014. Principles of Igneous and Metamorphic Petrology Second Edition, Pearson Education Limited.

Chapter 9: Appendices

9.1 Pulo do Lobo sample mineralogy and microstructures

Sample ID	Distance from shear zone (m)	Mineralogy	Microstructures (In quartz, micas, and feldspar)
SI-83	7.2	Quartz, biotite, muscovite, garnet, plagioclase	Bulging, subgrains, recrystallization, undulose extinction, solution seams, strain shadows, intergranular fractures, folds
SI-84	11.2	Quartz, biotite, muscovite, garnet, plagioclase, zircon	Intergranular fracture, strain shadows, bulging, subgrains, solution seams, recrystallization, undulose extinction, deformation lamellae, intragranular fracture
SI-85	12.8	Quartz, biotite, muscovite, garnet, plagioclase	Solution seams, strain shadows, undulose extinction, boudin veins, intragranular fracture, bulging, triple junctions, subgrains, recrystallization, fluid inclusions, GBM, folding
SI-86	14.6	Quartz, biotite, muscovite, garnet, plagioclase, opaques	Subgrains, bulging, undulose extinction, strain shadows, solution seams, fluid inclusions, recrystallization, intragranular fracture
SI-87	16.1	Quartz, biotite, muscovite, garnet, plagioclase, chlorite	Solution seams, strain shadows, deformation lamellae, bulging, subgrains, recrystallization, intragranular fracture, undulose extinction, folds
SI-88	20.2	Quartz, biotite, muscovite, garnet, plagioclase, chlorite	Solution seams, bulging, subgrains, strain shadows, recrystallization, undulose extinction

SI-89	24.1	Quartz, biotite, muscovite, garnet, plagioclase, zircon	Deformation lamellae, strain shadows, solution seams, subgrains, recrystallization, bulging, mica kinks, quartz veins
SI-90	23.8	Quartz, biotite, muscovite, garnet, plagioclase, chlorite	Deformation twins, fractures, undulose extinction, subgrains, fluid inclusions, bulging, recrystallization
SI-91	25.8	Quartz, biotite, muscovite, garnet, zircon	Recrystallization, strain shadows, undulose extinction, subgrains, solution seams, crenulation cleavage, bulging
SI-92Q	43.6	Quartz, biotite, muscovite, garnet, plagioclase	Recrystallization, undulose extinction, strain shadows, subgrains, bulging, folds, solution seams
SI-92P	43.1	Quartz, biotite, muscovite, garnet, plagioclase, chlorite	Undulose extinction, recrystallization, bulging, subgrains, strain shadows
SI-93P	46.7	Quartz, biotite, muscovite	Deformation lamellae, strain shadows, recrystallization, bulging, undulose extinction, subgrains, solution seams
SI-94Q	56.0	Quartz, biotite, muscovite, zircon	Recrystallization, bulging, undulose extinction, subgrains,
SI-94P	56.1	Quartz, biotite, muscovite, garnet, opaques, zircon	Subgrains, recrystallization, bulging, undulose extinction, strain shadows, deformation lamellae, fluid inclusions, boudins
SI-95P	71.3	Quartz, biotite, muscovite, plagioclase	Undulose extinction, recrystallization, mica kinks, bulging, subgrains, fluid inclusions, solution seams, crenulation cleavage, strain shadows, boudins
SI-96P	72	Quartz, biotite, muscovite, garnet	(hard to see microstructures with the small grain size) likely there is not any
SI-96Q	73	Quartz, biotite, muscovite	Subgrains, undulose extinction, strain shadows, bulging, deformation lamellae

SI-98P	120.7	Quartz, biotite, muscovite	Seritization, strain shadows, recrystallization, solution seams, crenulation cleavage, unduloase extinction
SI-100P	155.4	Quartz, biotite, muscovite, zircon, staurolite, opaques	Undulose extinction, subgrains, solution seams, strain shadows
SI-101P	173.0	Quartz, biotite, muscovite, zircon	Undulose extinction, strain shadows, solution seams,
SI-104P	202.8	Quartz, biotite, muscovite	Deformation lamellae, strain shadows, solution seams, undulose extinction, recrystallization, subgrains, crenulation cleavage
SI-105P	212	Quartz, biotite, muscovite, chlorite	Quartz veins, solution seams, strain shadows, recrystallization, bulging, undulose extinction, subgrains, fluid inclusions
SI-106P	243.5	Quartz, biotite, muscovite	Recrystallization, bulging, undulose extinction, solution seams
SI-82	>400	Quartz, biotite, muscovite, opaques	Undulose extinction, crenulation cleavage, (hard to see microstructures with the small grain size)

Table 2: Microstructural analysis and mineral composition for all 24 samples.

9.2 CPO M-index table

Sample	M-index	Sample	M-index
SI-82	0.0047	**SI-93P**	0.0073
SI-83	0.0036	**SI-94P**	0.0014
SI-84	0.0028	**SI-94Q**	0.0112
SI-85	0.0062	**SI-95P**	0.0046
SI-86	0.0026	**SI-96P**	0.0019
SI-87	0.0027	**SI-96Q**	0.0043
SI-88	0.0012	**SI-98P**	0.0008
SI-89	0.0031	**SI-100P**	0.0030
SI-90	0.0044	**SI-101P**	0.0011
SI-91	0.0038	**SI-104P**	0.0015
SI-92Q	0.0080	**SI-105P**	0.0028
SI-92P	0.0064	**SI-106P**	0.0105

Table 3: All 24 samples with the corresponding M-index value

9.3 Scripts used to make all figures

From Michels et al., 2015; https://github.com/zmichels

```
%% grains
% compute grain boundaries
[grains,ebsd.grainId,ebsd.mis2mean] = calcGrains(ebsd,'angle',[10 1]*degree,'boundary','tight');
% remove potentially spurious grains with fewer than 3 solutions
grains = grains(grains.grainSize>=3);
ebsd = ebsd(grains);

% recompute grain boundaries with remaining data
[grains,ebsd.grainId,ebsd.mis2mean] = calcGrains(ebsd,'angle',[10 1]*degree,'boundary','tight');

% remove/smooth stepped boundaries
grains = smooth(grains,10,'moveTriplePoints');

plot(grains)
------------------------------------------------------------
%% remove border grains
% ids of the outer boundary segment
outerBoundary_id = any(grains.boundary.grainId==0,2);

% corresponding grain_id
grain_id = grains.boundary(outerBoundary_id).grainId;

% remove all zeros
grain_id(grain_id==0) = [];

grains(grain_id) = [];
------------------------------------------------------------

%% Compute CVA
[gCVA, bv] = grainsCVA(grains,ebsd);

------------------------------------------------------------

%% Plot CVA
figure,
% condition for consideration (i.e., >=1-degree orientation spread)
cond = gCVA.GOS>=1*degree;
plot(gCVA(cond).CVA,'antipodal','lower','smooth','halfwidth',10*degree)
cb = mtexColorbar('Title','M.U.D.');
% setColorRange([1 max(cb.Limits)]);
annotation('textbox',[0 .7 0 .3],'String',sprintf('n = %i',length(gCVA(cond))),'FitBoxToText','on');
saveFigure(sprintf('%s_quartz_CVA.png',sampleName),'-bestfit')
------------------------------------------------------------
```

```
%% phase of interest
phase = 'q';
---------------------------------------------------------------

%% orientations
gq = gCVA(phase);

odfQ = calcDensity(gq.meanOrientation,'halfwidth',10*degree);
oMode = calcModes(odfQ);
cs =  odfQ.CS;
annotation('textbox',[0 .7 0 .3],'String',sprintf('n = %i',length(odfQ)),'FitBoxToText','on');
h = [Miller(0,0,0,1,'uvtw',cs)]
w = [Miller(1,1,-2,0,'uvtw',cs)];
```

% plot CPO with n=

```
figure,
plotPDF(odfQ,h,'antipodal','lower','smooth','halfwidth',10*degree,'colorrange','equal')
cb = mtexColorbar('Title','M.U.D.');
annotation('textbox',[0 .7 0 .3],'String',sprintf('n = %i',length(gq)),'FitBoxToText','on');
saveFigure(sprintf('%s_quartz_CPO_c_axis.png',sampleName),'-bestfit')

figure,
plotPDF(odfQ,w,'antipodal','lower','smooth','halfwidth',10*degree,'colorrange','equal')
cb = mtexColorbar('Title','M.U.D.');
annotation('textbox',[0 .7 0 .3],'String',sprintf('n = %i',length(gq)),'FitBoxToText','on');
saveFigure(sprintf('%s_quartz_CPO_a_axis.png',sampleName),'-bestfit')
---------------------------------------------------------------
```

%% plot CPO with M-index value

```
figure,
plotPDF(odfQ,h,'antipodal','lower','halfwidth',10*degree,'colorrange','equal');
cb = mtexColorbar('Title','M.U.D.');
MI = calcMIndex(odfQ);
annotation('textbox',[0 .7 0 .3],'String',sprintf('m = %0.4f',MI),'FitBoxToText','on');
saveFigure(sprintf('%s_quartz_CPO_mindex.png',sampleName),'-bestfit')
---------------------------------------------------------------
```

%% plot ODF

```
oriL = ebsd('q').orientations;
figure;
plotPDF(oriL,[Miller(0,0,0,1,ebsd.CS)],'points','all','markerColor','blue','markerSize',2)
figure;
```

```
psi = calcKernel(oriL);
odf = calcDensity(oriL,'kernel',psi);

h = [Miller(0,0,0,1,ebsd('Quartz').CS), Miller(1,1,-2,0,ebsd('Quartz').CS)];
plotPDF(oriL,h,'antipodal','lower','smooth','halfwidth',10*degree)
annotation('textbox',[0 .7 0 .3],'String',sprintf('n = %i',length(oriL)),'FitBoxToText','on');
mtexColorbar

saveFigure(sprintf('%s_quartz_allpoints.png',sampleName),'-bestfit')

close all
```

```
%% grains
% compute grain boundaries
[grains,ebsd.grainId,ebsd.mis2mean] = calcGrains(ebsd,'angle',[10 1]*degree,'boundary','tight');
% remove potentially spurious grains with fewer than 3 solutions
grains = grains(grains.grainSize>=3);
ebsd = ebsd(grains);
------------------------------------------------------------------

% recompute grain boundaries with remaining data
[grains,ebsd.grainId,ebsd.mis2mean] = calcGrains(ebsd,'angle',[10 1]*degree,'boundary','tight');

% remove/smooth stepped boundaries
grains = smooth(grains,10,'moveTriplePoints');


%% remove border grains
% ids of the outer boundary segment
outerBoundary_id = any(grains.boundary.grainId==0,2);

% corresponding grain_id
grain_id = grains.boundary(outerBoundary_id).grainId;

% remove all zeros
grain_id(grain_id==0) = [];

grains(grain_id) = [];
------------------------------------------------------------------

%% Compute CVA
[gCVA, bv] = grainsCVA(grains,ebsd);
------------------------------------------------------------------
```

%% Plot CVA

```
figure,
% condition for consideration (i.e., >=1-degree orientation spread)
cond = gCVA.GOS>=1*degree;
plot(gCVA(cond).CVA,'antipodal','lower','smooth','halfwidth',10*degree)
cb = mtexColorbar('Title','M.U.D.');
% setColorRange([1 max(cb.Limits)]);
annotation('textbox',[0 .7 0 .3],'String',sprintf('n = %i',length(gCVA(cond))),'FitBoxToText','on');
```

%% phase of interest

```
phase = 'q';
```

%% orientations

```
gq = gCVA(phase);

odfQ = calcDensity(gq.meanOrientation,'halfwidth',10*degree);
oMode = calcModes(odfQ);
cs =  odfQ.CS;
annotation('textbox',[0 .7 0 .3],'String',sprintf('n = %i',length(odfQ)),'FitBoxToText','on');
h = [Miller(0,0,0,1,'uvtw',cs),Miller(1,1,-2,0,'uvtw',cs),Miller(1,-1,0,0,'uvtw',cs),Miller(-
1,1,0,1,'uvtw',cs)];
```

%% Discrete low-angle (2–10°) boundary misorientation analysis

```
% Note, the particular approach used here requires that you specify a
% second angle for inner-boundaries during grain reconstructuion (as above)

% get all the subgrain/inner boundaries from the grainset
subB = gq.innerBoundary;

% boundaries of the phase of interest (forsterite in our example case)
subQ = subB(phase,phase);

% condition for only misorientations with angles of 2–10°
condLAB = subQ.misorientation.angle>=2*degree & subQ.misorientation.angle<10*degree;

% the "low-angle" boundaries of interest
labQ = subQ(condLAB);
```

% plot crystal reference frame

```
figure,
plotAxisDistribution(labQ.misorientation,'antipodal','lower','smooth','halfwidth',15*degree,'figSi
ze','small')
cb = mtexColorbar('Title','M.U.D.');
setColorRange([1 max(cb.Limits)]);
saveFigure(sprintf('%s_all_%s_LAB_2to10_axes_XTAL.png',sampleName,phase),'-bestfit')


% plot specimen/spatial reference frame
% first get all the crystal orientations along the boundaries
oLab = ebsd('id',labQ.ebsdId).orientations;

% compute the axis of rotation in specimen reference frame
misAx = axis(oLab(:,1),oLab(:,2));

% and angle
misAng = angle(oLab(:,1),oLab(:,2));

% plot specimen
figure,
plot(misAx,'antipodal','lower','smooth','halfwidth',15*degree)
cb = mtexColorbar('Title','M.U.D.');
setColorRange([1 max(cb.Limits)]);
saveFigure(sprintf('%s_all_%s_LAB_2to10_axes_SPEC.png',sampleName,phase),'-bestfit')

----------------------------------------------------------------

%% G R A I N  S P O  (2D)

% fit ellipses to grain hulls
[omega,a,b] = fitEllipse(grains);
grains.prop.omega = omega;
grains.prop.a = a;
grains.prop.b = b;

% SPO grains filtered by aspect ratio > 1.4
gSPO = grains(grains.a./grains.b>1.4);


% plot polar histograms (rose diagrams) of grain long axes
nbins = 360/5;

% quartz
figure,
```

```
polarhistogram([gSPO(phase).omega;
gSPO(phase).omega+pi],nbins,'Normalization','pdf','FaceColor',gSPO(phase).color,'FaceAlpha',.
75,'EdgeColor','none');
hold on
prose = polarhistogram([gSPO(phase).omega;
gSPO(phase).omega+pi],nbins,'Normalization','pdf');
hold on
prose.DisplayStyle = 'stairs';
prose.EdgeColor = 'k';
drawnow
saveas(gcf,sprintf('%s_SPO_qtz.png',sampleName))


%% save data
close all
save(sprintf('%s.mat',sampleName),'-v7.3');
```

%% rotations for CVA

%% compute directions to use for rotation

```
% bulk vorticity axis
dir1_s = bv(1);
% cross product of vorticity axis with X-direction (assuming x-to-east)
dir2_s = cross(dir1_s,vector3d(1,0,0));
%% define resulting positions for vectors/directions after rotation
dir1_cva = vector3d.Z;
dir2_cva = vector3d.Y;
%% compute a rotation
rot = rotation('map',dir1_s,dir1_cva,dir2_s,dir2_cva);
%% apply the rotation in a plot
figure,
% the key is "multiplying" the orientation by the rotation (not truly
% multiplication... just MTEX notation for concatenating rotations)
plotPDF(rot*odfQ,h,'antipodal','lower','smooth','halfwidth',10*degree,'figsize','medium','colorran
ge','equal')
cb = mtexColorbar('Title','M.U.D.');
% setColorRange([1 max(cb.Limits)]);
saveFigure(sprintf('%s_quartz_cpo_rotated_caxis.png',sampleName),'-bestfit')

figure,
% the key is "multiplying" the orientation by the rotation (not truly
% multiplication... just MTEX notation for concatenating rotations)
```

```
plotPDF(rot*odfQ,w,'antipodal','lower','smooth','halfwidth',10*degree,'figsize','medium','colorran
ge','equal')
cb = mtexColorbar('Title','M.U.D.');
% setColorRange([1 max(cb.Limits)]);
saveFigure(sprintf('%s_quartz_cpo_rotated_aaxis.png',sampleName),'-bestfit')
---------------------------------------------------------------

%% Plot CVA
figure,
% condition for consideration (i.e., >=1-degree orientation spread)

cond = gCVA.GOS>=1*degree;
plot(rot*gCVA(cond).CVA,'antipodal','lower','smooth','halfwidth',10*degree)
cb = mtexColorbar('Title','M.U.D.');
% setColorRange([1 max(cb.Limits)]);
annotation('textbox',[0 .7 0 .3],'String',sprintf('n = %i',length(gCVA(cond))),'FitBoxToText','on');

saveFigure(sprintf('%s_quartz_CVA_rotated.png',sampleName),'-bestfit')
```

9.4 Foliations lineations and vorticity axis plots and table for all samples containing a foliation and lineation

Sample	Foliation (strike/dip)	Lineation (plunge/ trend)	Rake
SI-83	313/81 NE	N/A	
SI-84	306/75 NE	N/A	
SI-85	319/66 NE	N/A	
SI-86	317/69 NE	N/AA	
SI-87	312/43 NE	60/100	
SI-88	313/66 NE	N/A	
SI-89	305/70 NE	N/A	
SI-90	303/69 NE	N/A	
SI-91	305/50 NE	N/A	
SI-92P	327/70 NE	37/131	40 E
SI-92Q	340/65 NE	58/111	70 E
SI-93	320/40 NE	79/345	
SI-94P	300/65 NE	65/030	
SI-94Q	300/65 NE	65/030	
SI-95P	287/16 NE	24/109	40 E
SI-96P	321/34 NE	18/111	90
SI-96Q	321/34 NE	18/111	90
SI-98	318/76 NE	42/125	
SI-100	281/73NE	N/A	
SI-101	302/52 NE	08/116	
SI-104	298/50 NE	N/A	
SI-105	313/67 NE	N/A	
SI-106	322/40 NE	N/A	
SI-82	080/79 N	63/058	

Table 4: Data are from Carman, 2010 and unpublished data from field colleagues (Czeck, Díaz-Azpiroz, or Fernández). Where possible, data are from the exact location of the sample. However, some fabric data are used from sites within 3 m if immediate data is unavailable. These data are used in the following stereonet plots.

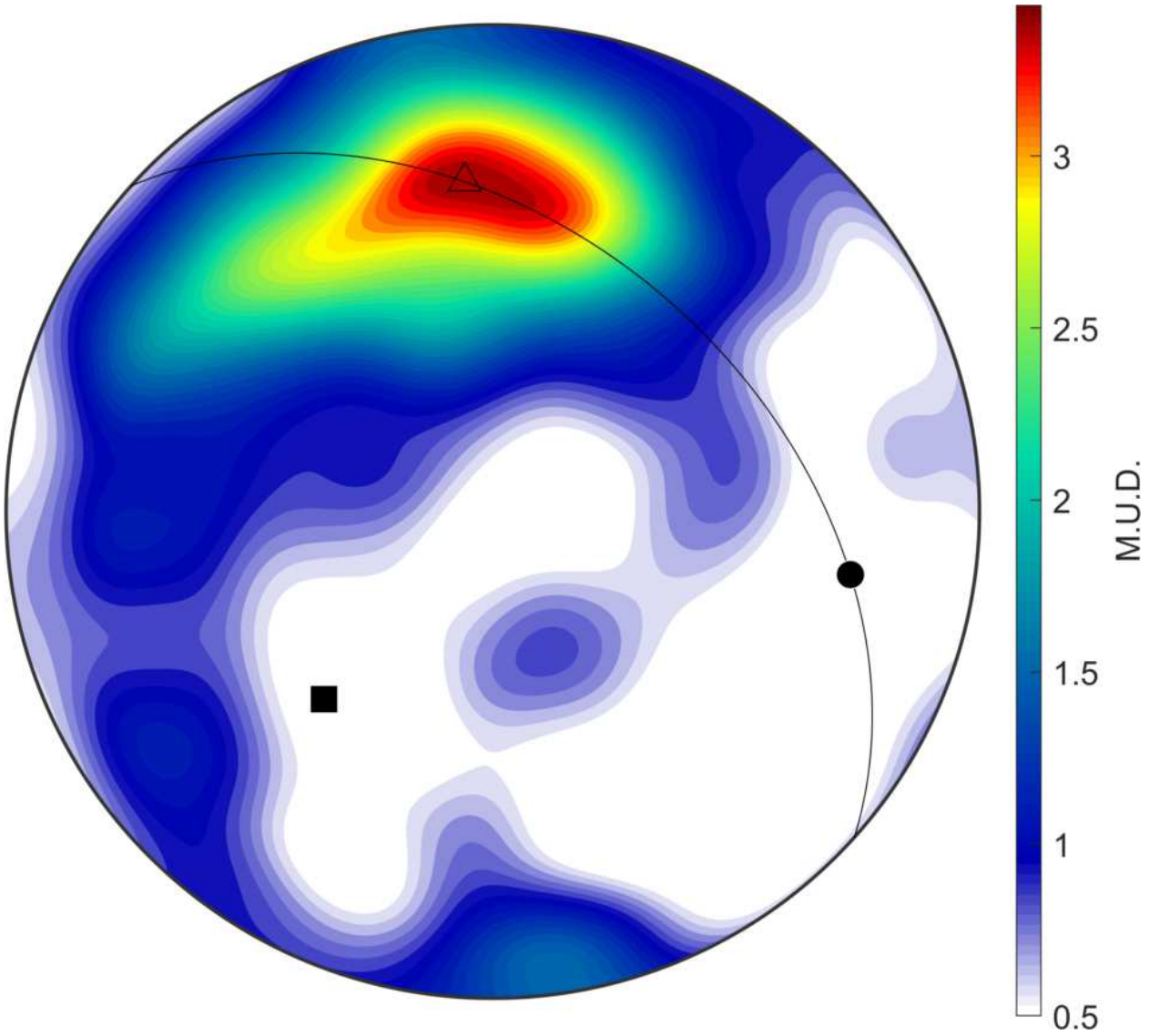

Figure 36: Quartz c-axis CPO for sample SI087 rotated into a geographic reference frame. Contours are multiple of uniform density (M.U.D.), a statistical description of fabric intensity. Field fabrics of foliation (black great circle), pole to foliation (black square), and lineation (black circle) indicated. Vorticity axis inferred from CVA orientation indicated by unfilled triangle.

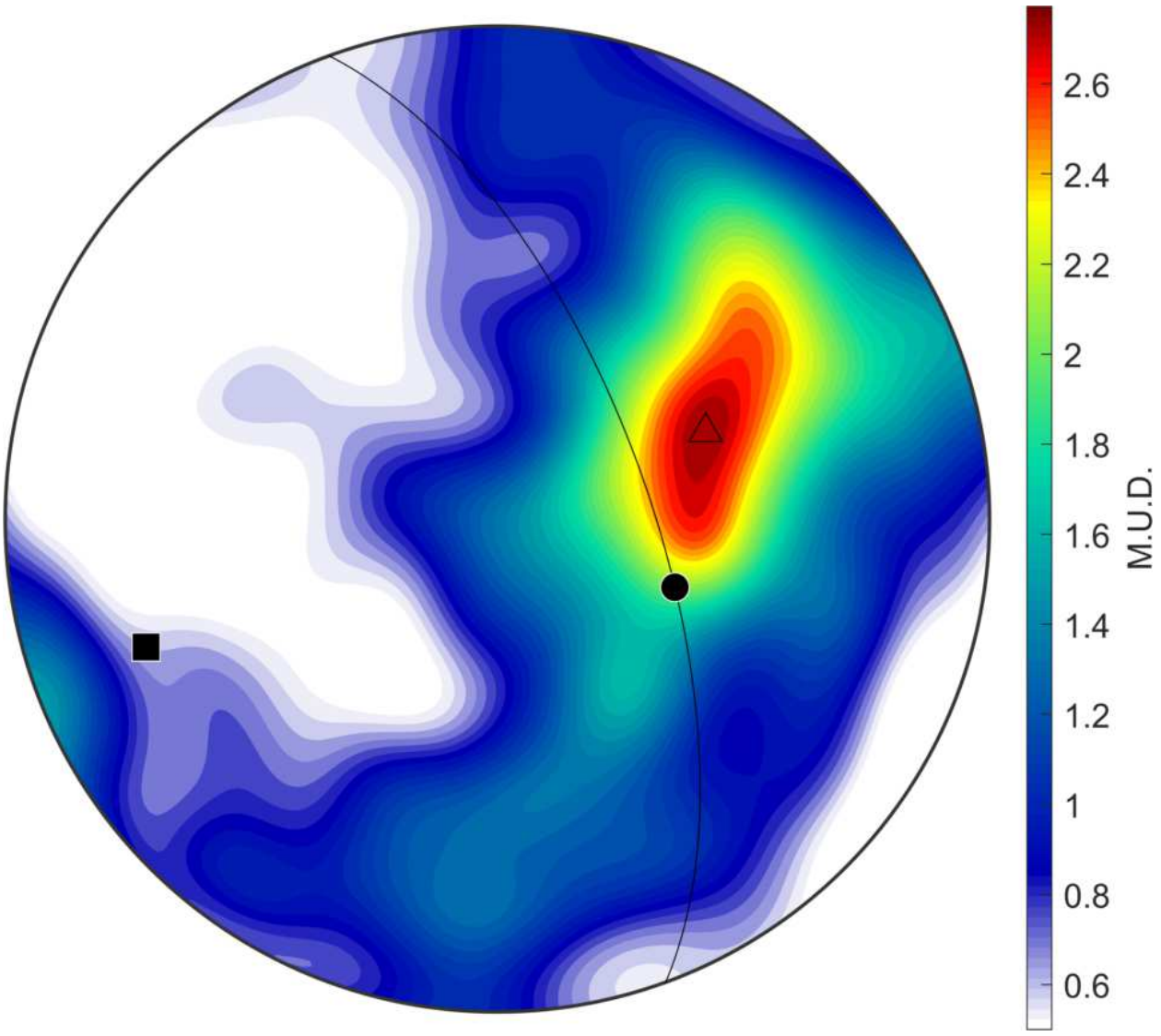

Figure 37: Sample SI-92Q rotated into the geologic reference frame. Contours are multiple of uniform density (M.U.D.), a statistical description of fabric intensity. Field fabrics of foliation (black great circle), pole to foliation (black square), and lineation (black circle) indicated. Vorticity axis inferred from CVA orientation indicated by unfilled triangle.

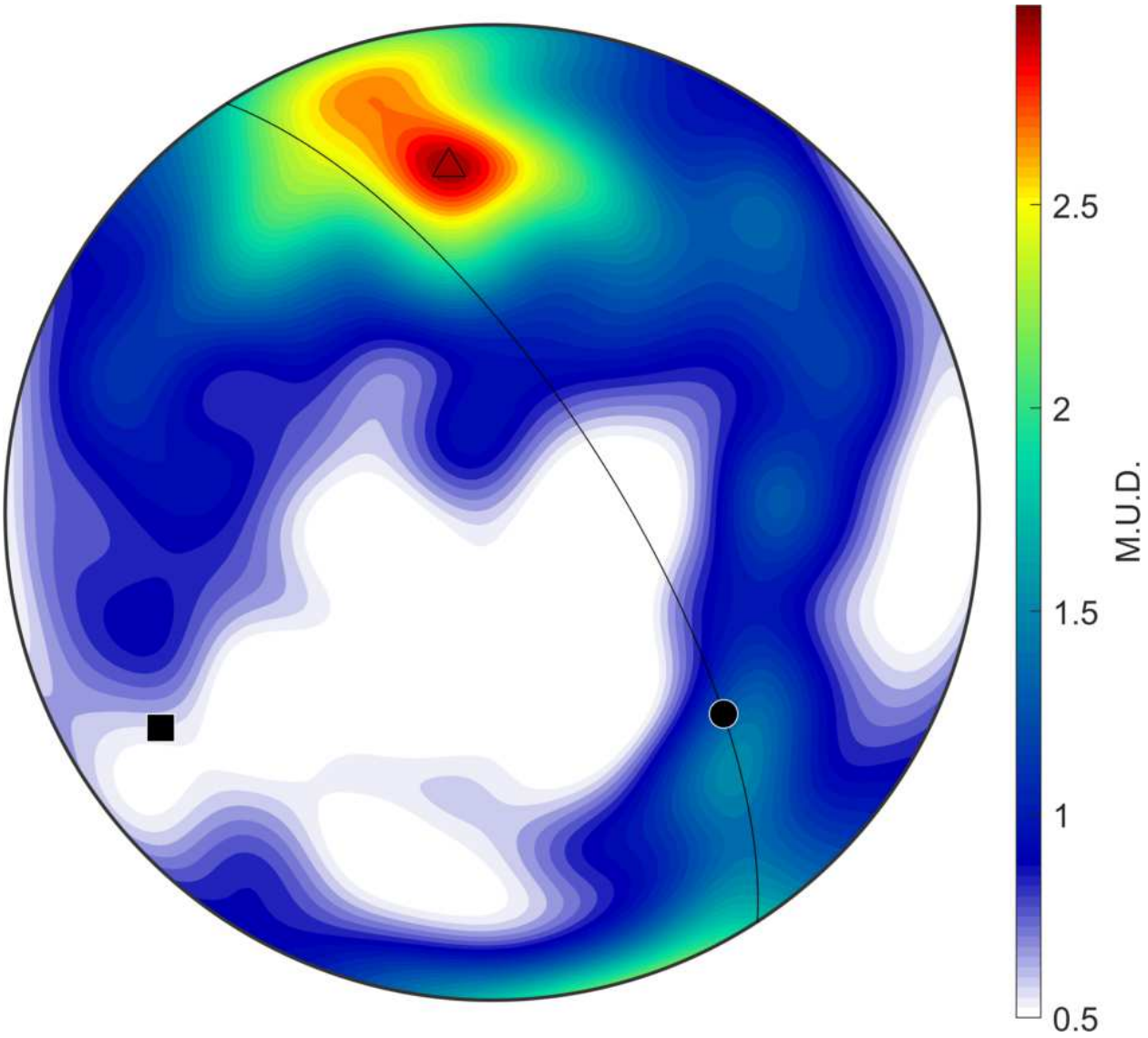

Figure 38: Sample SI-92P rotated into the geologic reference frame. Contours are multiple of uniform density (M.U.D.), a statistical description of fabric intensity. Field fabrics of foliation (black great circle), pole to foliation (black square), and lineation (black circle) indicated. Vorticity axis inferred from CVA orientation indicated by unfilled triangle.

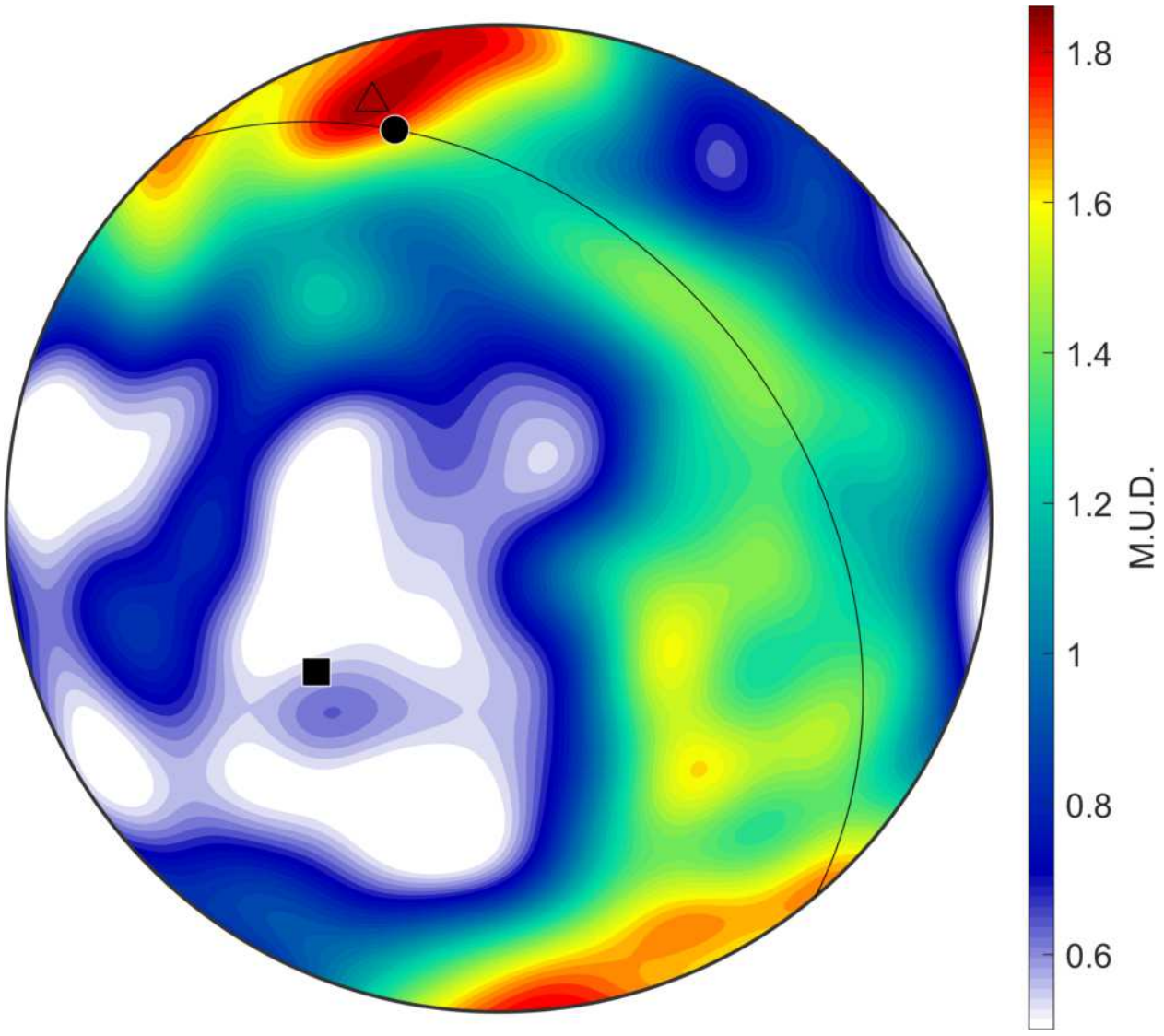

Figure 39: Sample SI-93 rotated into the geologic reference frame. Contours are multiple of uniform density (M.U.D.), a statistical description of fabric intensity. Field fabrics of foliation (black great circle), pole to foliation (black square), and lineation (black circle) indicated. Vorticity axis inferred from CVA orientation indicated by unfilled triangle.

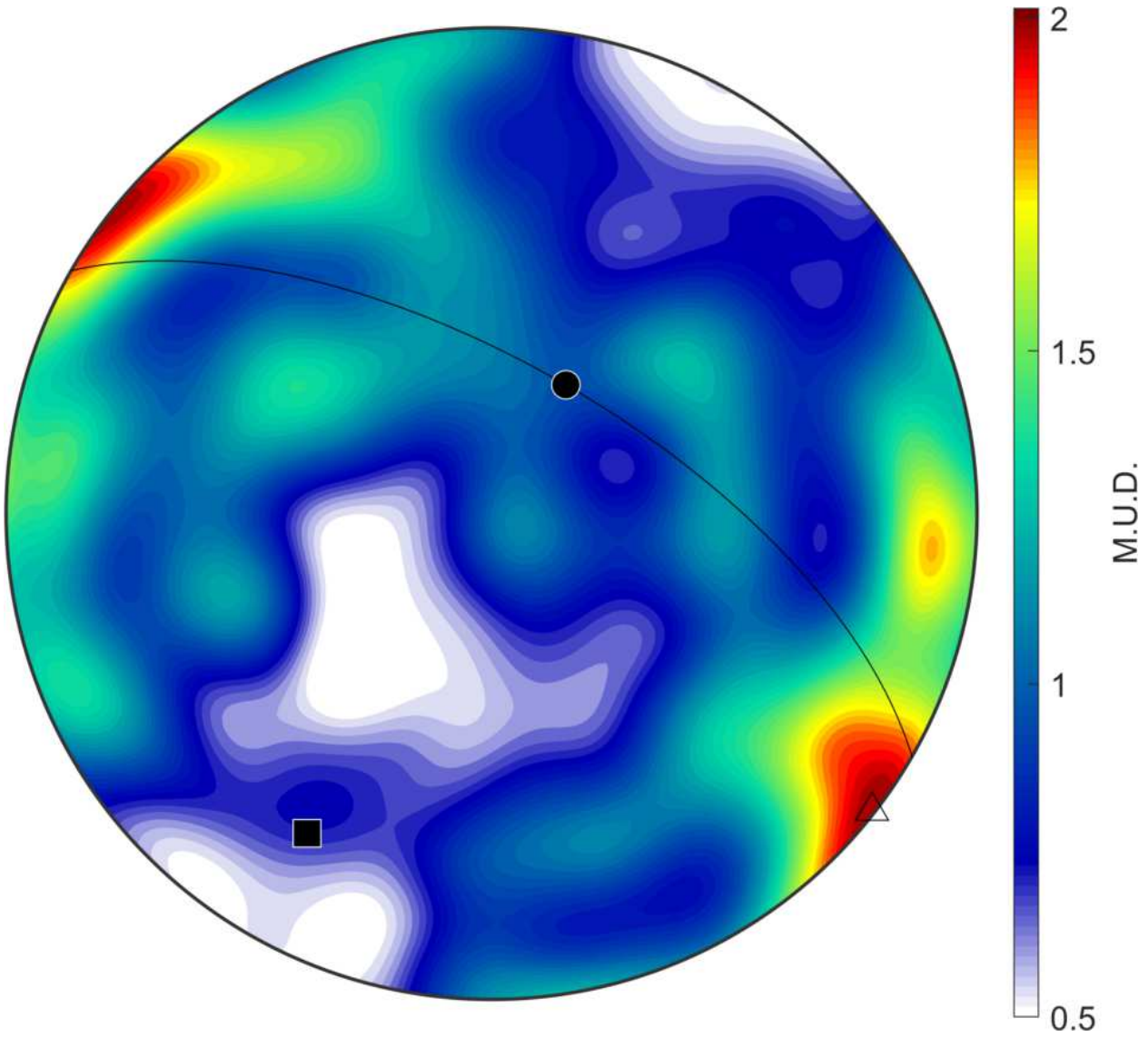

Figure 40: Sample SI-94P rotated into the geologic reference frame. Contours are multiple of uniform density (M.U.D.), a statistical description of fabric intensity. Field fabrics of foliation (black great circle), pole to foliation (black square), and lineation (black circle) indicated. Vorticity axis inferred from CVA orientation indicated by unfilled triangle.

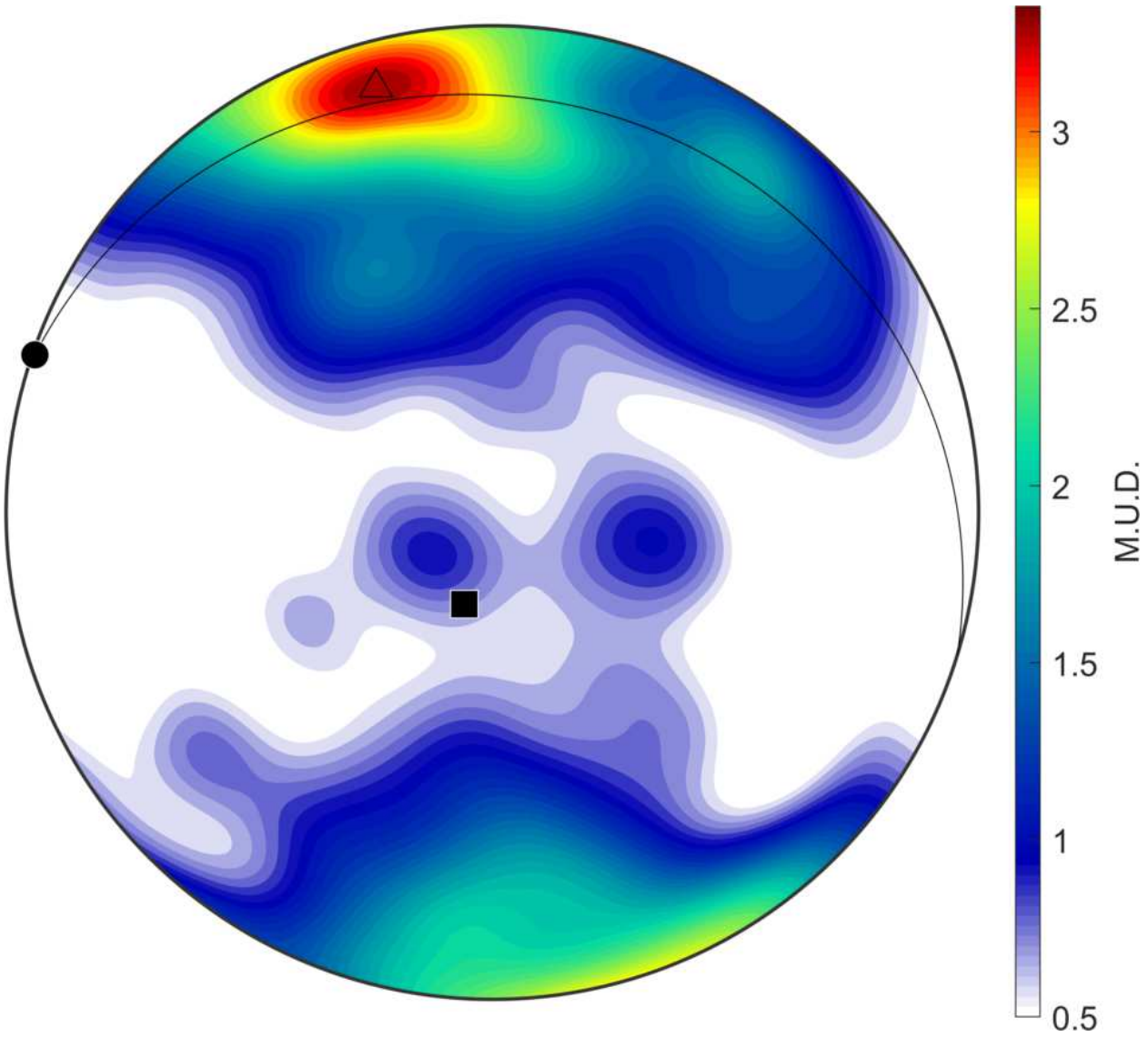

Figure 41: Sample SI-95P rotated into the geologic reference frame. Contours are multiple of uniform density (M.U.D.), a statistical description of fabric intensity. Field fabrics of foliation (black great circle), pole to foliation (black square), and lineation (black circle) indicated. Vorticity axis inferred from CVA orientation indicated by unfilled triangle.

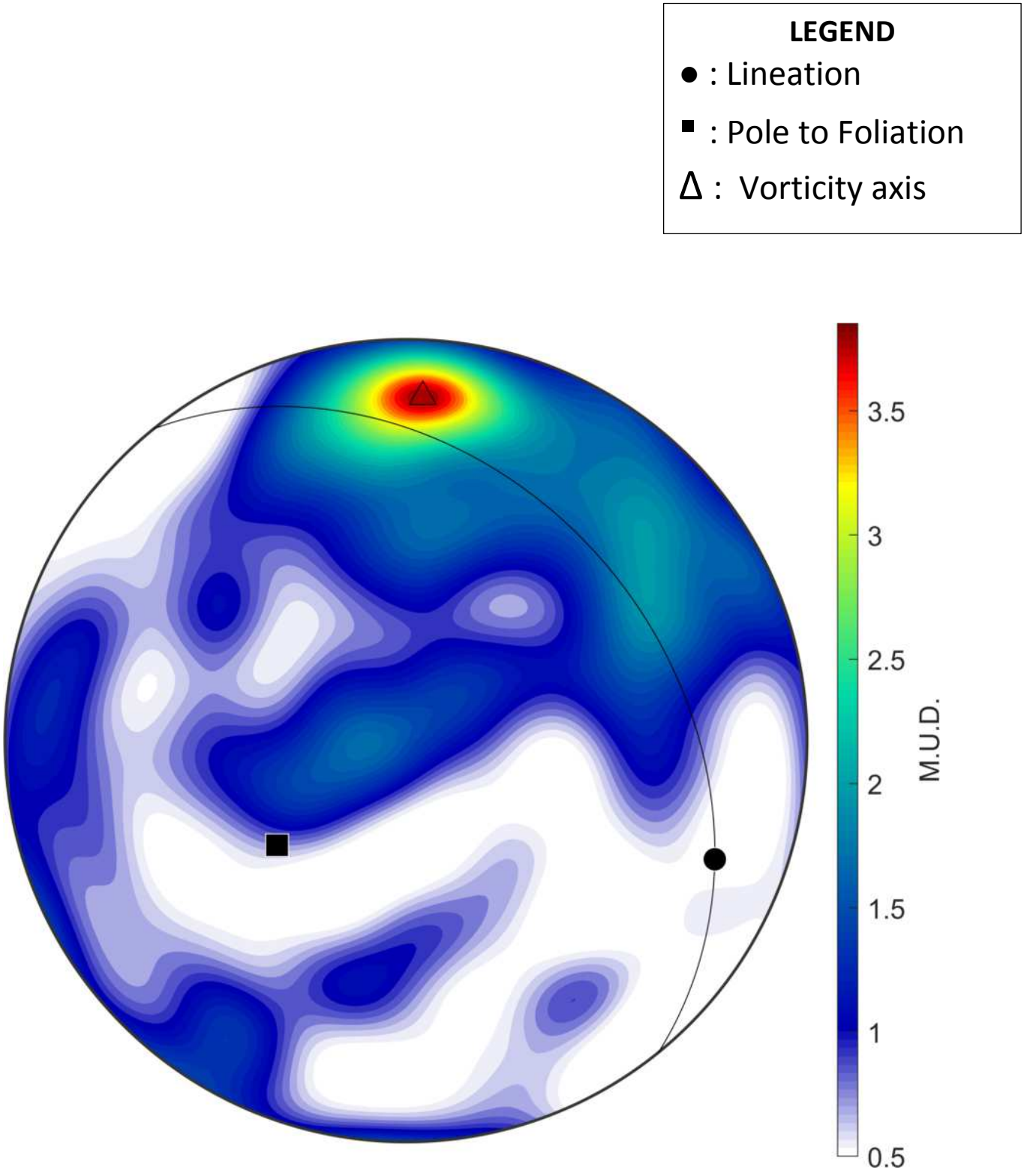

Figure 42: Sample SI-96P rotated into the geologic reference frame. Contours are multiple of uniform density (M.U.D.), a statistical description of fabric intensity. Field fabrics of foliation (black great circle), pole to foliation (black square), and lineation (black circle) indicated. Vorticity axis inferred from CVA orientation indicated by unfilled triangle.

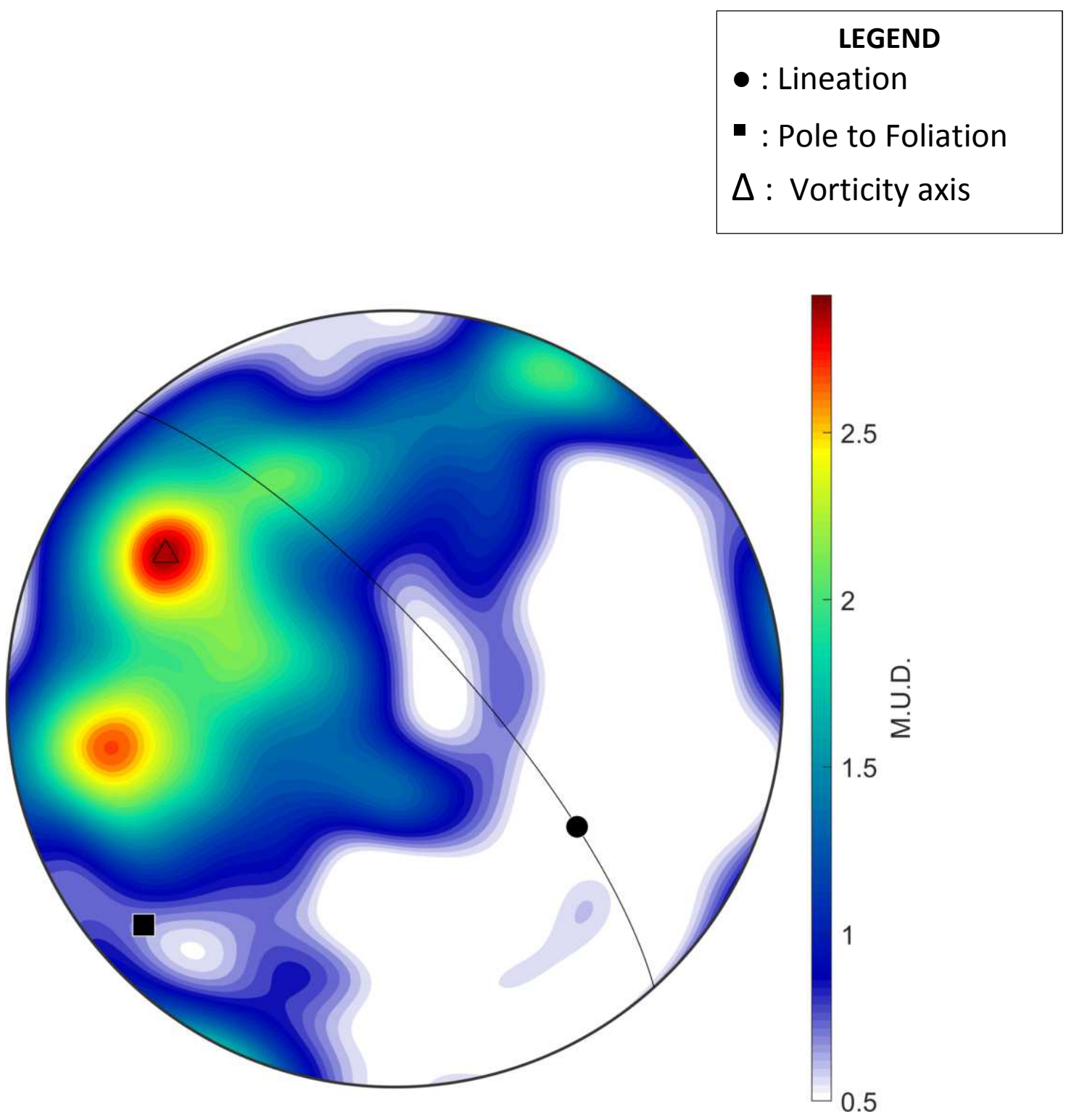

Figure 43: Sample SI-98P rotated into the geologic reference frame. Contours are multiple of uniform density (M.U.D.), a statistical description of fabric intensity. Field fabrics of foliation (black great circle), pole to foliation (black square), and lineation (black circle) indicated. Vorticity axis inferred from CVA orientation indicated by unfilled triangle.

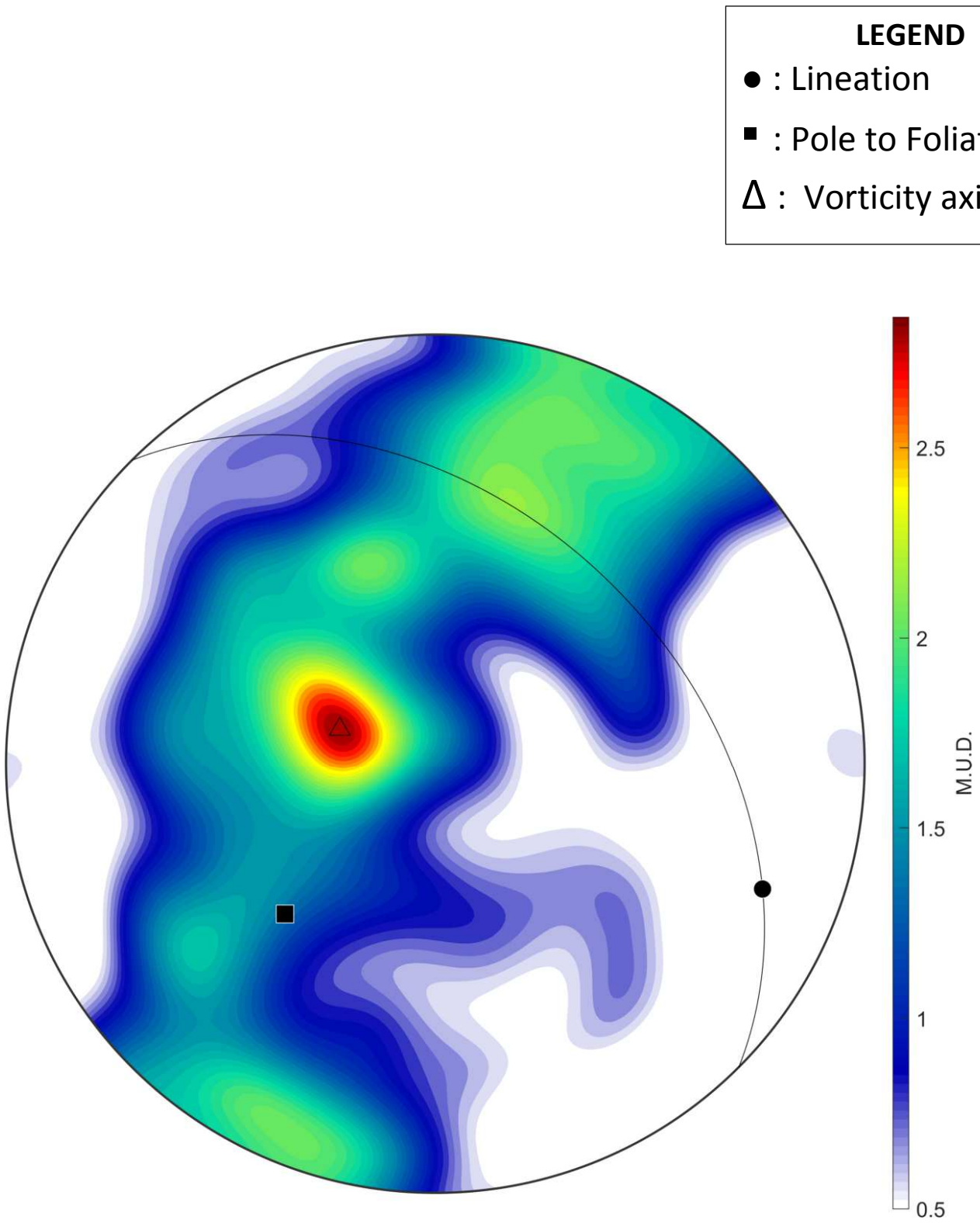

Figure 44: Sample SI-100P rotated into the geologic reference frame. Contours are multiple of uniform density (M.U.D.), a statistical description of fabric intensity. Field fabrics of foliation (black great circle), pole to foliation (black square), and lineation (black circle) indicated. Vorticity axis inferred from CVA orientation indicated by unfilled triangle.

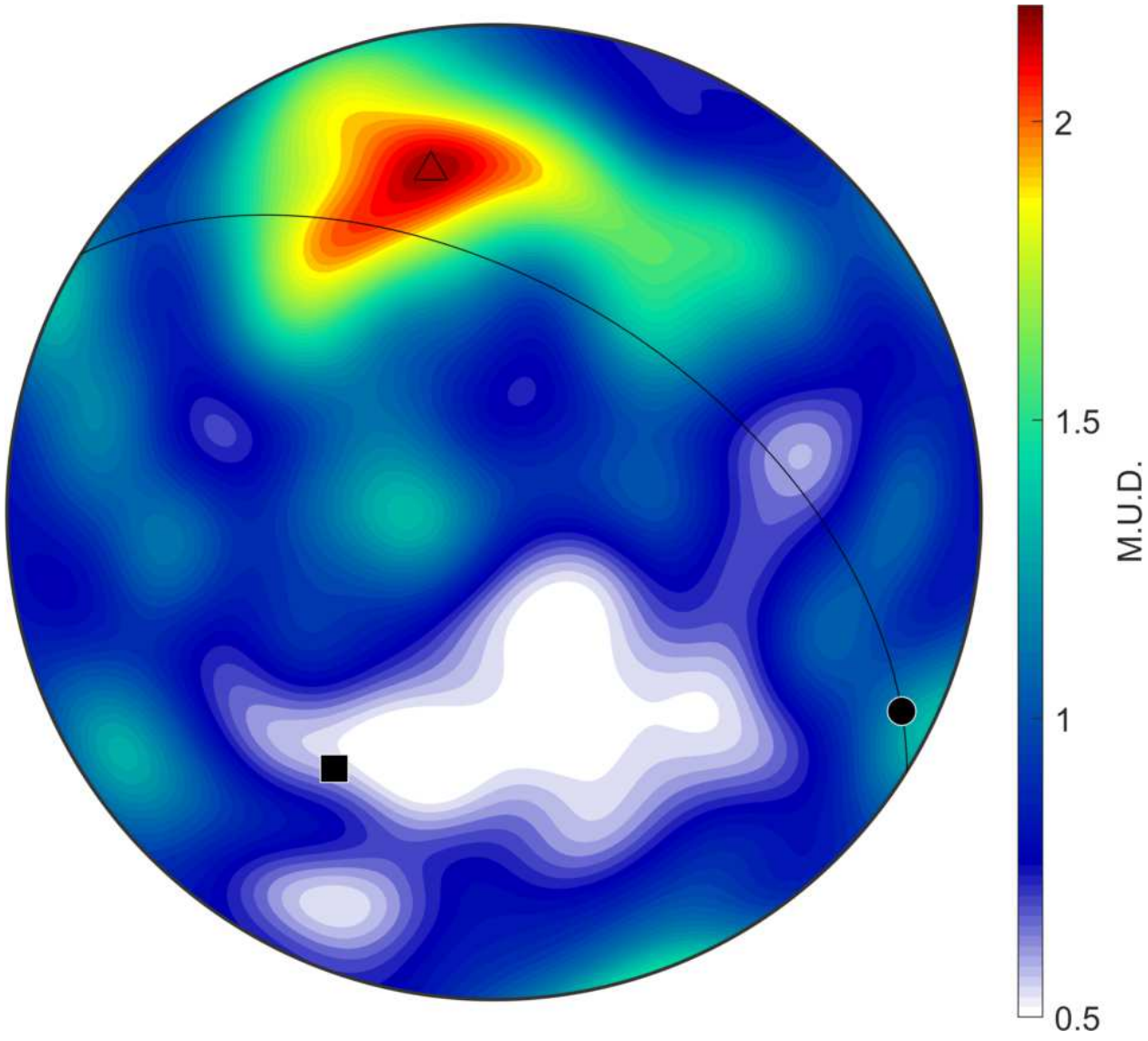

Figure 45: Sample SI-101P rotated into the geologic reference frame. Contours are multiple of uniform density (M.U.D.), a statistical description of fabric intensity. Field fabrics of foliation (black great circle), pole to foliation (black square), and lineation (black circle) indicated. Vorticity axis inferred from CVA orientation indicated by unfilled triangle.

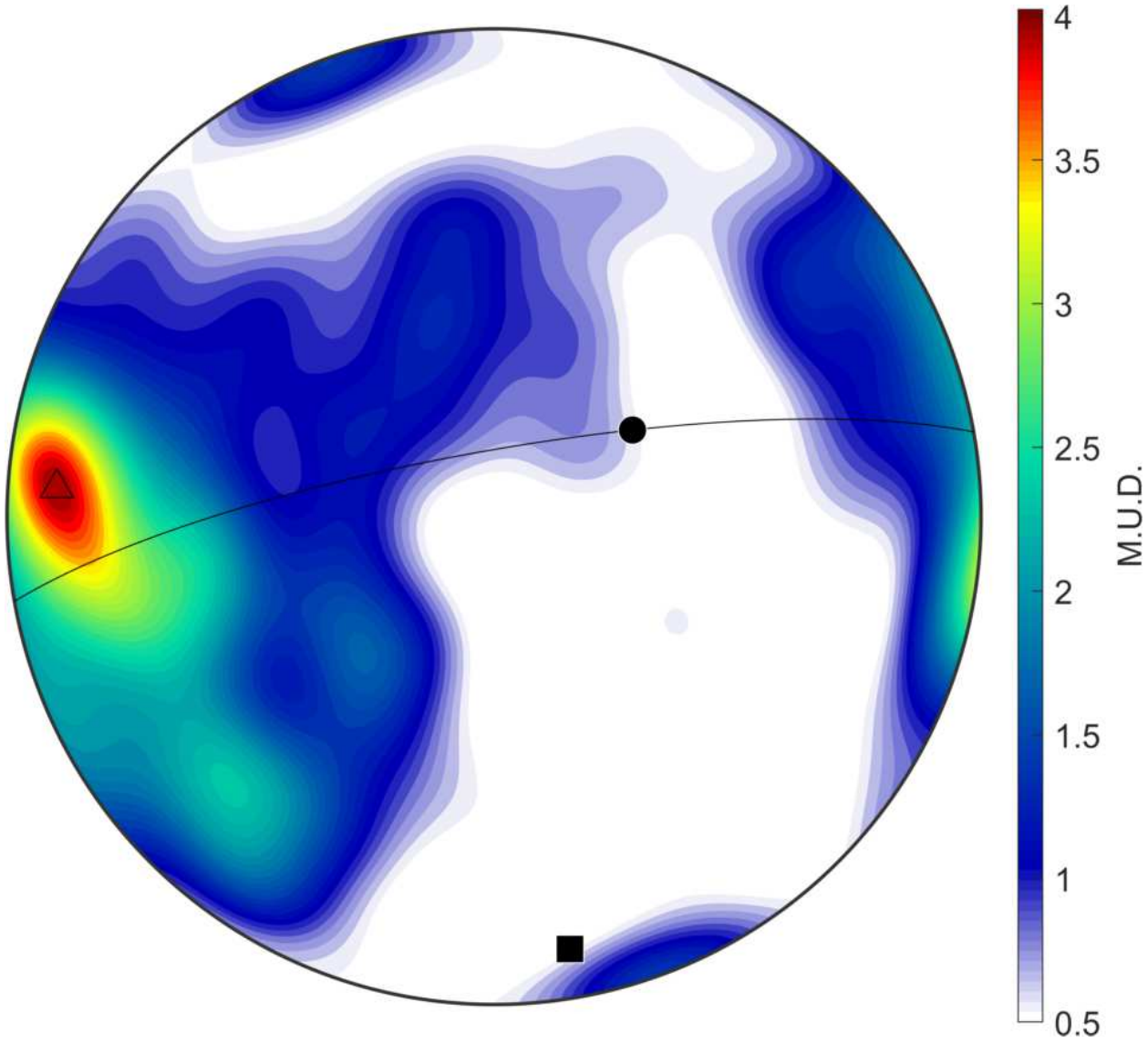

Figure 46: Sample SI-82 rotated into the geologic reference frame. Contours are multiple of uniform density (M.U.D.), a statistical description of fabric intensity. Field fabrics of foliation (black great circle), pole to foliation (black square), and lineation (black circle) indicated. Vorticity axis inferred from CVA orientation indicated by unfilled triangle.